THE BELL SYSTEM

TECHNICAL JOURNAL

VOLUME XLVI SEPTEMBER 1967 NUMBER 7

Statistical Analysis and Modeling of the High-Energy Proton Data From the *Telstar*® 1 Satellite

By J. D. GABBE, M. B. WILK and W. L. BROWN

(Manuscript received October 4, 1966)

This paper deals with the analysis of data from the omnidirectional high-energy proton detector on the Telstar® 1 satellite. The main accomplishment is the development of relatively simple (empirical) mathematical models which give a statistically accurate representation of the measured spatial distribution of intensity of protons with energies between 50 and 130 MeV.

These models depend upon the fitting of 8 (or 9 or 10) coefficients based on samples containing approximately 1000 of the nearly 80,000 experimental observations. The nature of the model for the average omnidirectional counting rate permits its closed form transformation to the equivalent equatorial pitch angle distribution.

Sufficiently accurate fits were achieved so that the residuals (equal to observed minus fitted) could be productively examined for possible dependence on variables other than the two magnetic coordinates used in the fitting. One consequence of this was the detection of instrumental susceptibility to temperature and bias voltage changes, which led to an objective partitioning of the data.

The present paper has several evolutionary aspects: In particular, a series of one-dimensional fits was employed as a base for developing a two-dimensional model; a preliminary analysis of all the data was used to guide the rejection of outliers; a first two-dimensional fit to all the data *led to a data-independent basis for partitioning the data; the mode of selection of a sample of data, to which the two-dimensional model was fitted, changed as deeper insight into the importance of this issue developed; and, after a very satisfactory fit to the data was attained, the model was improved by specialization and reparameterization so as to overcome some statistical defects and to achieve greater physical meaning.*

The data cover the time period between July 1962 and February 1963, and the spatial region bounded by $1.09\, R_e \leqq R \leqq 1.95\, R_e$ *and* $0 \leqq \lambda < 58°$. *Flux maps having a relative accuracy of about two percent are derived from the fit and presented. The temporal behavior of the intensity is examined and some changes are noted. The maximum value of the omnidirectional flux of protons with energies between 50 and 130 MeV is found to be* $[5.7^{+1.4}_{-2.8}] \times 10^3$ *protons/cm*^{2} *sec at* $L = 1.46$ *on the magnetic equator, in good agreement with other experiments. Relative flux values and energy spectra are consistent with the generally accepted picture of the proton distribution.*

TABLE OF CONTENTS

I. INTRODUCTION

This paper deals with the analysis of data from the omnidirectional high-energy proton detector on the *Telstar*® 1 satellite. The main accomplishment is the development of a relatively simple (empirical) mathematical model which gives a statistically accurate representation of the measured spatial distribution of protons with energies between 50 and 130 MeV.

The *Telstar*® 1 satellite was launched into a 45°-inclined orbit with an apogee of 5600 km and a perigee of 950 km on day 191 (July 10), 1962. The period of precession of the apsis was 180 days. The satellite was instrumented to measure fluxes of energetic particles; in particular, counting rates of protons with energies above 50 MeV were recorded. Two thousand hours of telemetry was received during the active life of the satellite, which terminated on day 52 (February 21), 1963. The satellite and associated systems have been described in detail.[1] The particle-detection instruments have been documented[2] and some of the experimental results have been presented.[3, 4, 5]

The above-mentioned presentations of information concerning the earth's radiation belts have been principally graphical in format, owing to the complexity of the belts and the limited understanding of the details of the processes affecting them.

An accurate analytical representation of the data would enable convenient interpolation, extrapolation, and transformation. Thence it would be practical to make extensive comparisons with the results of other experiments and with various theoretical predictions and to summarize, analytically, such features as the equatorial omnidirectional counting rate and the approximate size of the equatorial loss cone. In addition, an empirical mathematical model would facilitate the study of temporal fluctuations in various regions of space. Of course, a good analytical representation, even though empirical, may also stimulate deeper physical insight and theories.

The present study was directed toward the development of a mathematical function which would, when fitted to the data, provide a convenient, concise and precise summary description. The mathematical model(s), which are herein presented, were empirically evolved, using the knowledge that the intensity distribution of these protons is, in the main, not rapidly variable in time. Even more specifically, the assumption has been that fluctuations in observed counting rates at a fixed point in space relative to the earth are independent random variables. Further, the main effort of the analysis has been to try to relate the observed counting rates to a two-dimensional magnetic coordinate system derived from three-dimensional spatial coordinates by mapping the known earth's magnetic field onto the field of a magnetic dipole.[6]

The mathematical models which are used depend upon fitting of between 8 and 10 coefficients based on samples containing approximately

1000 of the nearly 80,000 experimental observations. The nature of these models for the average omnidirectional counting rate permit their closed-form transformation to the equivalent equatorial pitch angle distribution.

The fitted models were sufficiently accurate so that the residuals (equal to observed minus fitted) of all the data could be productively examined for possible dependence on variables other than the two magnetic coordinates used in the fitting. One consequence of this was the detection of instrumental susceptibility to temperature and bias voltage change, which led to an objective partitioning of the data.

This article summarizes some of the productive aspects of the analysis of this body of data. A very large amount of "preliminary" work is not reviewed. Though not an historical description of the work, the present paper does have several evolutionary aspects. In particular, a series of one-dimensional fits were employed as a base for developing two-dimensional models; a preliminary analysis of all the data was used to guide the rejection of outliers; a first two-dimensional fit to all the data led to a data-independent basis for partitioning the data; the mode of selection of a sample of data, to which the two-dimensional model was fitted, changed as deeper insight into the importance of this issue developed; and, after a very satisfactory fit to the data was attained, the model was improved by specialization and reparameterization so as to overcome some statistical defects and to achieve greater physical meaning.

Readers with specific interests may wish to consult the Table of Contents, the summary (Section XIV) and the following overview for guidance.

Section II introduces the input data which have been analyzed. Coordinates and notation are tabulated, the distribution of the data is displayed, and the general quality and stability of the data are discussed. It is shown informally that the measurements may be usefully organized in the dipole magnetic coordinate system used.

In Section III, various alternative coordinate systems and scales are considered. The bases for choice of the x,L coordinate system for the independent variables and the square-root-of-counting-rate scale for the dependent variable are given.

Section IV brings together the ideas underlying the formulation and evolution of the models, and gives mathematical definitions and details. Some properties of the models which make them suitable smoothing functions for this body of data are indicated.

One-dimensional fits to the data in each of several L-slices (an

L-slice is a particular grouping of the data) are displayed on several scales and discussed in Section V. It is shown that L-slice fits suffer from fundamental deficiencies, in addition to being inconvenient to work with. The results of the L-slice fits are used to lead to a two-dimensional model.

Section VI contains the treatment of the preliminary fit of a two-dimensional model. This fit is of good quality and provides residuals which are used to help identify and eliminate extraneous sources of variability in the data and to serve as a basis for more refined sample selection.

The treatment of the two-dimensional fit to the data after it has been partitioned to reduce instrumental effects appears in Section VII. The method of sample selection is important, and some algorithms and their influence on the resultant fits are considered in Section 7.1. The advantages of selecting a sample on the basis of a preliminary fit are discussed. The fit itself is described and evaluated in the remainder of the section.

A more detailed statistical critique of the fit discussed in Section VII is contained in Section VIII; in particular, some remaining physical and statistical defects are pinpointed.

Section IX deals with a modified version of the model, which eliminates the remaining defects, and gives the results of fitting the most satisfactorily parameterized model of the proton distribution.

Residuals are used to study temporal effects in Section X. An increase in intensity near $L = 2$ is noted during October, 1962. An upper limit of 0.003 gauss is found for the diurnal variation of the earth's magnetic field near $L = 1.5$. A possible shift in the location of the atmospheric cutoff is examined.

The behavior of the radiation belt near the top of the atmosphere is the subject of Section XI. Although the data do not allow the position of the low-altitude cutoff to be accurately determined, the qualitative behavior precludes a simple atmospheric cutoff mechanism.

Section XII is devoted to a comparison of the *Telstar*® 1 results, presented as flux maps, with those obtained on Injuns 1 and 3, Explorers 4 and 15, and other satellites. Absolute flux values agree to within a factor of 2 in most cases, which is as well as can be expected. Very good agreement exists concerning the behavior of the intensity in the equatorial plane, on L-shells, and near the top of the atmosphere. Experimental results regarding the equatorial pitch angle (see Fig. 1) distribution are found to agree well with each other, but differ appreciably from the published results of theoretical calculations.

Section XIII gives brief consideration to possible directions in which this work might be extended: improving the fit to the *Telstar*® 1 high-energy protons still further; approaching model development differently; employing the data more fully; and encompassing other more complex bodies of data.

Section XIV contains a brief summary of the results and Section XV contains acknowledgments.

Appendix A provides a detailed description of the particle detector and its calibration.

Appendix B gives some statistical background and details of the analysis, and Appendix C discusses statistical measures of the goodness of fit of the model over all the partitioned data.

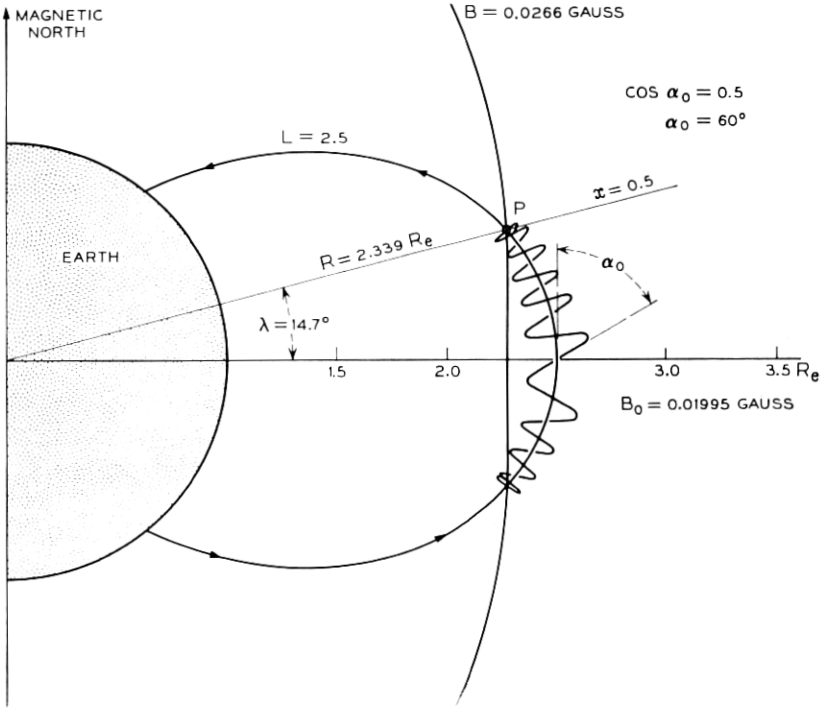

Fig. 1 — Magnetic coordinates of the point P. The spiral is the orbit of a particle trapped on the magnetic line of force $L = 2.5$ and mirroring at $B = 0.0266$ gauss. The equatorial pitch angle, α_0, is the angle between the velocity vector and the magnetic field vector at the equator.

II. THE DATA

The data which are studied in this paper were obtained with a detector on the *Telstar*® 1 satellite which measured protons with energies greater than 50 MeV. The sensitive detecting element is a semiconductor diode developed specifically for satellite experiments.[7] The effective geometric factor, g, of the detector depends upon proton energy, but over the region energy between 50 and 130 MeV the *average* geometric factor, $\bar{g}$, is relatively insensitive to the energy spectrum and an approximate value of 0.143 cm^2 steradian has been selected. These considerations are discussed in detail in Appendix A. The response of the detector is also dependent upon both temperature and electrical bias because of changes in the effective thickness of the active region of the detector. These effects are discussed in Section 6.8.

The primary input to our data reduction process consisted of: the telemetry record of the number of counts measured by the detector in an 11-second counting interval once every minute; the time at which the data were recorded (inserted by the recording station); and the ephemeris of the satellite position obtained from tracking data. These are supplemented by the satellite spin-axis orientation obtained from the mirror flash data[8] and by telemetered measurements of the satellite skin temperature near the detector and of the detector bias voltage.

During data reduction, the square root of the counting rate was computed for each recorded particle-counting interval and associated with the following information: date and time, geographic position, position in the earth's magnetic field, orientation of the detector relative to the magnetic field, bias voltage, and skin temperature.

The model developed in the present paper is based on the use of a two-dimensional magnetic coordinate system, in which the earth's magnetic field is mapped onto an axially symmetric dipole field using the adiabatic invariants of particle motion.[9] Any of a number of equivalent pairs of magnetic coordinates, including the B,L; R,λ and x,L sets[10] may be used to locate position in this dipole field. Briefly: The magnetic shell parameter, L, specifies a particular line of force (about which the trapped particle spirals) by the radial distance to the line in the equatorial plane of the dipole measured in units of one earth radius (see Fig. 1); position along the line of force is specified by either the magnetic induction (field strength), B, or by x, where $x = (1 - B_0/B)^{\frac{1}{2}}$ is a convenient variable in the equations of the dynamics of charged particle motion. (B_0 is the magnetic induction at the equator on the line of force in question.) Magnetic dipole polar coordinates R and λ,

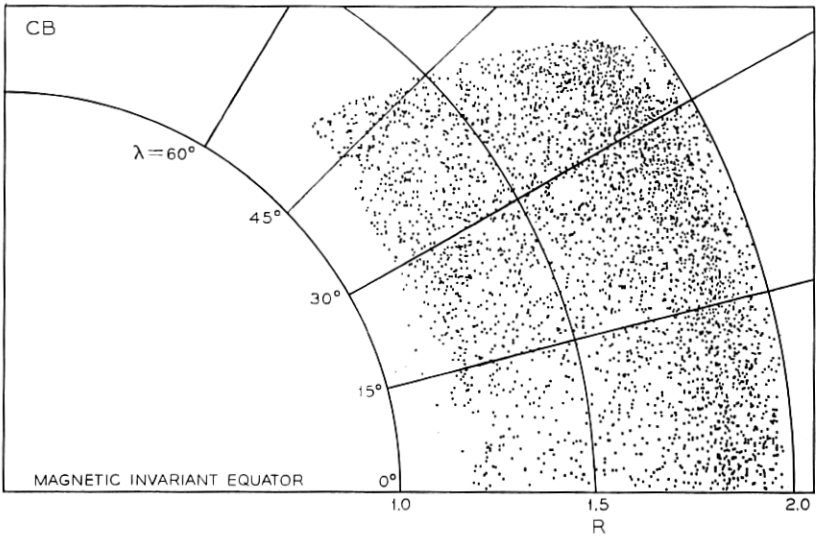

Fig. 2 — The spatial distribution of data for $L < 3$ in R, λ coordinates. Every twentieth point from the L-ordered data is plotted.

where R is the radial distance in earth radii and λ is the latitude angle, offer a sufficiently close analog to geographic coordinates to be convenient in many circumstances. The choice among these sets is discussed in Section III, as are the reasons for choosing the square root of the counting rate as the scale for the dependent variable.

The coordinates and variables, together with other symbols used in this analysis, are listed in Table I under the following headings: Radiation Intensity, Position and Orientation, Instrument and Energy Spectrum, Mathematical Model, Statistics, and Other. Summary information concerning units, constants, derivations, and sources is included.

The satellite was confined to the volume of space $\{1.09\ R_e \leqq R \leqq 1.95\ R_e,$* $0 \leqq \lambda \leqq 58°\}$. For $\{L > 3, R < 1.95\ R_e\}$, the average counting rate is very nearly zero, and these data were not examined further. About 5 percent of the 50–130 MeV proton data for $L \leqq 3$ were associated with noise bursts which affected adjacent telemetry channels; these data were discarded. The study described below is based on the remaining 77,649 observations.

The spatial distribution of the data is indicated in Fig. 2 which is

---

* R_e = earth radius.

a plot in R,λ coordinates of the position of every twentieth point from the L-ordered data. Although data were not acquired continuously during the 226 days that the satellite was active, there are no time gaps in the data longer than two days in duration.

Fig. 3 is a plot of bands of constant counting rate made by plotting the R,λ coordinates at which certain specified numbers of counts were recorded during 11-second counting intervals. The data in Fig. 3 cover the entire seven-month life of the satellite. The narrowness of the contour bands demonstrates that the data are exceptionally well-behaved in both time and space, and that one may reasonably hope to describe radiation intensity in terms of R,λ coordinates or their equivalent.

Among the various sources of error in the data are: noise present in the received telemetry signal or introduced during the recording and processing of the telemetry; errors in the time as recorded by the ground station; errors in the satellite ephemeris; differences between the real magnetic field of the earth and the values of B and L calculated from the coefficients in the computer program INVAR (see Table I); and instrumental effects. In addition, one expects statistical fluctuations in the measured counting rate at a fixed position. The importance of these sources of error is discussed later.

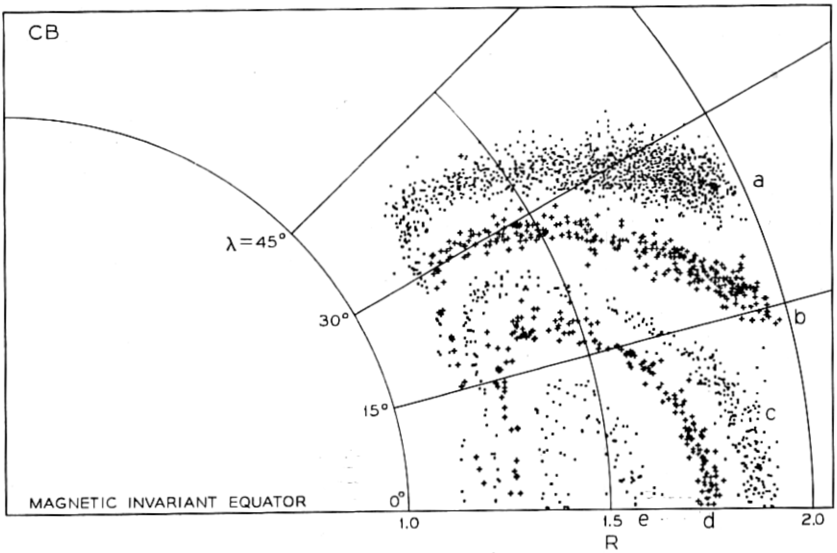

Fig. 3 — Bands of constant numbers of counts in 11 seconds in R, λ space: Band a, 4; Band b, 32; Band c, 127–129; Band d, 254–258; Band 3, 508–516 counts. All the data from the seven-month period are displayed.

III. CHOICE OF THE PRINCIPAL VARIABLES AND THEIR SCALES

The current state of knowledge of the earth's radiation belts suggests that the spatial distribution of high-energy protons may reasonably be organized on the basis of a two-dimensional magnetic coordinate system, except perhaps at very low altitudes near the South American magnetic anomaly, where longitude also becomes important. *Telstar*® 1 data plotted in Fig. 3 indicates that the observed counting-rate data does indeed depend principally on the magnetic coordinates, R and λ. The coordinates R,λ are defined in terms of the mathematically equivalent pair B,L.[9] A third equivalent set consists of L together with the coordinate x, suggested by Roberts,[10] defined in Table I.

We have primarily employed the x,L set in this study because of the following considerations: In the adiabatic theory, the mirror points of particles do not migrate between magnetic shells.[11] Within any shell, the coordinate x is approximately linear in λ for $\lambda < 30°$, and thus the near-equatorial data is not "crowded" into a small interval of the coordinate, as is the case for B. Moreover, we have been able to develop simple functional representations of the data in terms of x and L.

The flux of particles is the variable of greatest physical interest for comparing the results of different experiments, calculating physical effects of the radiation (such as radiation damage to devices in proposed orbits), deriving an energy spectrum from experimental measurements, examining the implications of various source and loss mechanisms, etc. However, the flux is not measured directly and requires for its calculation knowledge of the energy spectrum of the particles and of the energy dependence of the geometric factor of the detector. Even in the present circumstances where the conversion is (under the assumptions of Appendix A) quite insensitive to these, we prefer to carry out the bulk of the data analysis in terms mathematically equivalent to the directly observed counting rates.

From among the possible representations of the counting rate information (including counting rate, log counting rate, and square root of counting rate) the square root of the observed counting rate, Y, has been selected as the dependent variable. On the hypothesis that the number of counts in a given 11-second counting interval at any given position in space is a random variable with a Poisson distribution, it can be shown that the variance of Y is approximately constant, independent of its average value (see Appendix B.2). The least squares criterion has been used in all the estimating procedures; that is, coefficient estimates have been selected so that the sum of squares of dif-

Table I—Coordinates, Variables and Notation

The redundent use of a few symbols is partly due to the decision to retain "standard" notation in both geophysics and statistics. The context should resolve any apparent ambiguities. Some symbols used locally in the text are not included in this table.

Symbol	Coordinate	Units	Source	Underlying variables	Remarks
Radiation Intensity					
J	Fitted average omnidirectional flux	protons/cm^2 sec	. . .	y, $\bar{y}$	Equation (21).
j	Predicted unidirectional flux	protons/cm^2 sec ster	. . .	y, $\bar{y}$	Equation (8).
Y, Y_j	Square root of observed counting rate	(counts/sec)$^{1/2}$	telemetry	Z	. . .
y	Fitted average value of Y	(counts/sec)$^{1/2}$	least squares fit	Y, x, L	Section IV. This symbol is used generically for all the models.
Z	Counts in an 11-second counting interval	counts	telemetry	. . .	Random variable.
Position and Orientation					
B	Magnetic induction	gauss	INVAR	r, θ, ϕ	Computer program INVAR by McIlwain[12] containing the Jensen and Cain[13] magnetic field coefficients for 1960. $R_e = 6371.2$ km.
B	Magnetic field strength	gauss	$\lvert\mathbf{B}\rvert$	r, θ, ϕ	. . .
B_0	Equatorial value of B	gauss	. . .	. . .	$B_0 = 0.311653/L^3 = 0.311653/R^3$.
L	Magnetic shell parameter	ratio to earth radius (R_e)	INVAR	r, θ, ϕ	See **B**, above.

TABLE I—(Cont'd).

Symbol	Coordinate	Units	Source	Underlying variables	Remarks
Position and Orientation (Cont'd)					
L_m	Midpoint of an L-slice	same as L	...	...	Section V.
R	Magnetic dipole radial distance	R_e	B, L	r, θ, ϕ	$B = \frac{0.311653}{R^3}\left\{4 - \frac{3R}{L}\right\}^{1/2}$.
R_e	Earth radii	km	Heiskanen[14]	...	6371.2 km.
r	Geocentric distance	earth radii (R_e)	ephemeris	tracking data	For geomagnetic calculations, r is corrected to altitude above the International Ellipsoid [Heiskanen[14]]. R_e = 6371.2 km.
T	Universal time	days	clock at telemetry receiving station	...	Measured in days from 0 hr 0 min. U. T., Jan. 0, 1962.
t	Local time	hours	...	T, ϕ	Apparent sun time (local mean time corrected for the equation of time taken from the American Ephemeris and Nautical Almanac[15]).
x	$\left[1 - \frac{0.311653}{BL^3}\right]^{1/2}$	dimensionless	B, L	r, θ, ϕ	See above for B and L.
α_o	Equatorial pitch angle	degrees	...	...	Fig. 1.
γ	Angle between satellite spin axis and local magnetic vector	degrees	$\mathbf{B}$, $\boldsymbol{\omega}$	B, χ, δ	$\gamma = \mathbf{B}\cdot\boldsymbol{\omega}/\lvert\mathbf{B}\rvert$, where $\boldsymbol{\omega}$ is a unit vector parallel to the angular momemtum vector of the satellite.
δ	Declination of the satellite spin axis	degrees	mirror flash data	r, θ, ϕ, T, and astronomical data	Optical observations of the reflection of the sun from mirrors on the satellite, Courtney-Pratt, et al[8].

TABLE I—(Cont'd).

Symbol	Coordinate	Units	Source	Underlying variables	Remarks
Position and Orientation (Cont'd)					
θ	Colatitude	degrees	ephemeris	tracking data	geocentric angle.
λ	Magnetic dipole latitude	degrees	B, L	r, θ, ϕ	$\lambda = [\text{arc} \cos(R/L)]^{1/2}$
μ_0	Cos α_0	dimensionless	…	…	Numerically equal to x.
ϕ	East longitude	degrees	ephemeris	tracking data	Geocentric angle.
χ	Right ascension of the satellite spin axis	degrees	mirror flash data	r, θ, ϕ, T, and astronomical data	See δ, above.
ω	Direction of the spin angular momentum vector of satellite	dimensionless	mirror flash data	χ, δ	See δ, above.
Instrument and Energy Spectrum					
E	Energy	MeV	…	…	…
E_0	e-folding energy	MeV	…	…	Used in energy spectrum, Appendix A.
g	Geometric factor of the detector	cm² ster	detector geometry	…	…
$\bar{g}$	Average geometric factor of detector	cm² ster	detector geometry	proton energy spectrum	Equation (20).
M	Exponent of integral power-law energy spectrum	dimensionless	…	…	…
N	Number of protons	dimensionless	…	…	…
n	Exponent of differential power-law energy spectrum	dimensionless	…	…	…
v_b	Bias voltage	bits	telemetry	resistor calibration	Each bit represents a step of -1.108 volts.
τ	Skin temperature	°C	telemetry	thermistor calibration	Measured near the detector.

TABLE I—(Cont'd).

Symbol	Coordinate	Units	Source	Underlying variables	Remarks
Mathematical Model					
A, A', A'', A''' A^{iv}	Equatorial value of y	$(\text{counts/sec})^{1/2}$	fitting	L	The superscripts indicate various models, see Section IV. In particular A' indicates Model I and A'' indicates Model II. N.B. A is used generically for all the models, or when the distinction is unimportant or clear from the context.
A_p	Coefficient	$(\text{counts/sec})^{1/2}$	fitting	...	Maximum value of A'' (and therefore y''), Model II, Equation (11).
a_1, a_2, a_3, a_4, a_5	Coefficients	...	fitting	...	Coefficients of A'' and A^{iv}, Equations (6) and (16).
b	...	dimensionless	...	x, (L)	Equation (18).
e_i	Coefficients	...	...	L	Equation (18).
F	...	dimensionless	...	L, (x)	Equation (19).
G, G', G'', G'''	...	dimensionless	...	x, (L)	Describes the x-dependence of y for the models indicated by the superscripts, see Section IV. N.B. G is used generically for all the models, or when the distinction is unimportant or clear from the context.

TABLE I—(Cont'd).

Symbol	Coordinate	Units	Source	Underlying variables	Remarks
Mathematical Model (Cont'd)					
L_o	Coefficient	same as L	fitting	...	Smallest value of L for which $y > 0$.
L_p	Coefficient	same as L	fitting	...	Position of A_p is at $(x, L) = (0, L_p)$.
L_1	Coefficient	same as L	fitting	...	Equation (16).
M	Coefficient	dimensionless	fitting	L	Model III, Equation (15).
P	Coefficient	dimensionless	fitting	L	Model III, Equation (15).
p_i	Coefficients	...	...	x	Equation (19).
Q	Coefficient	dimensionless	fitting	L	Model III, Equation (15).
R_c	R at cutoff	R_e	fitting	L	Equation (4).
$r_1, r_2, r_3, (r_4), (r_5)$	Coefficient	...	fitting	...	Coefficients of R_c, Equation (5).
S	Shape factor	dimensionless	fitting	L	Equation (3).
s_0, s_1	Coefficient	...	fitting	...	Coefficients of S, Equation (3).
x_c	Cutoff function	dimensionless	fitting	L	Smallest value of x for which $y = 0$, Equation (4).
y, y_L, y', y'', y'''	Fitted average value of y	(counts/sec)$^{1/2}$	fitting	x, L	The subscript and superscripts indicate various models, see Section IV. In particular y' indicates Model I and y'' indicates Model II. N. B. y is used generically for all the models, or when the distinction is unimportant or clear from the context.
y_j	Fitted value	(counts/sec)$^{1/2}$	fitting	x, L	Corresponds to the observation Y_j.
η	Coefficient	dimensionless	fitting	...	Shape factor, Equations (6) and (11).

TABLE I—(Cont'd).

Symbol	Coordinate	Units	Source	Underlying variables	Remarks
Other					
CB	Complete body (of data)	. . .	. . .	. . .	Designates all the data, see Section 4.5.
HTB	High temperature and high bias voltage (data)	. . . . . .	. . . . . .	. . . . . .	Designates a subset of the data, see Sections 4.5 and 6.9.
Statistics					
Cov	Covariance	. . .	. . .	. . .	. . .
df	Degrees of freedom	dimensionless	. . .	. . .	See Wilks[16].
D_1^2, D_2^2	Squared distance	. . .	. . .	. . .	Appendix B.6.
g	Function	. . .	. . .	. . .	. . .
h	Function	. . .	. . .	. . .	. . .
n	Number of observations	. . .	. . .	. . .	. . .
R^2	Squared multiple correlation coefficient	. . .	. . .	. . .	. . .
Res, RES	Residual	. . .	. . .	. . .	Observed minus fitted.
SS	Sum of squares	. . .	. . .	. . .	. . .
u_j	Function of Y_j	. . .	. . .	. . .	. . .
$\bar{u}$	Mean of u_j	. . .	. . .	. . .	. . .
Var	Variance	. . .	. . .	. . .	Wilks[16].
w	Independent variable (vector)	. . .	. . .	. . .	. . .
w_i	Components of w	. . .	. . .	. . .	. . .
z	Values of the random variable Z	counts	. . .	. . .	. . .
α	Dependence coefficient	. . .	. . .	. . .	$\alpha = [1 - \sqrt{1 - \rho^2}]\,\mathrm{sign}\,(\rho)$, Wilk[17]. Equation (31).
β_i	Confidence coefficient	. . .	. . .	. . .	Wilks[16].
$\tilde{\delta}$	Correction to $\hat{\theta}$ (vector)	. . .	. . .	. . .	. . .

TABLE I—(Cont'd).

Symbol	Coordinate	Units	Source	Underlying Variables	Remarks
Statistics (Cont'd)					
$\tilde{\delta}_i$	Component of $\tilde{\delta}$	...	...	...	...
θ, θ'	Coefficient vector	...	...	...	...
θ_i	Component of θ'	...	...	...	...
$\hat{\theta}$, $\tilde{\theta}$	Estimate of θ'	...	...	...	...
$\hat{\theta}_i$	Components of $\hat{\theta}$	...	...	...	Estimates of θ_i.
ν	Average value of a Poisson variable	counts	...	...	...
ρ	Correlation coefficient	dimensionless	...	...	...
σ	Standard deviation	...	...	...	...
MSD MSE MSR	The terms, mean square error (MSE), mean square residual (MSR) and mean square deviation (MSD) are used in this document to denote related but different entities, each measuring "goodness of fit" in relation to different situations. When a selected array of data is fitted by a model, the minimum sum of squares of residuals from the fit of those data divided by the degrees of freedom (number of selected observations minus number of coefficients fitted) is termed the MSE. When a fit based on a sample of data is used to generate residuals for all of the data, without refitting, the total sum of squares of these residuals divided by the number of residuals is termed the MSR. For defined "small" cells in x,L space, the sum of squares of deviations of observations from their average in the cell divided by the number of such deviations minus one is termed the MSD.				

ferences between observed and fitted values is minimized. The choice of the square root scale, Y, as the scale on which to represent the counting rate data makes troublesome differential weighting of the data in the least squares fitting unnecessary. Similarly, plots of Y versus various variables are convenient since the scatter in Y is approximately independent of the value of Y. In fact, the square root transformation will make the variance of the observation approximately independent of its average value whenever the variance is proportional to the mean. Thus, the procedure is more robust than the assumption of a Poisson distribution, for which the variance equals the mean. Further discussion and detail is given in Appendices B.2 and C.

The results were restored to counting rate and the flux was calculated using the best estimate of the average geometric factor, $\bar{g}$, (see Appendix A) to facilitate the discussion of the physical significance of the measurements.

IV. THE EVOLUTION OF THE MODELS

4.1 *General Approach*

This section provides a summary overview of the evolution of the models, the details and accomplishments of which are elaborated in the following sections and appendices.

The approach to model development in this study has been largely empirical. Theoretical physics considerations are currently too complex and speculative to do more than serve as a general guide and stimulus. We have proceeded on the presumption that an adequate model for the spatial distribution of the high-energy protons can be based on the mapping of the earth's magnetic field onto a two-dimensional axially symmetric dipole field, expressed, for example, in the coordinates x and L. This is supported by the plots of Fig. 3, the successful polynomial fits on L-lines of McIlwain,[18] Valerio,[19] and Fillius,[20] and by the results of the present study.

The ultimate justification of the mathematical models developed herein is that, when appropriate estimates of coefficients are inserted, good fits to the data are obtained. Various other mathematical, physical, and statistical considerations also provided guidance and evaluation.

The evolution involved successive interactions with the data and iteration on models. Roughly, the main stages included: grouping the data into L-slices; inferring a mathematical function having adjustable coefficients which would fit a selected series of L-slices; developing a mathematical function to describe the dependence of the L-slice coefficients on L; thence fitting the two-dimensional model so-defined to a sample of the data; using this fit to screen outliers, to detect instrumental effects and, after partitioning the data, to select a representative sample of partitioned data for further fitting; after obtaining a very good fit to the partitioned data, some remaining physical and statistical defects of the model were overcome by a reparametrization and specialization. Further generalizations of the model were also tested.

4.2 *The L-slice Model*

As a developmental operational procedure (encouraged by the L-shell orientation of the adiabatic theory[11]) the data were grouped into a series of narrow bands according to L values (e.g., $1.849 \leqq L \leqq 1.851$) and plotted versus x. Retrospectively, there is every reason to believe that an initial approach based on grouping the data into x-slices would also have led to an effective analysis (see Section 13.2). Various functional forms, having adjustable coefficients dependent on L, were tested for adequacy of fit to the L-slices.

Initially, we employed the functional form

$$y_L(x) = \begin{cases} A \cdot G(x; x_c, S) & (x \leqq x_c), \\ 0 & (x > x_c), \end{cases} \tag{1}$$

where A, x_c and S are fitted coefficients for each L-slice, and

$$G(x; x_c, S) = \begin{cases} (1 - x^2)^{-\frac{1}{4}}\left[1 - \left(\dfrac{x}{x_c}\right)^2\right]^{S+\frac{1}{4}} & (x \leqq x_c), \\ 0 & (x > x_c). \end{cases} \tag{2}$$

For this body of data from the region $\{R \leqq 1.95\, R_e\,, 1.15 \leqq L \leqq 3.0\}$, we have found this $y_L(x)$ function provides an adequately flexible model on L-slices, for appropriately fitted values of the coefficients A, x_c, and S. In this representation for given fixed L, the quantity A^2 may be interpreted as the average equatorial omnidirectional counting rate, since $x = 0$ on the equator, x_c represents a "cutoff" value for x, i.e., the cosine of the equatorial pitch angle corresponding to the "loss cone", and S has the effect of a shape factor in the y,x dependence.

The analysis using this $y_L(x)$ model is described in Section V.

4.3 *Dependence on L*

The $y_L(x)$ model was fitted to a series of L-slices, obtaining fitted values of A, x_c and S. These were each plotted against the nominal (mid-range) L value for the slice and a reasonably smooth variation with L obtained.

Thence we inferred the following functional dependence of the L-slice coefficient estimates on L:

$$S = S(L) = s_0 + s_1 L, \tag{3}$$

$$x_c = x_c(L) = \sqrt{1 - \left(\frac{R_c}{L}\right)^3 \left[4 - 3\frac{R_c}{L}\right]^{-\frac{1}{2}}}, \tag{4}$$

$$R_c = R_c(L) = L_0 + r_1(L - L_0) + r_2(L - L_0)^2 + r_3(L - L_0)^3, \tag{5}$$

$$A = A'(L) = \begin{cases} \dfrac{a_1(L - L_0)}{a_2 + (L - a_3)^\eta} & (L \geqq L_0), \\ 0 & (L < L_0), \end{cases} \tag{6}$$

where s_0, s_1, r_1, r_2, r_3, a_1, a_2, a_3, η and L_0 are fitted coefficients.

Equation (4) simply expresses the mathematical relationship between R (or R_c) and x (or x_c) in the magnetic dipole field (see Table I). The coefficient L_0, which occurs in $A'(L)$ and $x_c(L)$, may be interpreted as the lower bound of the L shells on which protons with energies above 50 MeV were measurable. The quantity $R_c(L)$ is such that $R_c(L) - 1$ is the equivalent dipole altitude at which the counting rate falls to zero.

4.4 *A Two-Dimensional Model—Model I*

The conjunction of (1) to (6) defines a two-dimensional model, referred to henceforth as Model I,

$$y'(x, L) = A'(L)\cdot G'(x, x_c(L), S(L)), \tag{7}$$

where G' is essentially the function G of (2), with x_c and S explicitly dependent on L.

Though empirical considerations mainly guided the choice of these functions, some physical and mathematical properties influenced the choice. In the present case, in which the geometric factor of the detector is considered to be independent of the energy spectrum (see Appendix A), $[y(x, L)]^2$ transforms in closed form to the equatorial pitch angle distribution, giving[10]

$$j(\mu_0, L) = \frac{4\pi}{\bar{g}} \frac{[A(L)]^2 \left\{1 - \left[\frac{\mu_0}{x_c(L)}\right]^2\right\}^{2S(L)}}{2\pi x_c(L) \beta(\frac{1}{2}, 1 + 2S(L))}, \tag{8}$$

where $j(\mu_0, L)$ is the predicted equatorial unidirectional flux (protons/cm^2 sec ster) at equatorial pitch angle $\alpha_0 = \text{arc cos } \mu_0$, and β is the beta function,

$$\beta(p, q) = \int_0^1 u^{p-1}(1 - u)^{q-1} \, du. \tag{9}$$

In addition $y'(x, L)$ has good boundary behavior. The derivative at the magnetic equator, $\partial y'(0, L)/\partial x$, is 0, which provides continuity. When $\frac{1}{4} < S(L) < \frac{3}{4}$, then $\partial y'(x_c, L)/\partial x \rightarrow -\infty$ and $\partial[y'(x_c, L)]^2/\partial x = 0$. The estimated values of S do satisfy this constraint in the present case. The desirable consequences of this behavior of the derivatives will be discussed in Section V. The function $y'(x, L)$ gives smooth interpolation over regions sparse in data, and does not have any of the wild fluctuations often associated with polynomial fits.

The analysis of the data using Model I is described in Section VI.

4.5 *Summary Uses of Model I.*

The unspecified coefficients of Model I were estimated by nonlinear least squares fitting to a sample of about 1000 observations from the complete body of data. Thence this fit of Model I (the CB fit) was evaluated relative to all the data and to auxiliary variables, such as time, which were not included in the model. Outliers were thereby detected and screened. An instrumental effect was uncovered (see Section 6.8), and this led to an objective partitioning of the data, yielding a subset (HTB data) for further analysis. The CB fit of Model I was also used to specify a representative data sampling procedure for further fitting to the HTB data.

Though Model I produces a very good fit to the HTB data (see Section VII), it has certain physical and statistical defects. Specifically, though the quantities A and x_c in the L-slice model have a direct physical interpretation, most of the coefficients in $y'(x, L)$ do not. Additionally, the estimates of the coefficients in $A'(L)$ turn out to have exceedingly high statistical correlations and the model $y'(x, L)$, as a function of the coefficients, exhibits marked nonlinearities even in a close neighborhood of the least squares estimates (see Section 8.5).

Therefore, after clarifying the character of the data and obtaining a good fit, attention was given to additional improvements of the model.

4.6 *A Modified Model—Model II*

The statistical difficulties of Model I were entirely overcome by employing a specialized version of $A'(L)$, defined below. Furthermore, this specialized model, Model II, retains all the desirable properties of Model I while providing both aesthetic improvement and greater physical interpretability.

Model II is defined by

$$y''(x, L) = A''(L) \cdot G''(x, x_c(L), S(L)), \tag{10}$$

where G'' is as in (2), but with $S(L) = s_0$, and

$$A''(L) = \begin{cases} \dfrac{A_p(L - L_0)}{\dfrac{(\eta - 2)}{\eta}(L_p - L_0) + \dfrac{2}{\eta}\dfrac{[(L_p + L - 2L_0)/2]^\eta}{(L_p - L_0)^{\eta - 1}}} & (L \geqq L_0), \\ 0 & (L < L_0), \end{cases} \tag{11}$$

where A_p, L_0, L_p and η are the coefficients to be estimated.

$A''(L)$ is a special case of $A'(L)$ and relates to it by the following transformations:

$$\begin{aligned} L_0 &= L_0 \\ \eta &= \eta \\ a_3 &= 2L_0 - L_p \\ a_2 &= 2^{\eta-1}(\eta - 2)(L_p - L_0)^\eta \\ a_1 &= 2^{\eta-1}A_p\eta(L_p - L_0)^{\eta-1}. \end{aligned} \tag{12}$$

Indeed, Model II is essentially defined by the following nonlinear constraint imposed on Model I:

$$a_2 = 2^{\eta-1}(\eta - 2)(L_0 - a_3)^\eta. \tag{13}$$

The coefficients of $A''(L)$ in Model II have the following physical interpretations:

L_0	(as before) is the smallest value of L such that high-energy protons are measurable by the instrument;
A_p	is the square root of the maximum counting rate of high-energy protons in the radiation belt;
L_p	is the value of the magnetic shell parameter (on the equator, $x = 0$) at the highest radiation intensity;
η	may be interpreted as a shape factor for the equatorial (counting rate)$^{\frac{1}{2}}$ function, $A''(L)$.

The model $A''(L)$ has the form of a product, with the maximum value, A_p, being multiplied by a factor which decreases as L departs from L_p in either direction. Note that the factor multiplying A_p is dimensionless.

The other fitted coefficients of Model II are s_0, which is a shape factor for the dependence of (counting rate)$^{\frac{1}{2}}$ on x at constant L, and r_1, r_2 and r_3 which, with L_0, define the cutoff function $x_c(L)$.

The analysis of the HTB data using Model II and comparisons of Models II and I are considered in Section IX.

4.7 *Generalizations*

The previously defined models may be regarded as special cases of Model III defined by

$$y'''(x, L) = A'''(L) \cdot G'''(x, x_c(L), M(L), P(L), Q(L)), \tag{14}$$

where $A'''(L) = A'(L)$, defined in (6),

$$G''' = \begin{cases} \left[1 - \left(\dfrac{x}{x_c(L)}\right)^{M(L)}\right]^{P(L)} \Big/ (1 - x^2)^{Q(L)} & (x \leqq x_c), \\ 0 & (x > x_c), \end{cases} \tag{15}$$

$x_c(L)$ is as defined in (4), and $M(P)$, $P(L)$ and $Q(L)$ involve coefficients or functions to be fitted.

The function G' is a special case of G''', in which $M(L) = 2$ and $Q(L) = \frac{1}{4}$. This permits a closed form transformation to an equatorial pitch angle distribution. The function G'' additionally constrains $P(L) = s_0$, independent of L.

The more general G''' in Model III can be used on L slices to determine L-slice estimates of M, P, Q, as well as A and x_c, and these in turn inspected to infer functional dependence on L. Clearly, this more general form must lead to at least as good a fit as Models I or II. Work has been done with Model III[21] but no important improvement over Model II was obtained for this body of data.

Neither of the fitted models $y'(x, L)$ nor $y''(x, L)$ is applicable far outside the spatial and energy regions that include the data analyzed here. For example, Models I and II do not fit well to the 26–33 MeV protons measured by the *Telstar*® 1 satellite, nor are they suitable for fitting many of the electron distributions. Preliminary investigations indicate that these remarks may not apply to G$'''$, whose additional coefficients allow more rapid changes in curvature as a function of x.

We have already shown for *Telstar*® 2 data[5] that $A(L)$ can be extended to include description of the plateau of high-energy protons reported by McIlwain[18, 22] near the equator at $R \approx 2.2\ R_e$, beyond the orbital extremes of the *Telstar*® 1 satellite. The extension was made by adding a term to $A'(L)$, (6), to give A^{iv} defined by

$$A^{iv} = A'(L) + a_4 \exp\left[-\frac{(L - L_1)^2}{a_5}\right], \tag{16}$$

where a_4, a_5, and L_1 are coefficients describing the equatorial distribution of the "excess" protons that give rise to the plateau. In the less stable parts of the radiation belts the early work on empirical time dependence presented by Gabbe and Brown[5] clearly requires extension.

V. FITS ON THE L-SLICES

The model of (1) and (2) was fitted to the data, on the scale of Y, in 92 individual L-slices, using a nonlinear, multidimensional, least squares, computer program (see Appendix B) to estimate the coefficients and produce various statistical measures. The procedure of fitting to L-slice data enabled one to test functional forms of $y_L(x)$ and then to evolve functional forms for the dependencies of the coefficients of the L-slice models on L.

Proceeding in this manner, however, has a number of possible pitfalls. In particular, the estimates of coefficients within an L-slice may be highly correlated, and the reliability of the actual values of the estimated coefficients also depends on the pattern of data points in the particular L-slice, e.g., whether or not there are points near x_c. Hence, the estimated values for any particular coefficient may not exhibit a smooth dependence on L.

The form of the L-slices whose middle values of L, called L_m, are 1.35, 1.801, 2.2015, and 1.79, respectively, are displayed in Figs. 4 to 7. The thin solid lines in the figures are the fits to the L-slice data (meaning of the dashed and thick solid lines will be taken up later). The numerical values of the coefficients of the fits, and the widths of the slices are given in Table II. Figs. 4 and 5 are examples of the high quality of fit which is typically obtained for L-slices having $L_m < 2$.

In Figs. 4(a) and 5(a), square root of counting rate is plotted against x. One sees that the fit to the data points (the thin solid line) is quite adequate. The cutoffs, x_c, are well-defined, the scatter in Y is approximately independent of y and the data are well-distributed in x.

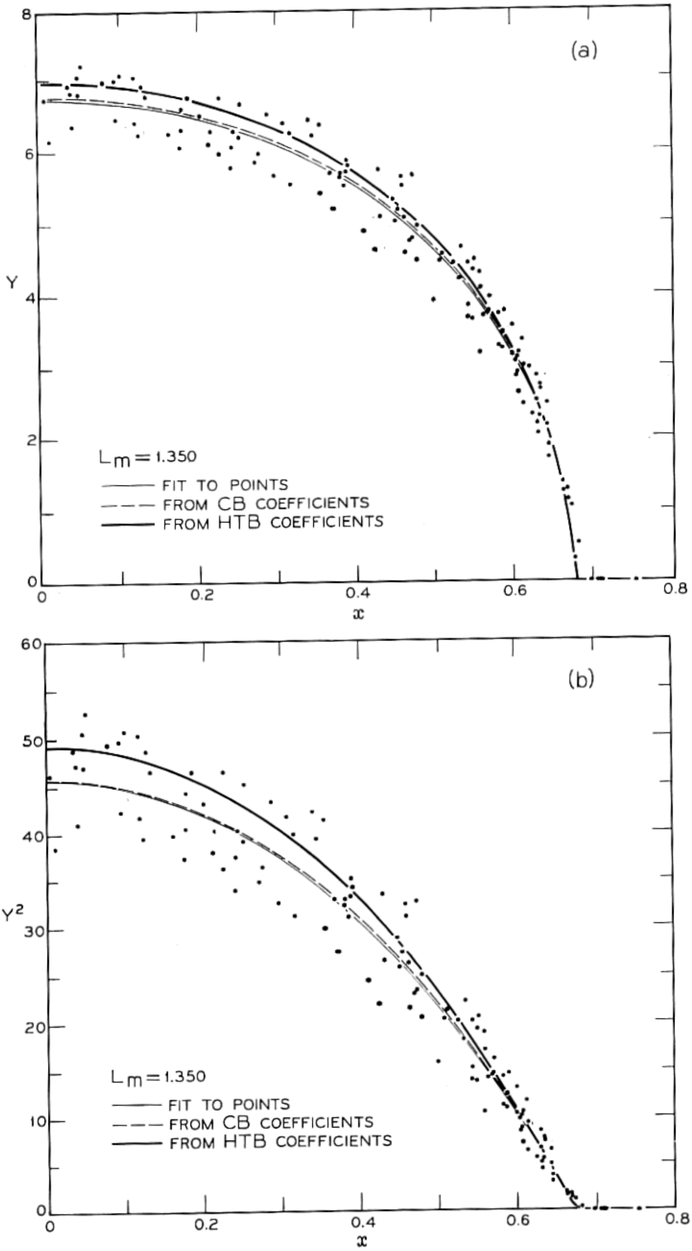

Fig. 4 — Data from the L-slice centered at $L_m = 1.35$ and the results of three fits shown on four scales.

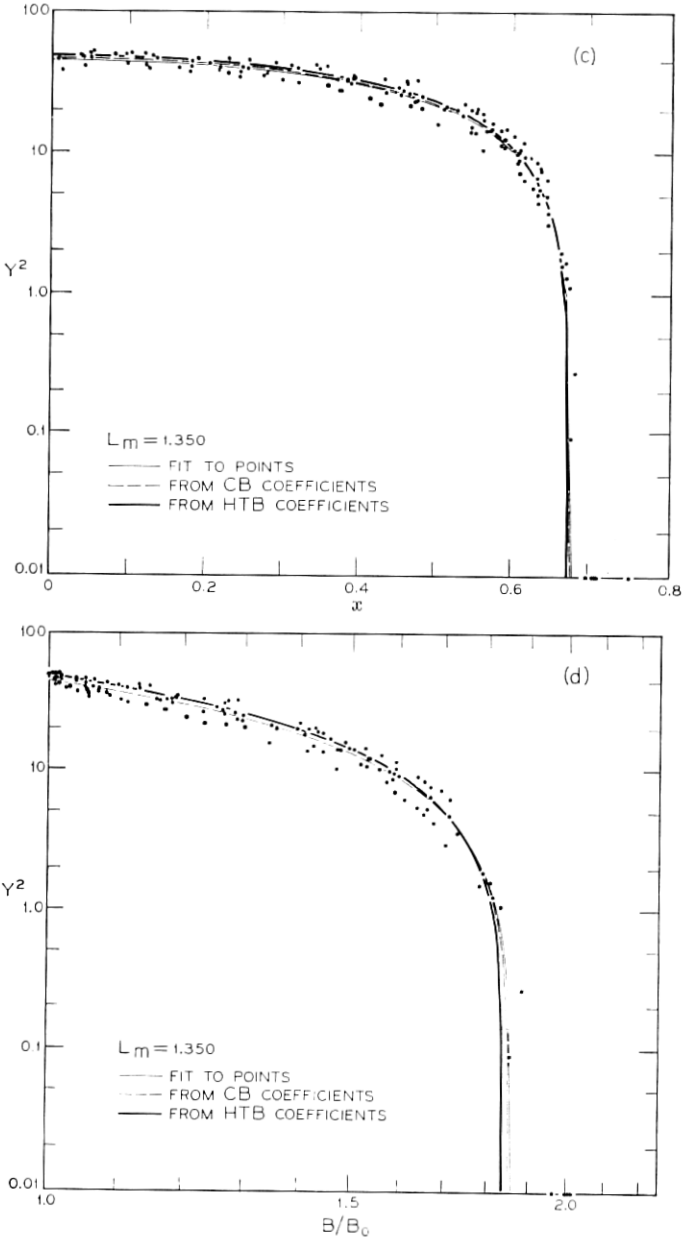

Fig. 4 — (continued)

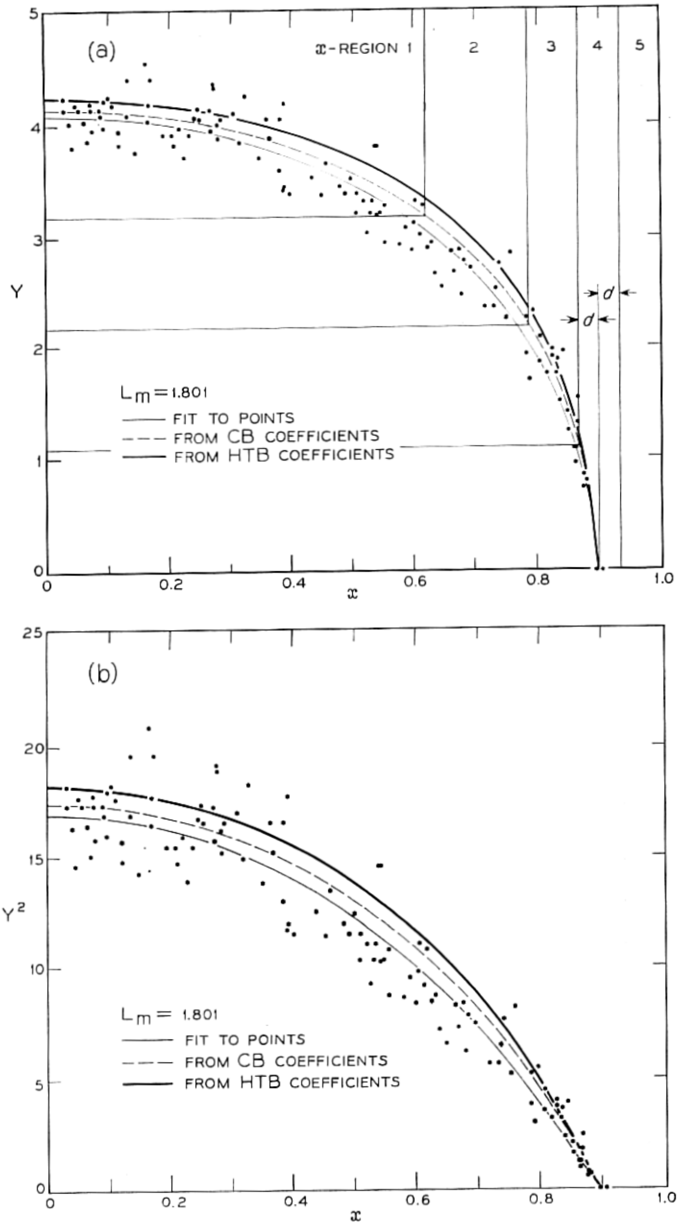

Fig. 5 — Data from the L-slice centered at $L_m = 1.801$ and the results of three fits shown on four scales. The partitioning in (a) is discussed in Section 7.1.

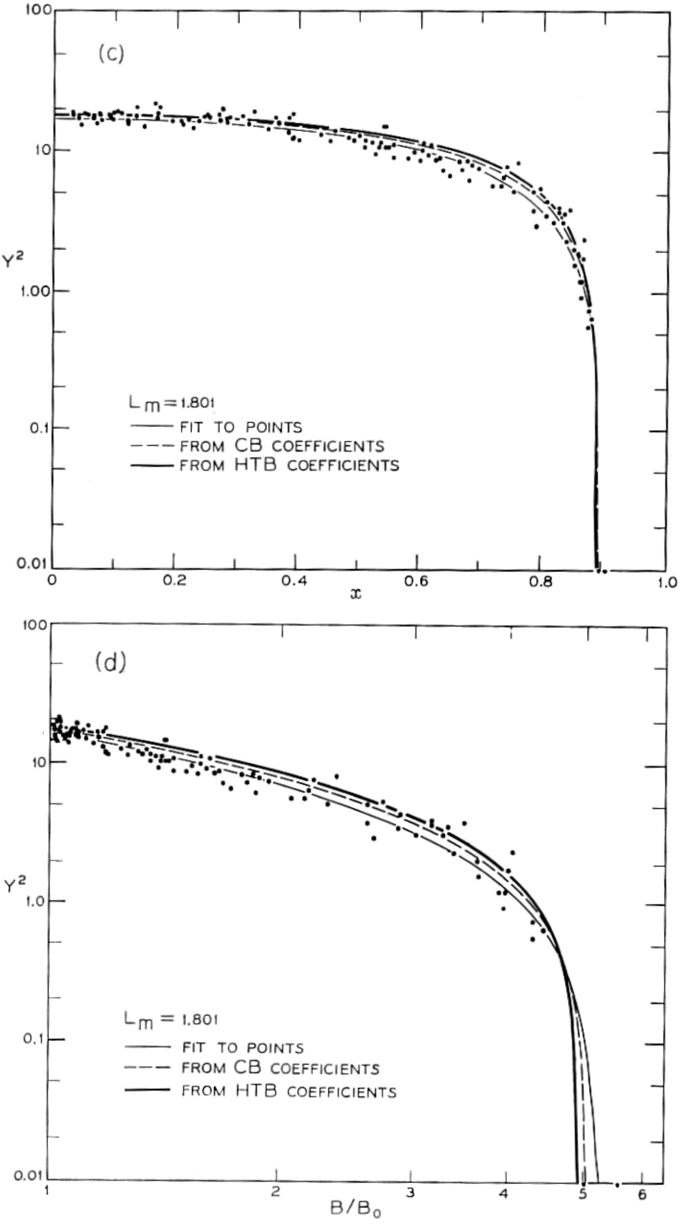

Fig. 5 — (continued)

Table II—Coefficients and Statistics of the L-Slice Fits.

L_m	1.35	1.801	2.2015	1.79
L_{MIN}	1.346	1.800	2.200	1.7895
L_{MAX}	1.354	1.802	2.203	1.7905
ΔL	0.008	0.002	0.003	0.001
A	6.757	4.109	1.70	4.324
$\sigma(A)$	0.053	0.031	0.12	0.043
x_c	0.6795	0.8998	0.954	0.923
$\sigma(x_c)$	0.0027	0.0044	0.011	0.015
S	0.324	0.390	0.58	0.478
$\sigma(S)$	0.018	0.024	0.10	0.060
Number of pts	140	129	144	65
MSE	0.1125	0.0497	0.0282	0.0478
Correlation coefficients				
A with x_c	0.281	0.309	0.724	0.408
A with S	0.605	0.561	0.940	0.548
x_c with S	0.774	0.820	0.890	0.944

As the cutoff is sharp on the scale of y, it is convenient to have a function which has an infinite derivative at x_c. Otherwise the exact x at which $y \rightarrow 0$ may have relatively little effect on the mean square error of the fit. This would lead to an ill-defined value for x_c, even though the data allows one to evaluate the position of the cutoff quite precisely for L values smaller than ≈ 1.9.

In Figs. 4(b) and 5(b), the counting rate, Y^2, is plotted against x. The thin solid lines represent the same fits as those in Figs. 4(a) and 5(a). One finds that the position of the cutoff is no longer well-defined on the plot. Instead the counting rate fades away as x increases. Having the derivative of y^2 equal zero at the cutoff (as noted in the previous section) is suitable in this situation. The scatter in Y^2 now changes with y^2, and is greater for large values of y^2 (small values of x). This nonuniform scatter makes it more difficult to judge the appropriateness of fit. If one wished to minimize the squared deviations between observed and fitted in terms of y^2 (or log y^2) the values of Y^2 (or log Y^2) would have to be weighted inversely as their estimated approximate variance, with a loss of intuitive appreciation of the quality of fit from a scatter plot and a substantial inconvenience in carrying out the fitting procedure.

In Figs. 4(c) and 5(c) the ordinate is log y^2. This choice of coordinate restores the ability to discriminate in the vicinity of the cutoff at the cost of a large loss of sensitivity in regions where the counting rate is higher.

Finally, Figs. 4(d) and 5(d) display the same data in the coordinate system log y^2, log (B/B_0). This choice of abscissa expands the high-x region enormously, but contracts the low-x region to the point where it is impossible to see the details of the particle distribution in the vicinity of the equator $(x = 0)$. This contraction would be even more severe if the abscissa were B or B/B_0.

In the region defined by $\lambda < 45°$, which covers the high energy proton data, the coordinate x provides adequate detail (see Ref. 10 for further discussion). If, however, the data had extended to $\lambda > 45°$ another choice of magnetic coordinate would have been desirable for $x > 0.95$, because all $\lambda > 45°$ are crowded into x values between 0.95 and 1.

The standard errors and correlations of the coefficients of the four L-slices under discussion, together with mean square error (MSE)* of fits, are listed in Table II. The standard error is in general a relatively small fraction of the estimate and the MSE is substantially greater at small values of L_m than at larger ones. This is further analyzed in Section VI.

At $L = 2.2$ the satellite gets no closer to the magnetic dipole equator than $\lambda = 20°$. This fact, which is associated with the problem of correlation of coefficient estimates within L-slices, is displayed more emphatically by choosing x as a coordinate, as in Figs. 6(a), (b), and (c), than by choosing log (B/B_0) as in Fig. 6(d). In addition, in Fig. 6(d) the expansion of the abscissa in the region of the cutoff makes it difficult to judge the physical appropriateness of the value of x_c which results from the least squares procedure. The same difficulty is encountered to a lesser degree with Fig. 6(b). However, in Figs. 6(a) and 6(c) one judges the x-intercept of the thin solid line to be too large, and Fig. 6(a) has the additional advantage of allowing one to make a better judgment of the quality of the fit at lower values of x. As might be surmised from the high values of the correlations for $L_m = 2.2$ in Table II, the value of x_c can be adjusted to a substantial extent without much change in the mean square error. These high correlations, which typically occur for $L_m > 2$, reduce confidence in the individual estimates of the coefficients for given L-slices. This difficulty also reduces the stability of the estimates of the coefficients as L_m is changed, and precludes basing the values of $x_c(L)$ and $S(L)$, for $L > 2$, on the fits to the L-slices.

A similar difficulty may be introduced when $L < 2$ by sampling fluctuations as illustrated in Fig. 7. In this case, there is a scarcity of

---

* Some statistical terms are defined in Table I.

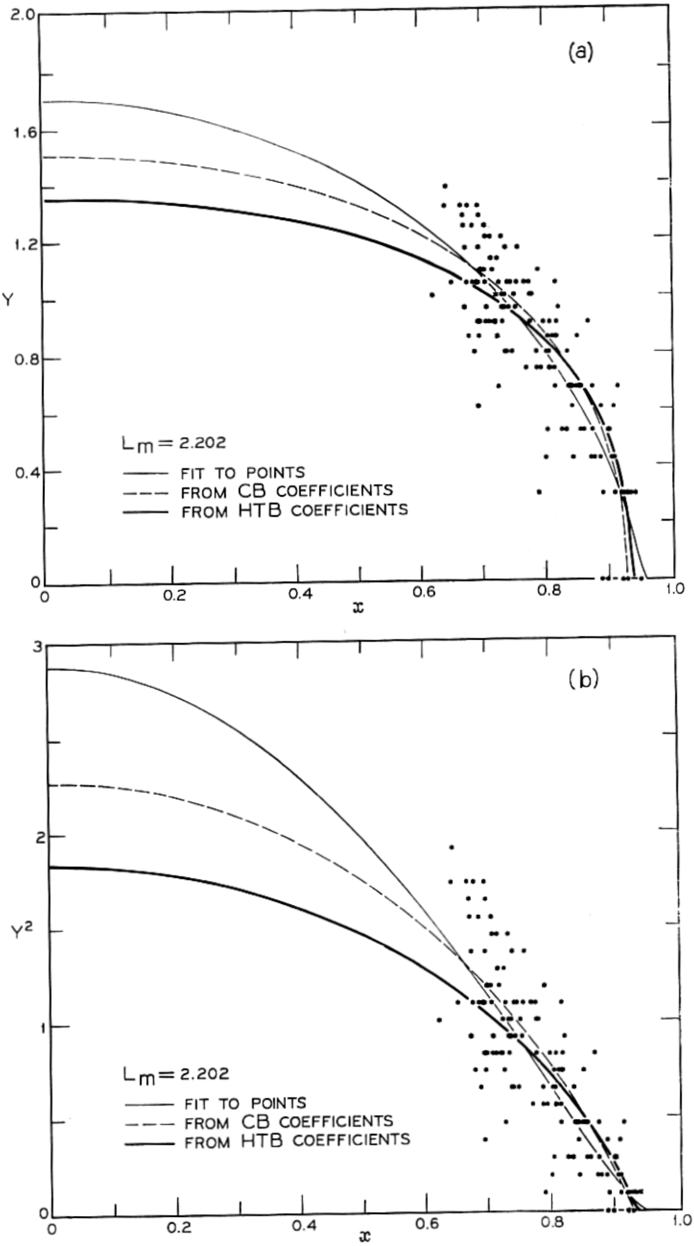

Fig. 6 — Data from the L-slice centered at $L_m = 2.202$ and the results of three fits shown on four scales.

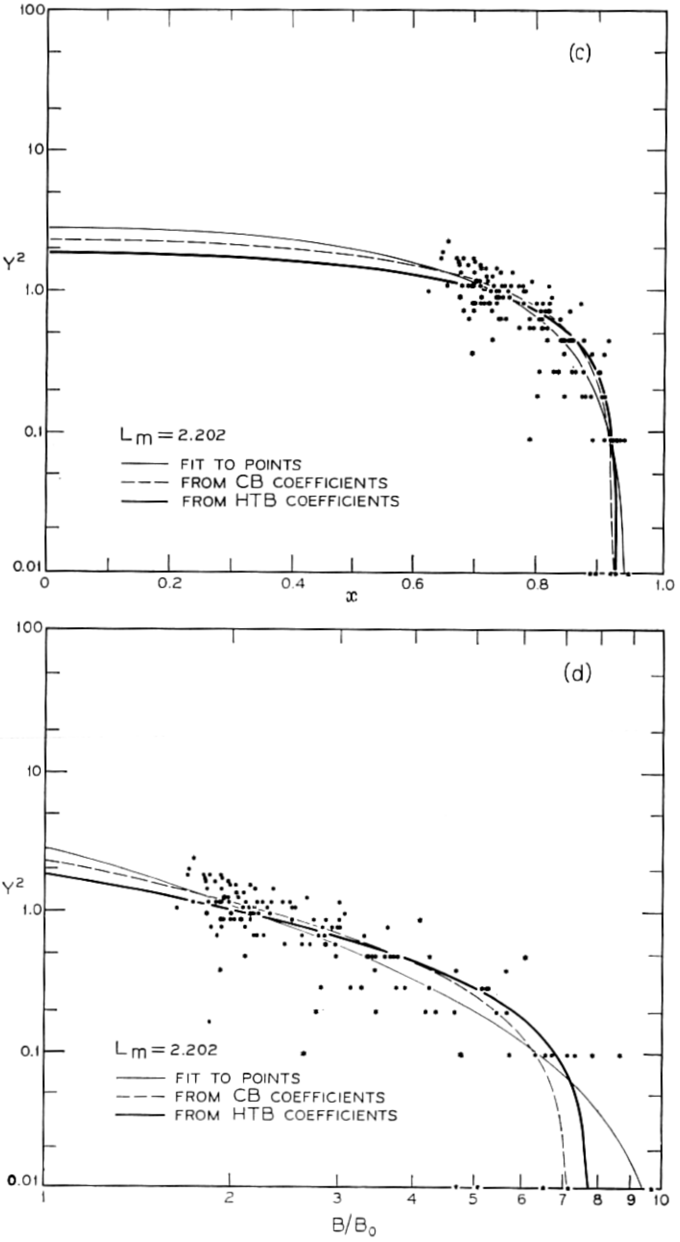

Fig. 6 — (continued)

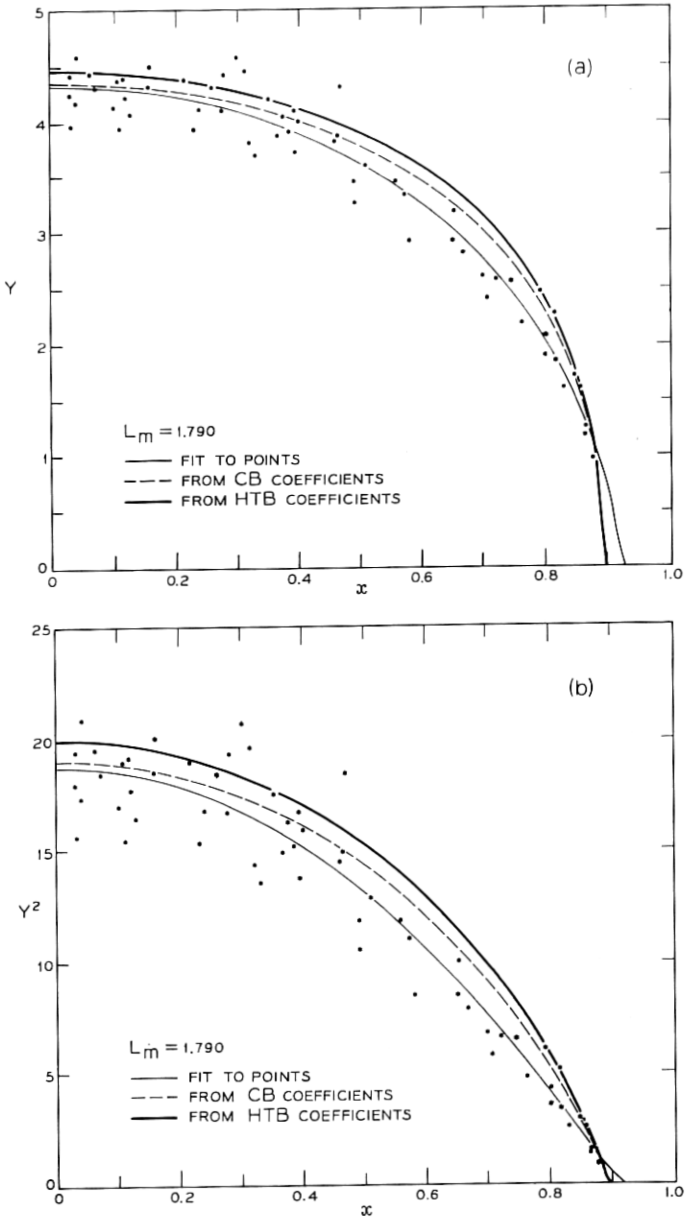

Fig. 7 — Data from the L-slice centered at $L_m = 1.790$ and the results of three fits shown on four scales.

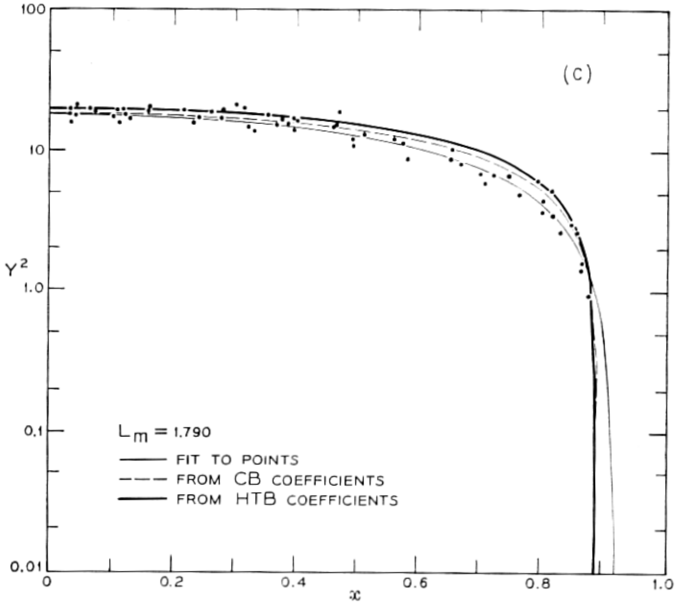

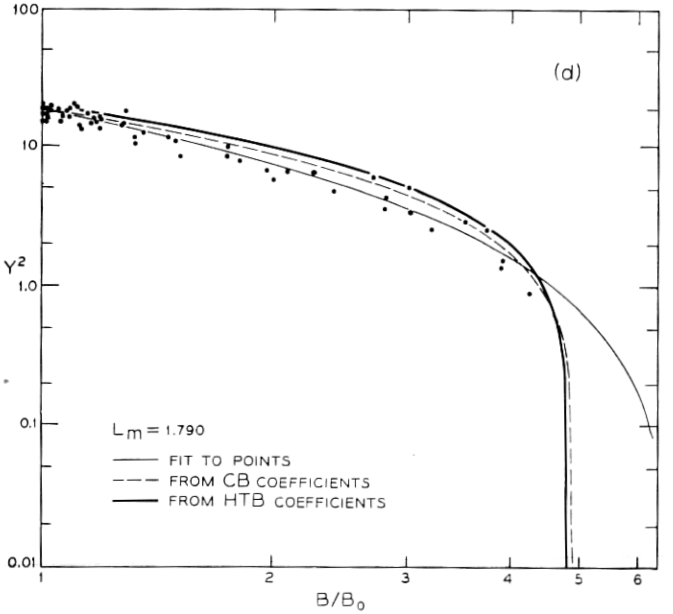

Fig. 7 — (continued)

data near and beyond the cutoff, unlike the slice with $L_m = 1.801$ illustrated in Fig. 5. The paucity of data near the cutoff in the L-slice centered on $L_m = 1.79$ both correlates and distorts the values of x_c and S. In this particular case, the width of the L-slice can be increased to avoid this difficulty, but, in general, increasing the width of the slice to include enough data may introduce a serious L-dependence within the slice. As a result, x_c may be determined by points near one extreme of L within the slice, A by points at the other extreme and S by some combination. This problem is especially severe below $L = 1.3$ where data begin to become sparse.

The plotted points in Figs. 8 to 10 summarize the dependencies of the estimates of the L-slice coefficients A, x_c, and S, respectively, on L_m, for all 92 slices. More than one value of the coefficients is plotted for some values of L_m because on occasion the width of the L-slice was

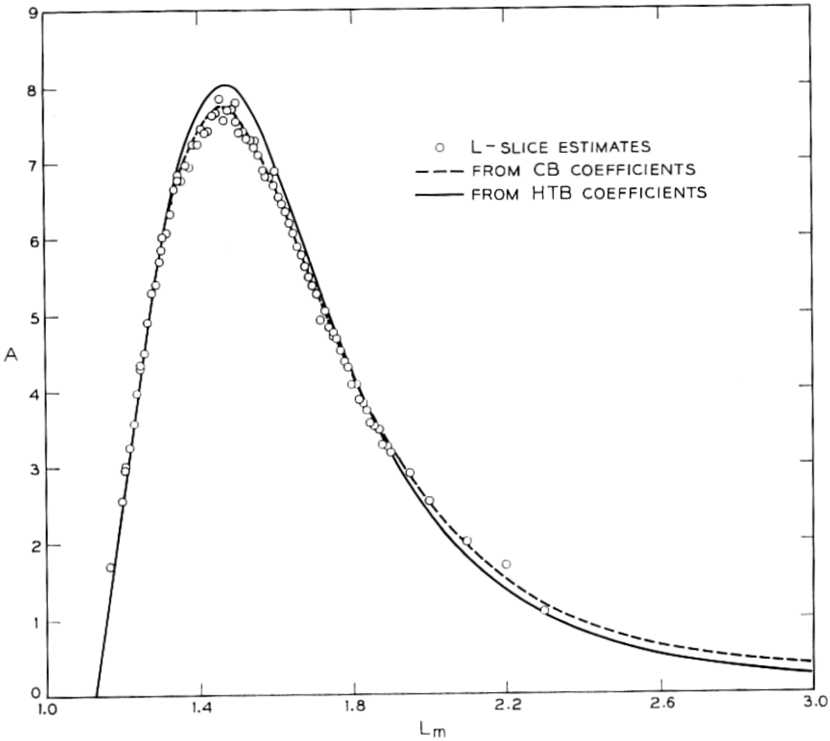

Fig. 8 — Three estimates of A as a function of L.

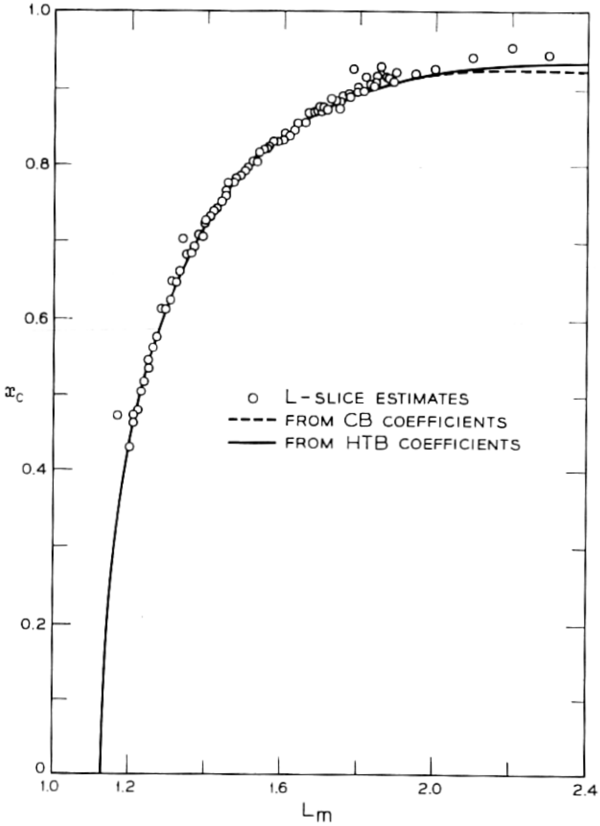

Fig. 9 — Three estimates of x_c as a function of L.

varied without changing L_m. Although there are local fluctuations in the estimates that arise from the way a narrow L-slice samples the data, the estimates exhibit a smooth dependence on L. The fluctuations are particularly pronounced near $L_m = 1.8$ in Figs. 9 and 10, and $L_m = 1.3$ in Fig. 10.

The standard errors of the L-slice estimates of A are typically 1 percent for $L < 1.95$, but become as large as 6 percent where there are no equatorial data, as is the case for $L > 1.95$. Fox x_c estimates, the standard errors are typically 0.5 percent. The estimates of S have a standard error of about 5 percent (± 0.015) near $L = 1.5$ and about 15 percent (± 0.05) near $L = 1.2$ and $L = 2$. The meanings of the curves in Figs. 8 to 10 will be discussed in the following sections.

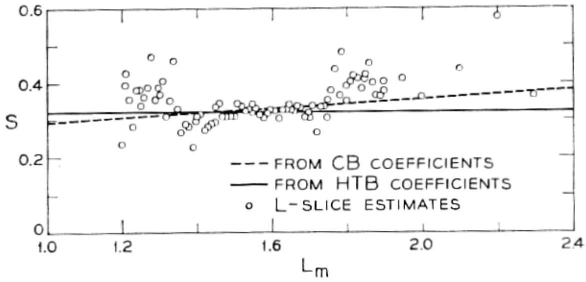

Fig. 10 — Three estimates of S as a function of L.

In summary, the L-slice approach enables one to infer a functional dependence of L-slice coefficients on L and to obtain an intuitive appreciation of the quality and nature of fit. The fitting procedure requires refinement by being carried out as a simultaneous two-dimensional process in x and L jointly. This overcomes the "grouping" inaccuracy in the L-slice approach and in addition makes good use of the data in those regions where data are scarce. The resultant function also provides convenient and excellent interpolation of data over the entire x,L region while employing a relatively small number (8, 9, or 10) of fitted coefficients.

VI. THE TWO-DIMENSIONAL FIT FOR THE COMPLETE BODY OF DATA

The analysis of this section is a precursor to the more refined parallel analysis of Section VII. This preliminary analysis produces the following results of consequence: Model I (see Section 4.4) is shown to be satisfactory; instrumental effects are identified and an objective algorithm for partitioning the data to reduce these effects is formulated; outliers are screened; and a more adequate basis for sample selection is provided. Many statistical details are omitted from this section, and statistical matters are dealt with more fully in Sections VII, VIII, and IX and in Appendices B and C.

6.1 *Sample Selection and Fit*

It was necessary, for practical computing reasons, to make a selection of approximately 1000 observations on which to carry out the simultaneous two-dimensional (in x and L) nonlinear (in the coefficients) least squares fit. In this preliminary phase, the nearly 80,000 data points were sampled by dividing the L-range from 1.15 to 3.00

into 925 contiguous intervals, each 0.002 wide. One data point was selected from each interval. As the data are approximately uniformly distributed in x (in the x-range covered by the satellite) in each L-slice (see Figs. 4 to 7), no effort was made at this point to influence the x distribution of the observations in this subset. The question of the "design" of the sample to be used as a basis for fitting the model is rather important, however, since the fit obtained with the empirical model is responsive to the distribution of data in x,L space. Other bases of sampling were employed later (see Section 7.1 and Appendix B.3).

Model I, described in Section 4.4, was fitted to the 925-point sample from the complete body (CB) of data. As this serves only as a preliminary fit, the values of the CB coefficients and other statistics are not presented here.

The quality of this fit was examined from various viewpoints: (*i*) by its behavior along the boundaries of the belt; (*ii*) by comparison with the L-slice fits; (*iii*) by plotting the residuals (observed value minus fitted value) versus the x and L coordinates; and (*iv*) by examining the mean square residuals (MSR) in various regions of magnetic coordinate space. Though the coefficients of the model were estimated from 925 sampled data points, the evaluation of quality of fit was based on all the nearly 80,000 observations.

6.2 *Evaluation of Fit at Equator*

The points in Fig. 11 are the values of Y (square root of observed counting rate) plotted against L for all data points for which x is near 0, specifically $x < 0.037$ (i.e., $\lambda < 1°$). For a given L, $y'(x, L)$ changes very little between $x = 0$ and $x = 0.037$ (see Figs. 4 and 5) and the points in Fig. 11 may be regarded as approximate equatorial points. The curve in Fig. 11 gives the fitted values of $A'(L) = y'(0, L)$ using the CB coefficients, and appears to represent the data very well. Note that $A'(L)$ has not come from a fit to the equatorial data as such, but rather is the equatorial value of y' as predicted by the two-dimensional fit. That is, the fitted $A'(L)$ does not minimize the sums of squares of deviations for just the equatorial points, but is, rather, the optimum fit in the least squares sense to the 925-observation sample, and these observations are distributed through x,L space. The excessive scatter in the equatorial value of Y between $L = 1.35$ and $L = 1.55$ which shows in Fig. 11 will be taken up in the next section.

The values of $A'(L)$ are also plotted for reference as the dashed

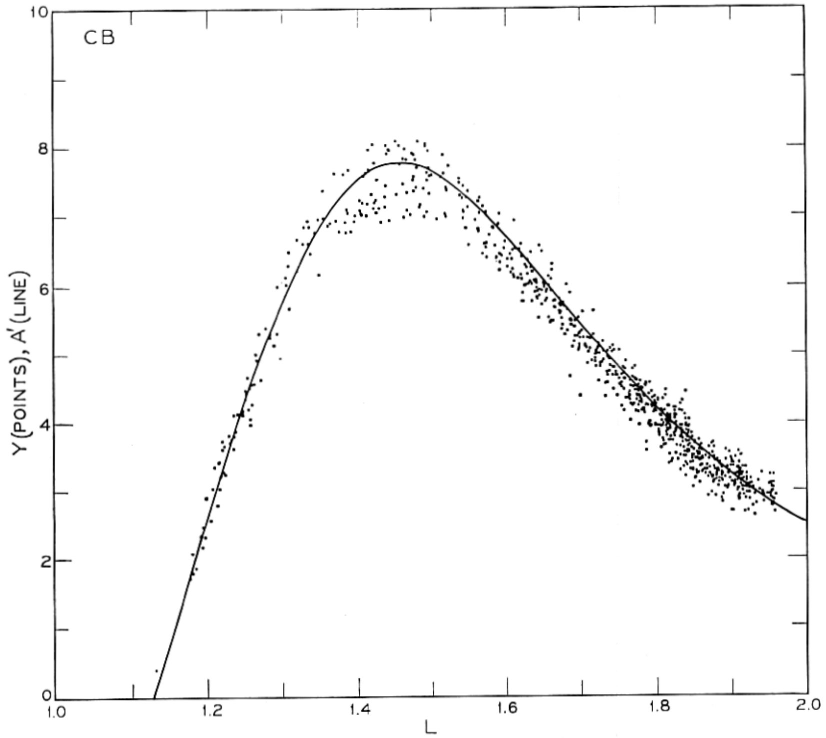

Fig. 11 — All data for $x < 0.037$ (i.e., within 1° of the magnetic invariant equator) and the equatorial value estimated from the CB coefficients plotted against L. A' and Y are in units of $(\text{counts/sec})^{1/2}$.

line in Fig. 8. One sees that the L-slices give quite good estimates for A, although these estimates tend to be a little erratic and to favor the lower values rather too much in the neighborhood of $L = 1.4$.

6.3 *Evaluation of Fit at Cutoff*

The cutoff may be thought of as the position of the outer envelope of the nonzero counting rate, or the inner envelope of the zero counting rate. Thus, in practice the location of the cutoff is associated with the sensitivity of the detector, rather than with the absence of particles. For $L \geqq 2$, there is a wide range of x over which there are many instances of either zero or one count occurring during the 11-second counting interval, and as a result the cutoff is not well-defined. This is exemplified in Fig. 6. The overlapping of the region in which no count is observed with that in which one count is observed shows clearly in Fig. 12. The locations of occurrences of zero counts are plotted in R,λ coordinates in Fig. 12(b) and in x,L coordinates in Fig. 12(d). Figs. 12(a) and (c) show the locations at which one count (one, two, and three counts for $L < 1.5$) was recorded. (The density of points has been reduced at high L to improve the clarity of the display.)

Because the cutoff is increasingly difficult to define from the data as L increases beyond ≈ 2, the position of the cutoff predicted by the fitted model is not a good boundary condition to use in judging the quality of the two-dimensional fit. Instead the locus of positions for which exactly one count per counting interval is predicted is superimposed as the solid lines in Figs. 12(a) and (c) upon the array of points giving the band of positions at which one count per counting interval was observed. The data are represented quite satisfactorily by the solid lines particularly in the region ($L \leqq 1.90$) where the belt ends abruptly. The fit is least satisfactory near $L = 2$ ($\lambda = 40°$). Adding the terms $r_4(L - L_0)^4$ and $r_5(L - L_0)^5$ to the expansion for $R_e(L)$ in (5) does not appreciably improve the fit near $\lambda = 40°$.

The line $x_c(L)$, representing the cutoff itself, is plotted as the dashed line in Fig. 12 and is seen to be a reasonable outer envelope for the nonzero counts.

The present estimate of $x_c(L)$ is also shown as the dashed line in Fig. 9. Below $L \approx 1.8$, the estimates of x_c from the individual L-slices are in good agreement with estimates from the two-dimensional fit. However, above $L \approx 1.8$ the L-slices give erratic values for x_c. As demonstrated in Fig. 7, the L-slice estimates may be biased toward high values, a circumstance which makes it difficult to extract a satisfactory fit for $x_c(L)$ from the estimates of x_c produced by fitting the L-slices.

6.4 *Behavior of* $S(L)$

The values of the function $S(L)$ generated by the two-dimensional fit cannot be subjected to a simple boundary comparison with the data. The function $S(L)$ is plotted as the dashed line in Fig. 10 along with the L-slice estimates. It will be seen that the L-slice estimates tend to be somewhat higher than the values given by $S(L)$ in the neighborhoods of $L = 1.3$ and $L = 1.9$. However, if the form of $S(L)$ is taken to provide a better fit to the points in Fig. 10, then the resulting two-dimensional fit yields a physically less satisfactory fit of the cutoff function $x_c(L)$ to the boundary data without substantial improve-

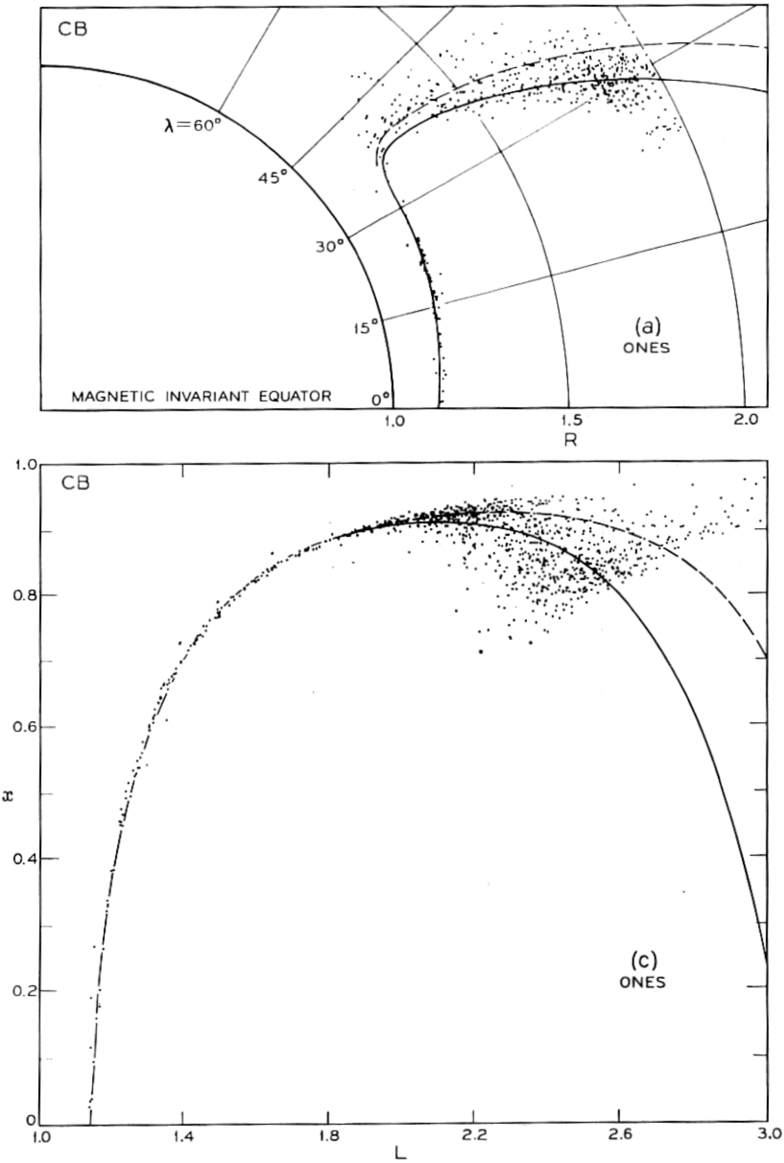

Fig. 12 — All positions in R, λ space (a) and x, L space (c) at which one count (one, two, and three counts for $L < 1.5$) was observed in an 11-second counting interval, and all positions in R, λ (b) and x, L space (d) at which zero counts were observed in an 11-second counting interval. The solid lines are the loci of positions at which the CB coefficients estimate one count in 11 seconds. The dashed lines are the loci of the cutoff function $x_c(L)$ or $R_c(L)$ calculated from the CB coefficients. The trace $R = 2.0\ R_e$, which explains the absence of data

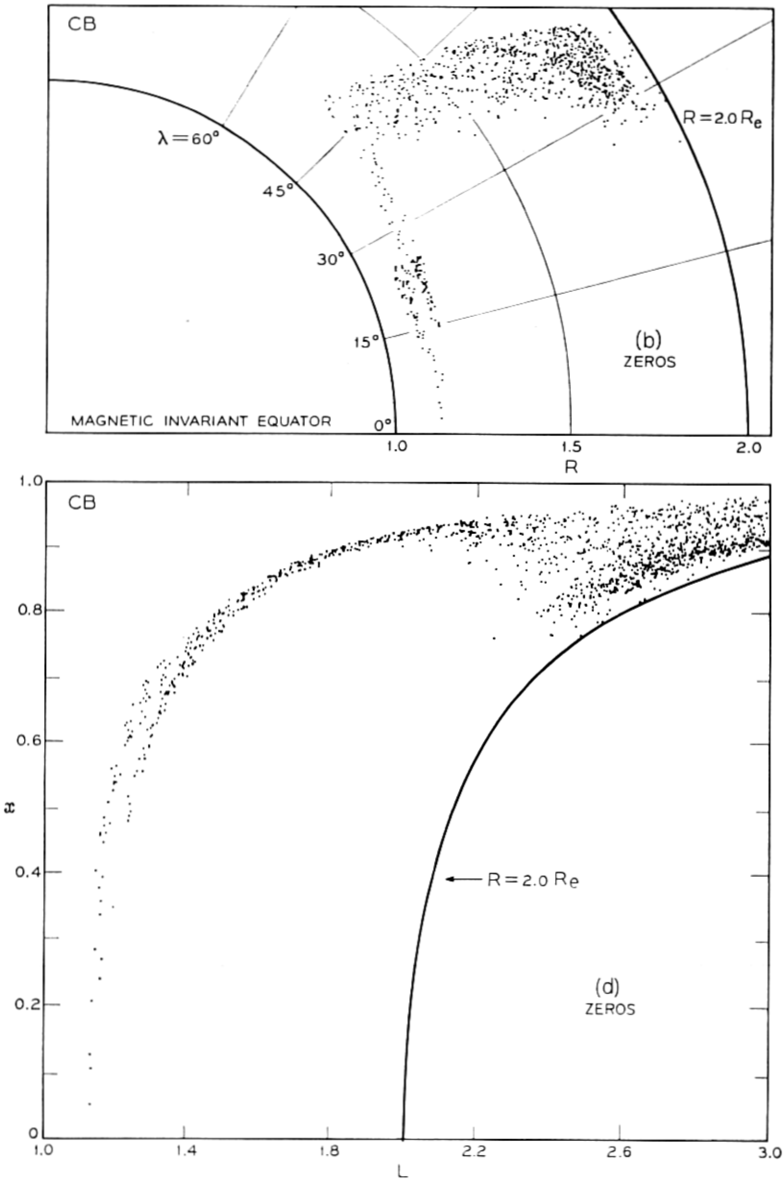

Fig. 12 — (continued)

in the lower right-hand corner of the x,L plots, appears in part (d). The cluster of points near $R = 1.1$ and $\lambda = 20°$ in part (b) of the figure is data acquired by the telemetry station at Woomera, Australia. It represents observations made near perigee when the satellite was below the bottom edge of the proton belt, which is high over the western Pacific Ocean.

ment in the overall fit (see also Section 4.7). Admittedly, this judgment is subjective because it is made in regard to regions where the cutoff is poorly defined by the data because of the insufficent sensitivity of the detector. The high values of S near $L = 1.9$ appear to arise from the correlation problem discussed in Section V in connection with Fig. 6 and Table II.

6.5 *Behavior of the Fit on Several L Slices*

The dashed lines in Figs. 4 to 7 are the values predicted by the CB coefficients superimposed on the L-slice data along with the previously derived L-slice fit. In Figs. 4 and 5, the difference between the thin solid and the dashed lines is insignificant, and this is generally the case for $L < 1.95$. At $L_m = 1.79$, the predictions from the CB coefficients differ importantly from the fit to the L-slice only for x values at which there are no data.

For $L_m = 2.2$, however, the two predictions are noticeably different as may be seen in Fig. 6. The fit to the L-slice gives the estimate $x_c = 0.954$ (see Table II); the two-dimensional fit yields $x_c = 0.928$; and the difference exceeds two standard deviations. The question as to which of the two lines is a better representation of the data in this L-slice in the physical sense, rather than in the least squares sense applied to these points by themselves, is connected with criteria which will be discussed in the following sections. The basic fact is that the two-dimensional fit provides a mechanism by which the data on every L-slice can influence the fit on every other L-slice and thereby provides a fit that is more satisfactory overall than the collection of individual L-slice fits.

6.6 *Residuals in x,L Space*

The data were also examined for dependencies on x and L over and above those provided for by the fitted mathematical model. This is accomplished by studying the residuals, i.e., $(Y - y)$, for all the nearly 80,000 observations. The residuals provide a very sensitive basis for judging the quality of the fit. The removal of the principal dependence on x and L by subtracting the fitted function from the observations has the effect of allowing small systematic differences to be prominently displayed.

Fig. 13 shows a 3100-point sample of the residuals, $Y - y$, plotted against L, where, to keep the density of the points reasonable, only one point has been plotted from each of the nearly 3100 contiguous

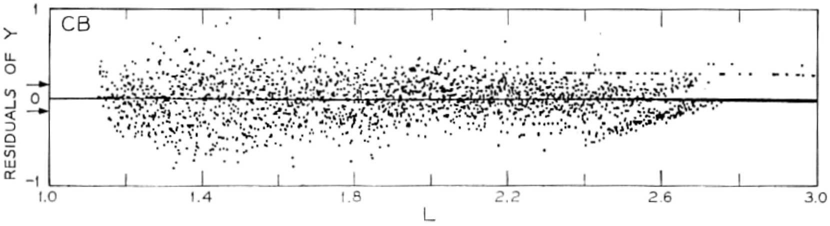

Fig. 13—CB residuals of Y (i.e., $Y - y$ calculated from the CB coefficients) plotted against L. The arrows indicate ± the approximate standard deviation if Y^2 were Poisson distributed. No more than one point is plotted for an L increment of 0.0006.

L-intervals, of width $\Delta L = 0.0006$, between $L = 1.15$ and $L = 3$. Ideally, the residuals should scatter randomly about 0, without any perceivable pattern. For $L < 2.4$ there is only a little indication of a nonrandom trend. However, for $L > 2.4$ there is a distinct pattern. This pattern is associated with the quantization error, which becomes important where the number of counts per counting interval is very small. When $0 < y < \sqrt{1 \text{ count}/11 \text{ sec}}$ and $Y = 0$ or $\sqrt{1 \text{ count}/11 \text{ sec}}$, the result is the tailing upward toward the residual = 0 axis that starts at $L \approx 2.4$. When $y = 0$ and $Y = 0$ or $\sqrt{1 \text{ count}/11 \text{ sec}}$, one gets the two-line pattern (0 and $0.0310 = \sqrt{1/11}$) seen clearly in Fig. 13 for $L \gtrsim 2.7$. (The thickening of the zero axis indicates the presence of data points.)

Fig. 14 is a plot of the residuals against x for all points for which $1.4 < L < 1.6$. The residuals in Fig. 14 show no structure; however, their average value is a little less than zero. This dip is confirmed by the points in the range $1.4 < L < 1.6$ in Fig. 13, and means that the value of y is slightly high relative to the data in this region. However, the lack of structure in Fig. 14 indicates that the bias is independent of x in this region.

Fig. 15, the plot of the residuals vs x for $1.85 < L < 1.90$, shows the region in which the fit is poorest. The residual points are not symmetrically distributed about zero and the asymmetry seems to depend on x. Notice that the value of y is slightly too large near $x \approx 0.05$ and $x \approx 0.65$. The discussion of these trends is continued below, after some further analysis has been described.

6.7 *Mean Square Residuals in x,L Space*

Another way of gauging the quality of fit is to compute the mean square of the residuals (MSR) separately for various regions of x,L space. Trends in these quantities may indicate regional varia-

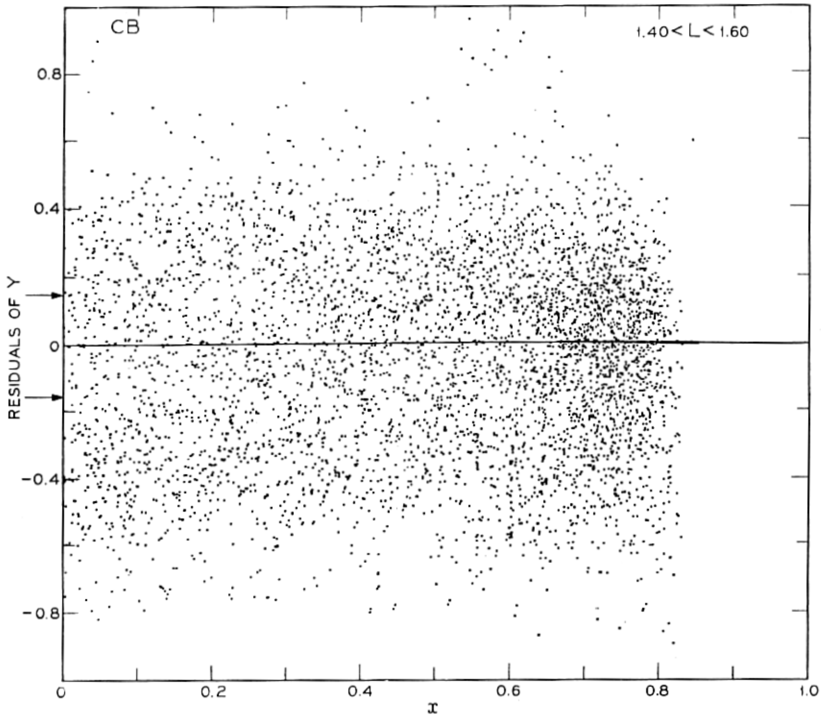

Fig. 14 — CB residuals of Y (i.e., $Y - y$ calculated from the CB coefficients) plotted against x for $1.40 < L < 1.60$. The arrows indicate ± the approximate standard deviation if Y^2 were Poisson distributed.

tions in the adequacy of fit. The data and residuals were divided into three groups. Group I contains all the "good" data points "within" the boundaries of the $>$ 50 MeV proton belt. These points are defined as those not included in Groups II and III. Group II consists of the "good" data points "outside" the boundaries of the belt. These are points which meet two criteria: they have values of (x, L) for which x is greater than $x_c(L) + 0.001$, and they are not in Group III. Group III comprises the outliers or "bad" data points, defined as those points whose residuals are greater than three times the overall root mean square residual of the points in all *three* groups together.* The most probable origin of a point in Group III is a telemetry error.

If the number of counts in a counting interval behaves like a

---

* Note that only 0.5 percent of the data fall in Group III.

Poisson random variable, then the variance of Y^2 would be equal to the average value of Y^2. As noted in Appendix B, when Y is not near zero, the variance of Y would then approximately equal 0.023, independent of the average value of Y. This value then might approximately represent the average value of the mean square residual, MSR, on the scale of Y. Thus, the number 0.023 provides a baseline for the comparisons discussed below.

Table III lists the mean square residuals (MSR) by L range and by Group. For Group II, Y is frequently zero and, as $x > x_c$ implies $y \equiv 0$, one finds that the residual is zero very often. Of course, under the Poisson assumption the variance of Y when its average value is 0 or very close to 0 will be less than 0.023 (see Appendix B.2) and the appearance of MSR values smaller than 0.023 in Group II is thus not surprising. A similar circumstance exists in Group I for $L > 2.6$.

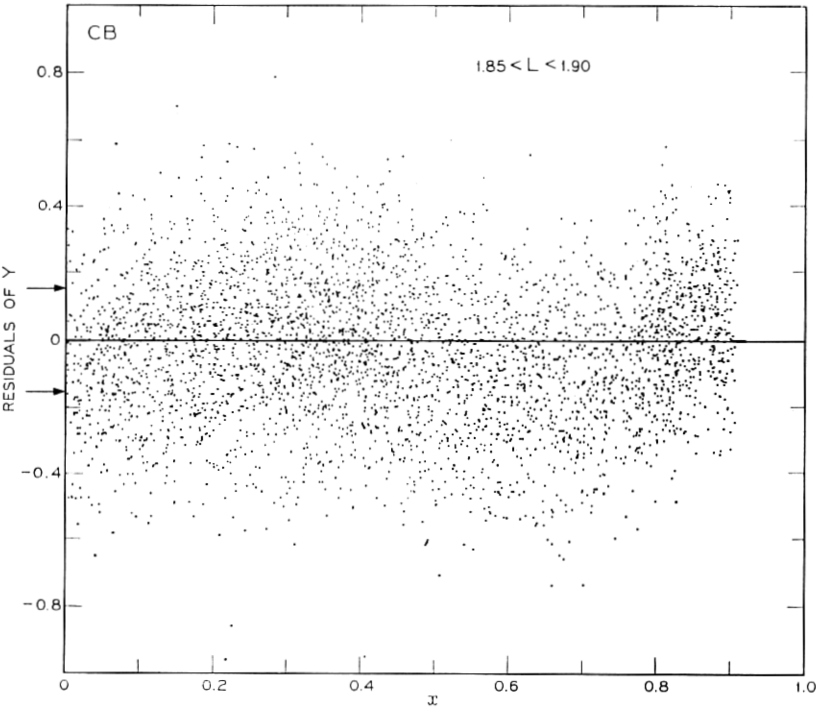

Fig. 15—CB residuals of Y (i.e., $Y - y$ calculated from the CB coefficients) plotted against x for $1.85 < L < 1.90$. The arrows indicate ± the approximate standard deviation if Y^2 were Poisson distributed.

TABLE III—MEAN SQUARE RESIDUALS AND MEAN SQUARE ERRORS.

L-Range		All data. CB coefficients					
		Group I		Group II		Group III	
L_{MIN}	L_{MAX}	No. of points	MSR	No. of points	MSR	No. of points	MSR
1.1	1.2	148	0.039	31	0.009	0	0.
1.2	1.3	1147	0.053	68	0.019	9	4.171
1.3	1.4	1608	0.106	99	0.027	20	2.265
1.4	1.5	1939	0.106	120	0.010	19	6.743
1.5	1.6	2974	0.083	101	0.004	22	9.079
1.6	1.7	3835	0.056	104	0.004	26	4.617
1.7	1.8	5233	0.055	87	0.001	29	4.356
1.8	1.9	8487	0.054	92	0.001	54	4.110
1.9	2.0	8880	0.041	98	0.011	55	4.280
2.0	2.1	6261	0.043	106	0.033	24	8.031
2.1	2.2	5354	0.032	183	0.049	18	6.509
2.2	2.3	4717	0.030	313	0.047	16	6.982
2.3	2.4	4040	0.034	477	0.030	21	9.478
2.4	2.5	3769	0.044	716	0.021	22	8.296
2.5	2.6	2987	0.038	1000	0 014	15	6.462
2.6	2.7	2066	0.023	1696	0.010	15	17.098
2.7	2.8	225	0.011	3104	0.007	24	13.343
2.8	2.9	0	0.0	2784	0.006	11	14.545
2.9	3.0	0	0.0	2394	0.005	6	15.908
1.1	3.0	63670	0.048	13573	0.011	406	7.011
1.1	3.0	925	0.045	MSE of CB Sample (Group I + Group II)			
1.1	2.0	975	0.065	MSR of equatorial points, λ < 1° (Group I)			

L-Range		HTB data. Model I coefficients (see Table IV)					
		Group I		Group II		Group III	
L_{MIN}	L_{MAX}	No. of points	MSR	No. points of	MSR	No. of points	MSR
1.1	1.2	111	0.037	28	0.010	0	0.
1.2	1.3	650	0.045	49	0.028	8	4.435
1.3	1.4	633	0.059	78	0.043	6	1.253
1.4	1.5	693	0.050	56	0.0	7	5.892
1.5	1.6	926	0.039	43	0.019	1	0.816
1.6	1.7	1342	0.036	38	0.002	6	5.472
1.7	1.8	2161	0.037	39	0.005	8	5.474
1.8	1.9	4708	0.037	30	0.003	38	4.981
1.9	2.0	5585	0.046	28	0.013	40	4.184
2.0	2.1	3728	0.049	38	0.021	16	9.037
2.1	2.2	3258	0.033	38	0.036	10	9.716
2.2	2.3	2857	0.030	80	0.034	10	6.581
2.3	2.4	2335	0.032	135	0.027	14	9.094
2.4	2.5	2193	0.043	212	0.020	11	8.922
2.5	2.6	1831	0.041	278	0.011	11	6.638
2.6	2.7	1520	0.027	464	0.007	9	17.120
2.7	2.8	1083	0.014	765	0.007	18	15.845
2.8	2.9	146	0.009	1433	0.007	9	16.145
2.9	3.0	0	0.0	1317	0.005	4	20.590
1.1	3.0	35760	0.038	5149	0.009	226	7.926
1.1	3.0	960	0.036	MSE of 960-point HTB Sample (Group I + Group II)			
1.1	2.0	429	0.035	MSR of equatorial points, $\lambda < 1°$ (Group I)			

Poisson approximation: variance ≈ 0.023. Note conditions in text and Appendix B.2.

For the overall fit, the MSR of Group I (L range from 1.1 to 3.0) is only twice 0.023. However, for $1.3 < L < 1.6$ the Group-I MSR is four times 0.023. This L range is associated with the large scatter in the equatorial data plotted in Fig. 11, and Fig. 14 shows that this scatter is independent of x, rather than just an equatorial phenomenon. This issue is pursued further below.

6.8 *Dependence of Residuals on Other Variables*

Studies were made of the possible dependence of the residuals on observed variables other than x and L. Indeed, it will appear that some of the excess scatter exhibited in Table III and in Figs. 11 and 14 is associated with instrumental effects.

The regularities inherent in the orbit and orientation of a satellite, the motion of the earth, and the location and operation of the telemetry receiving stations lead to systematic interrelations among the various coordinates listed in Table I. A simple example concerns temperature. The satellite cools when its enters the earth's shadow. This eclipse occurs only on the night side of the earth. Thus, if the detector is temperature sensitive, one would see a false day-night effect in the counting rate. If, because of additional dependencies, data are available during eclipse for only a limited span of days, a false secular effect might also be observed. Because of the implications of the preceding discussion, a careful study was made of the behavior of the residuals with respect to a large number of coordinates, and attention was given to the details of the relationships among the coordinates during the search for contributors to the inflation of the MSR.

We present below the evidence that has led us to the conclusion that two instrumental effects, variations in bias voltage and changes in temperature of the detector, are principal causes of inflation of the MSR.

There was no temperature sensor on the particle detector. The instrument is not exposed to sunlight and is relatively well-insulated thermally from the skin and frame of the satellite. Consequently, temperature measurements of the skin are not closely related to the temperature of the detector. However, a good indicator of detector temperature is elapsed time since entering or since leaving eclipse. Fig. 16 gives plots of the residuals, $Y - y$, against time in minutes measured from the more recent of the two events, entered shadow or entered sunlight. Residuals associated with periods during which the satellite did not enter eclipse once per orbit are segregated at the far right-hand side of the plots, labeled A on the abscissa.

Figs. 16(a) and (b) are for $1.4 < L < 1.6$. The points in Fig. 16(a) are those for which the bias voltage was between 95.3 and 97.5 volts, while Fig. 16(b) contains those for bias voltages between 92.0 and 95.3 volts. The decrease in the residuals (and also in the observed counting rate) after the satellite enters eclipse (and the temperature falls) and the increase after the satellite leaves eclipse (and the temperature rises) may be seen distinctly in both figures. In addition the residuals are noticeably more negative for the low (92.0 to 95.3 V) bias range. Both low bias voltage and low temperature are known to decrease the efficiency of the detector and one expects an appreciable effect to be introduced into the counting-rate data. In the present case the scatter is about ±15 percent of the counting rate. A consequence of this is the excess scatter that has been noted particularly with reference to Fig. 11 and Table III.

Figs. 16(c) and (d) are analogous to Figs. 16(a) and (b), but the residuals are for the L range 1.85 to 1.90. Again, the systematic influence of low temperatures and low bias voltages is unmistakable.

6.9 *Partitioning the Data*

Two ways of responding to these instrumental effects might be: (*i*) to try to correct the data, or (*ii*) to disregard the affected data. It is not possible to make a correction to the counting rate that is properly independent of the experimental results because; (*i*) the bias voltage was measured in steps of 1.11 V, which is not sufficiently fine-grained; (*ii*) it would be necessary to estimate the temperature of the instrument using a complicated hypothetical relationship between the instrumental temperature, skin temperature, and time after entering eclipse (or sunlight); and (*iii*) we have an insufficient knowledge of the temperature and bias-voltage sensitivity of the detector.

Though an ad hoc correction based on the observed counting rates could have been attempted, it was decided for practical reasons to eliminate both the low-temperature and low-bias points and use only that data which was gathered under the following conditions:

(*i*) The satellite had been in sunlight for the previous 50 minutes, and thus had attained temperature equilibrium reasonably well (see Fig. 16).
(*ii*) The bias voltage was between 95.3 and 97.5 volts.

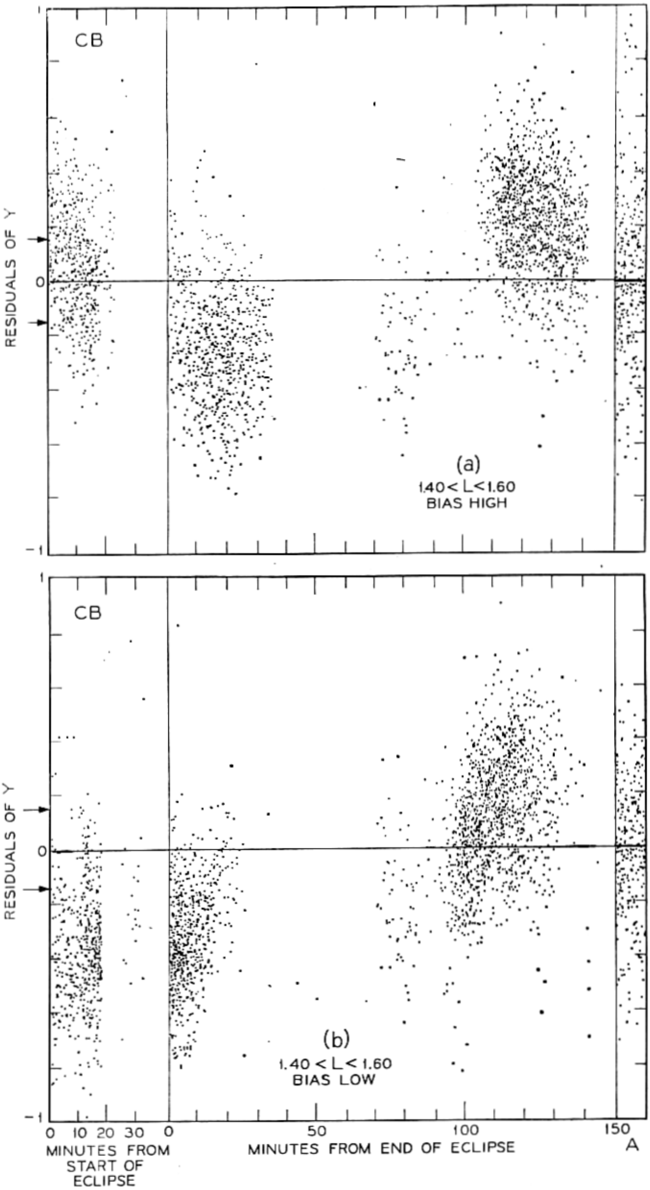

Fig. 16 — CB residuals of Y (i.e., $Y - y$ calculated from the CB coefficients) plotted against time in minutes from the most recent of the two events, entered eclipse or entered sunlight. Data taken on days during which no eclipse occurred are plotted

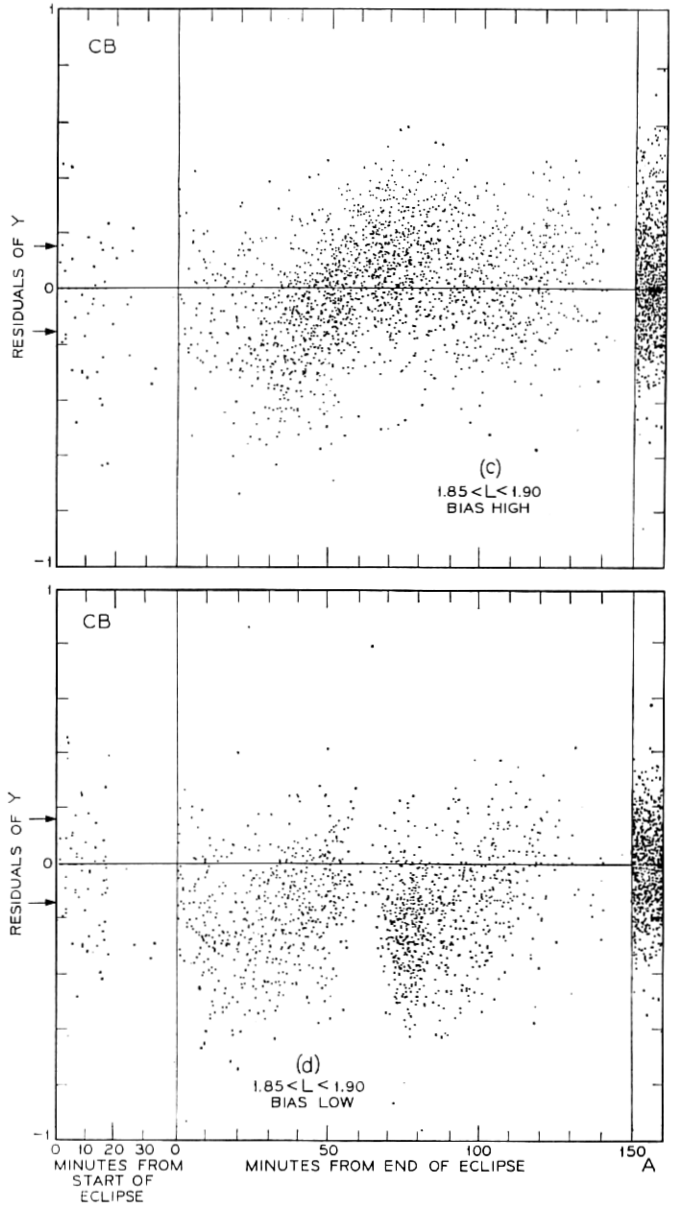

Fig. 16 — (continued)
within the region marked "*A*" at arbitrary values of the abscissa. The arrows indicate ± the approximate standard deviation if Y^2 were Poisson distributed.

This selection yields a homogeneous body of 41,135 points, henceforth referred to as high temperature-high bias (HTB) observations. The remaining 36,500 points, which represent a mixture of temperature and bias conditions, were used only occasionally in further analyses. This selection process coincidentally produces one unfortunate associated circumstance, namely, the exclusion, as low-bias data, of all measurements made between days 325 and 373.

Further analysis and model fitting and development based on, and directed towards, this HTB data is detailed in the following sections and Appendix C.

VII. THE TWO-DIMENSIONAL FIT FOR THE SELECTED (HTB) DATA

7.1 *Sample Selection*

The distribution of the HTB data in magnetic space is indicated in Fig. 17, which gives the R,λ coordinates of every tenth point from the 41,135 L-ordered HTB observations. The data provide reasonably adequate, though uneven, coverage. As a practical requirement for the fitting procedure, a "representative" sample of about 1000 observations must be selected.

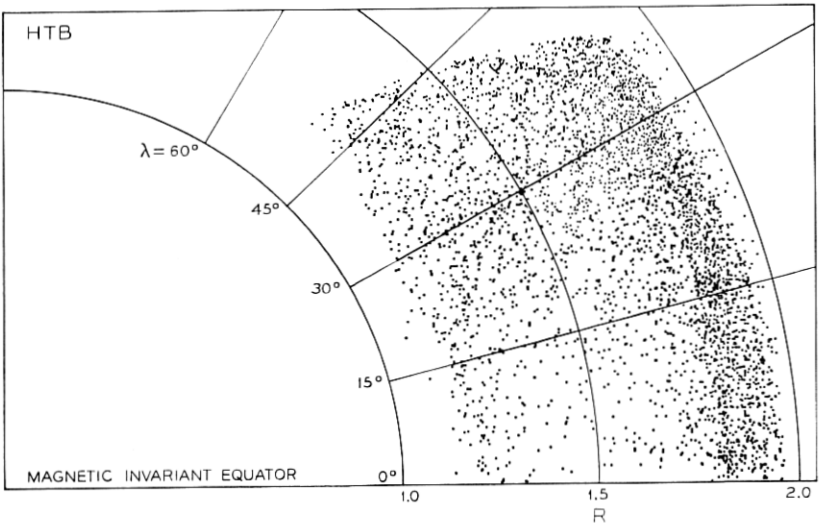

Fig. 17 — The spatial distribution of the HTB data for $L < 3$ in R, λ coordinates. Every tenth point from the L-ordered data is plotted.

It is intuitively clear from preliminary knowledge of the radiation distribution that some sample configurations will be far more effective than others in defining the functional form of the proton flux.

The sample selection is important because: (*i*) nothing more than a sophisticated smoothing function is being fitted and we want this function to be broadly applicable over the entire space; (*ii*) an optimum fit in one region of space does not necessarily imply a good fit elsewhere; (*iii*) the spatial distribution of data points depends on the satellite orbit and the position of the telemetry stations; (*iv*) even with the square root transformation, there remains some differential variance among the data.

These considerations argue against using a simple random sample or even a random sample in x with a systematic sample in L such as in the CB fit. Indeed, they also argue against fitting *all* (unweighted) HTB data, even if this were practical. Alternatively, points might be chosen on the basis of a simple geometric grid in magnetic space. Such a procedure would be easy to use, but it is arbitrary with respect to the radiation belts.

Sampling procedures might be based on particular physical features of the radiation belts to emphasize the goodness of fit, for example, where the flux is high or where diffusion across L lines might be important. However, such fits would be too biased for our present general objective.

One is thus led to a sampling process based on properties of the radiation belt itself, as described for example by the preliminary CB fit. In particular, a high density of data points is desirable in regions where the value of y is changing rapidly, while a low density will suffice where the function is changing slowly. A realization of this criterion would be to define about 1000 x,L cells, within each of which the range of y from the preliminary fit would be the same. However, there are appreciable practical difficulties in defining the boundaries of such cells.

Thus, the following hybrid procedure was used to define the 960-point HTB sample on which the subsequent fitting was done: The L-range from 1 to 3 was divided into about 120 L-slices of equal ($\approx$ 0.017) width in L. Each L-slice was then divided into eleven x,L cells using a scheme that depends on the preliminary fit. The first ten cells were chosen so that within each cell the range of y predicted by the CB model is closely 1/10 of the equatorial value of y at the center of the L-slice. The eleventh cell lies beyond x_c. The *method* of partitioning in the x direction is illustrated by the partition of the L-slice in Fig. 5(a) into five x-regions by the horizontal lines. (The distance d is added to x_c to define the lower-x boundary of the last cell.)

To take some account of differential variances remaining after the square root transformation, the following procedure was employed: The mean square deviation from the mean (MSD*) was calculated for all the HTB data in each x,L cell defined above; thence, after visual inspection of the results (see Appendix C), three groupings of contiguous x,L cells were made according to whether the MSD's were generally below 0.013, between 0.013 and 0.020, or above 0.020; the corresponding regions were then given relative weights of 2, $1\frac{1}{2}$, and 1, respectively. The weight 1 implies that one point was sampled from the cell.

These weights were assigned on the basis of a judgment which considered: (*i*) the desire to increase the weight of low variance (i.e., near-zero counting rate) observations and thus to aid the definition of the cutoff; and (*ii*) the desire to keep from "wasting" sample points in the region $x \gg x_c$ since such data will add little to the specification of $x_c(L)$ and virtually nothing to the estimation of $A(L)$ and S.

Fig. 18 shows the distribution in x,L space of the 960-point sample which was used. The number 960 came about because a number of the defined cells had no data in them. Our experience with several other samples of the HTB data gives us confidence in both the rationale behind, and the results obtained with, this 960-point set, henceforth referred to as the HTB sample. However, sampling procedures tailored to the requirements of special purpose fits will give better results in some regions of x,L space.

Some additional discussions relevant to sample selection and data usage are given in Section 13.3 and Appendices B.3 and C.2.

7.2 *The HTB Fit*

A slightly constrained version of Model I of Section 4.4 was fitted to the 960-point HTB sample. The results are referred to as the HTB fit. The constraint is $s_1 = 0$, in (3). Most of the values of s_1 obtained in preliminary fits to various samples of the HTB data differed from zero by less than two standard deviations. Also, the points in Fig.

---

* See Table I for definition of MSD, MSR and MSE.

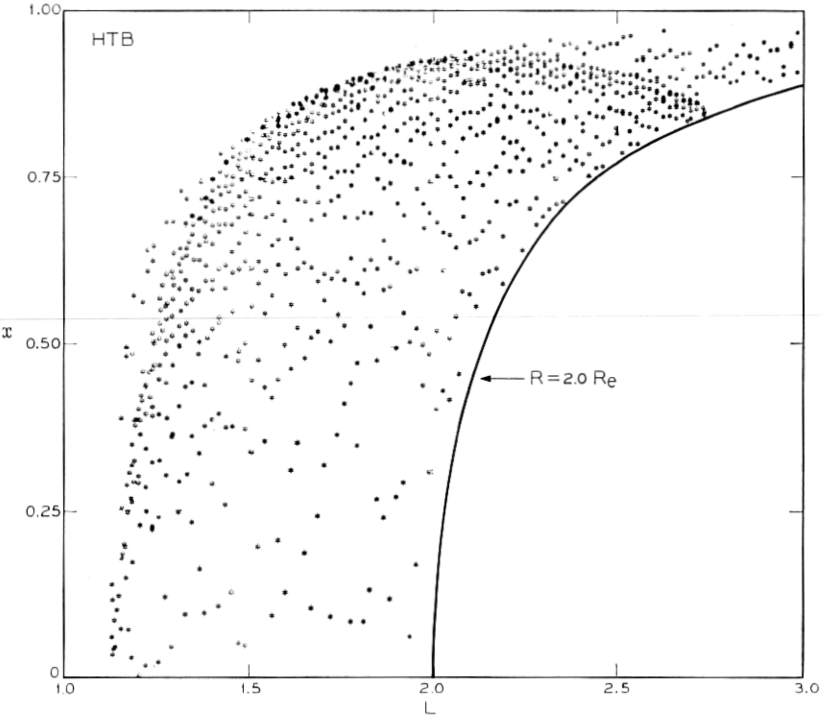

Fig. 18 — The distribution of the 960-point HTB sample in x, L space. The trace $R = 2.0\ R_e$ explains the absence of data in the lower right-hand corner of the figure.

10 do not suggest a linear dependence of S on L.* The effect of this constraint on the value of the fitted cutoff function was examined and found to be unimportant.

The estimated HTB coefficients (obtained by fitting the constrained model to the HTB sample) appear in Table IV. The physical interpretation of L_0 as the lowest L on which > 50 MeV protons were measurable was noted in Section 4.3. The standard error of 0.001 (≈ 6 km in altitude) is no larger than the uncertainties inherent in the calculation of L itself.

The interpretation of S as a shape factor (see Section 4.2) is straightforward in the present case, i.e., where $s_1 = 0$. The standard error of 0.005 is much smaller than the standard errors of the estimates of S generated from the fits to L-slices (Table II) and is

---

* Some higher-order models for $S(L)$ were tried but proved unsatisfactory (see also Sections 6.4 and 9.2).

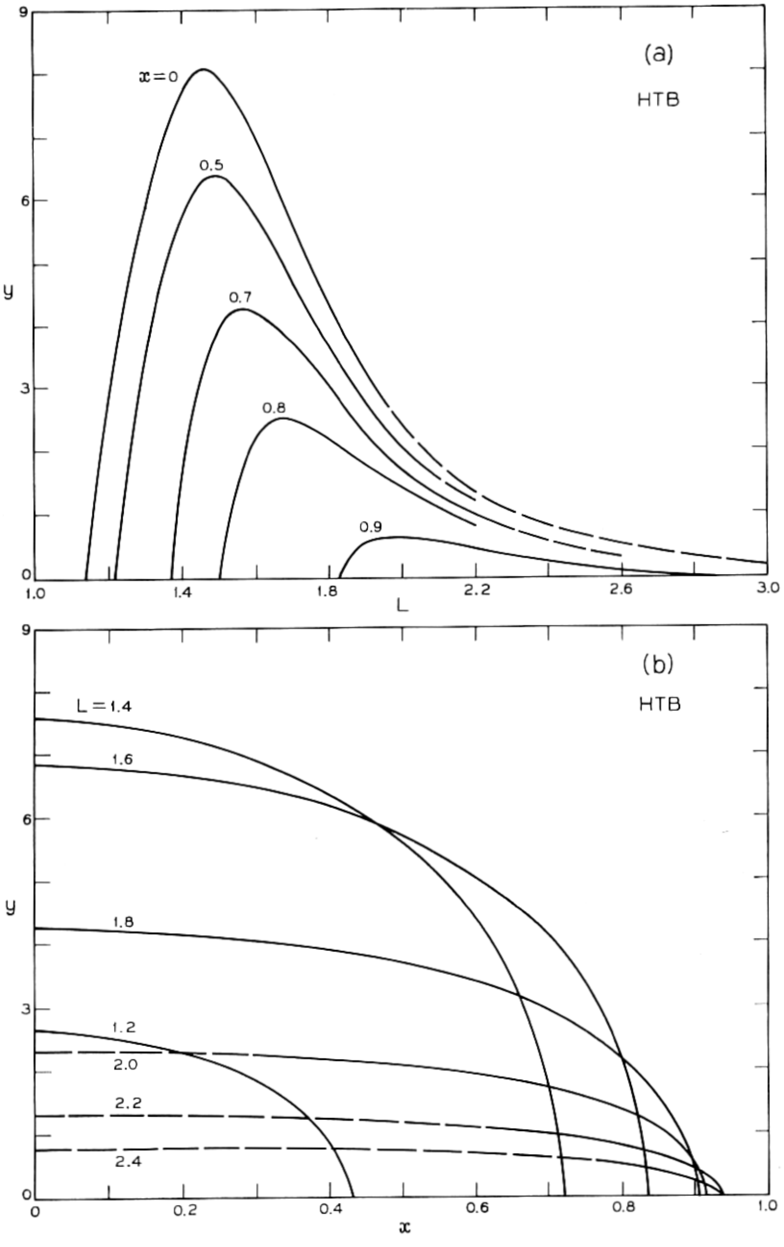

Fig. 19 — Graphical summary of the HTB fit, (a) curves of y' vs L for constant x, (b) curves of y' vs x for constant L, (c) contours of constant y' in x,L space.

also small compared to the scatter in Fig. 10. This implies that a substantial fraction of the scatter may be associated with the high correlation between S and x_c on the L-slice fits. Further consideration of standard errors and correlations of the fitted coefficients and detailed statistical evaluation of the fit is deferred to Section VIII.

Fig. 19 presents a graphical summary of the function $y'(x, L)$. Part (a) of the figure shows y' vs L for (several) constant x. Physically, these curves correspond to values of the intensity of radiation vs L for constant magnetic dipole latitude, because x = constant implies λ = constant. The nesting of the curves in Fig. 19(a) is a consequence of the fact that $G'(x;\ x_c,\ S)$ decreases monotonically with x [see (2) and Fig. 19(b)]. The shape of the curves changes smoothly with L, and the position of the maximum shifts smoothly toward higher L as the value of x (and therefore λ) increases.

The nesting property does not hold for plots of y' vs x at constant L. This general consequence of the existence of a maximum in $A'(L)$ is displayed in Fig. 19(b). All the curves in Fig. 19(b) have similar dependences on x.

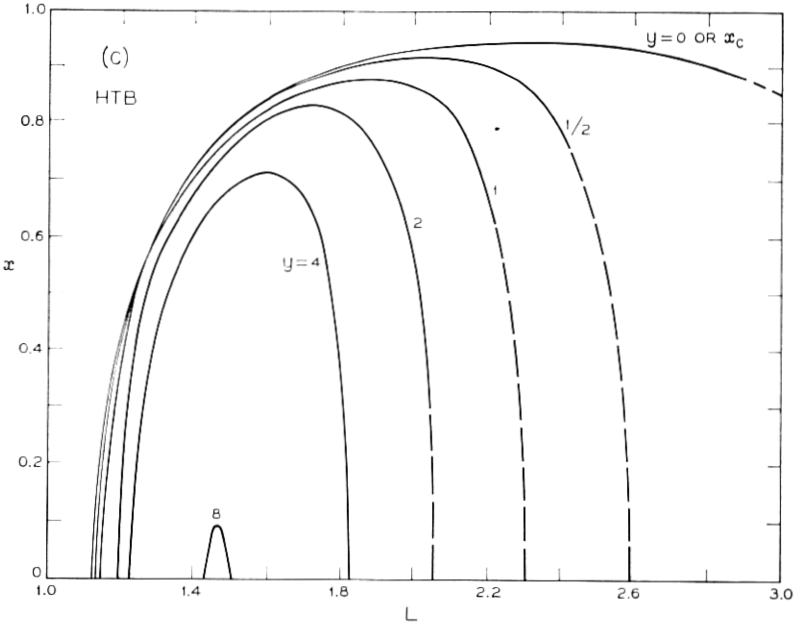

Fig. 19 — (continued)

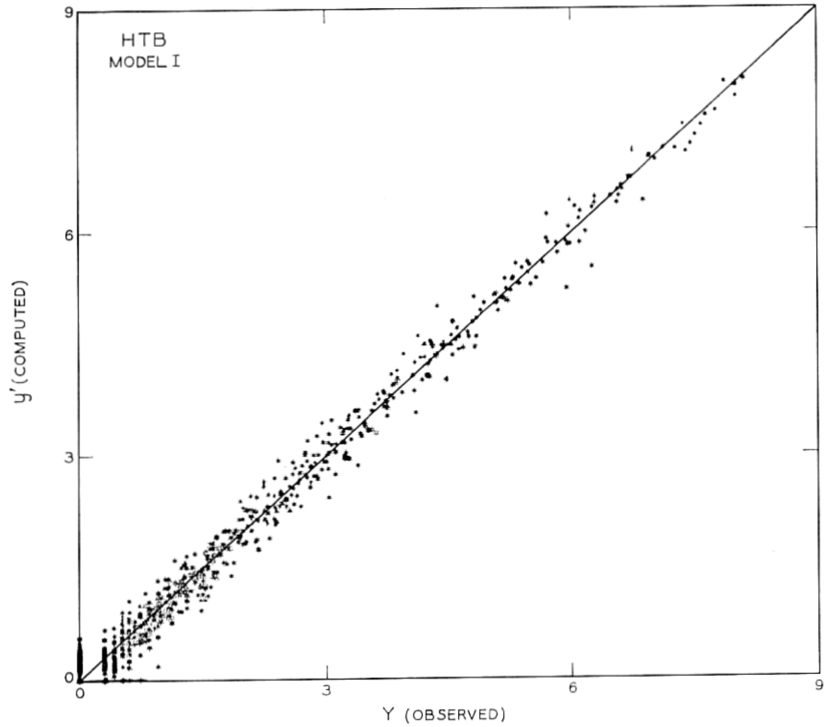

Fig. 20 — The value of y' computed from the HTB coefficients of Model I vs the observed value, Y, for the 960-point HTB sample.

Fig. 19(c) contains contours of constant y' plotted in x,L space and completes the graphical summary. The contours surround the point $x = 0$, $L = 1.46$ at which the peak intensity occurs.

7.3 *Evaluation of Fit to the HTB Sample*

A summary indication of the quality of the fit of the 9-coefficient Model I to the HTB sample is given in Fig. 20, in which the fitted (computed) value, y', is plotted against the corresponding observed value, Y. The solid straight line would represent the case of a perfect fit. This is impossible on the basis of a model using only x,L coordinates since different Y values were observed for the same x,L pairs. It is seen, however, that the scatter of the plotted points about the line of perfect fit is reasonably uniform and that the horizontal width of the "scatterband" is roughly constant over the entire range of y'.

In the following subsections, the quality of fit to the entire body of HTB data is scrutinized, using many of the procedures used in the previous section to evaluate the CB fit.

7.4 *Evaluation of Fit on Equator*

The HTB fit along the equatorial boundary is displayed in Fig. 21. The points are the values of observed Y plotted against L for all HTB data for which $0 \leqq x < 0.037$ (i.e., $\lambda < 1°$), and the plotted curve is $A'(L)$, defined in (6), using the HTB coefficients of Table IV. Comparing Fig. 21 with Fig. 11, it is seen that most of the excess scatter has been eliminated. The curve in Fig. 21 does not deviate noticeably from the center line of the points (except for $1.5 < L < 1.6$, where the curve is a trifle high and for $L \approx 1.95$, where the curve is a trifle low).

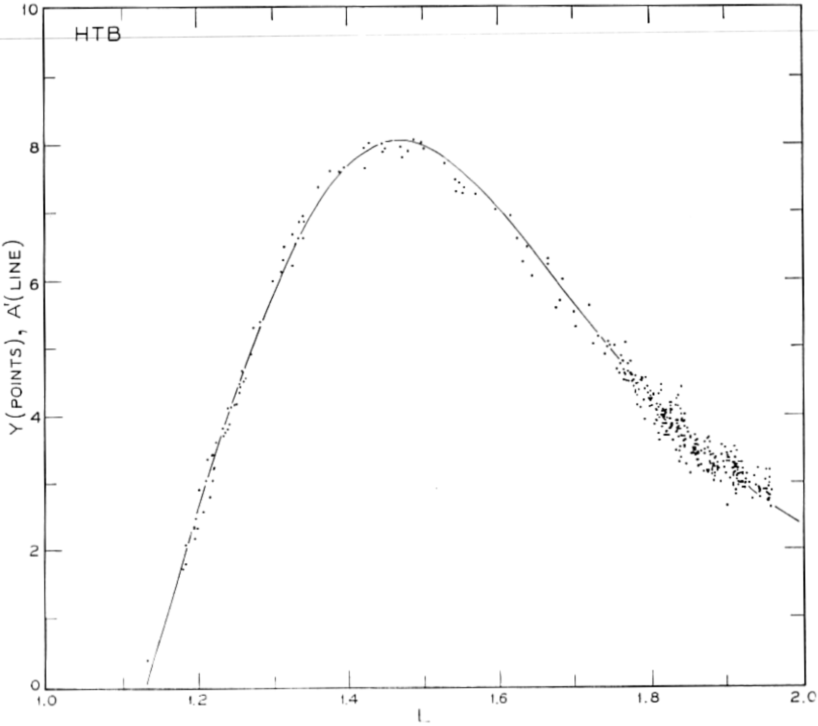

Fig. 21 — All the HTB data for $x < 0.037$ (i.e., within 1° of the magnetic invariant equator) and the equatorial value estimated from the HTB coefficients plotted against L. A' and Y are in units of $(\text{counts/sec})^{1/2}$.

TABLE IV—FIT OF MODEL I TO 960-POINT HTB SAMPLE. (HTB COEFFICIENTS.)

Analysis of variance

Due to	d.f.*	Sum of squares	Mean square
Total	960	5374.7320	
Mean	1	2121.1760	
Corrected total	959	3253.5560	
Model	9	5340.0645	593.3405
Error	951	34.66751	0.03645

Coefficient estimates

	a_1	L_0	a_2	a_3	η	r_1	r_2	r_3	S
Estimate	12.0702	1.1300	0.3006	0.7131	5.6190	0.2600	−0.4937	0.3536	0.3221
Standard error	5.1178	0.0010	0.1205	0.0765	0.3798	0.0090	0.0245	0.0190	0.0048

α values

		a_1	L_0	a_2	a_3	η	r_1	r_2	r_3	S
ρ values	a_1		0.13	0.97	−0.98	0.90	0.11	0.09	−0.08	−0.00
	L_0	0.4969		0.12	−0.13	0.11	−0.47	0.27	−0.15	−0.00
	a_2	0.9995	0.4783		−0.96	0.92	−0.10	0.09	−0.08	−0.00
	a_3	−0.9998	−0.4998	−0.9990		−0.90	0.11	−0.09	0.08	0.00
	η	0.9948	0.4705	0.9966	−0.9941		−0.10	0.10	−0.09	−0.00
	r_1	0.4624	−0.8541	−0.4505	0.4617	−0.4490		−0.64	0.43	0.00
	r_2	0.4261	0.6819	0.4199	0.4243	0.4268	−0.9378		−0.72	0.00
	r_3	−0.3951	−0.5355	−0.3926	0.3929	−0.4066	0.8219	−0.9589		−0.00
	S	−0.0571	−0.0270	−0.0616	0.0657	−0.0680	−0.1166	0.0653	−0.0587	

* degrees of freedom

In Fig. 8 the solid curve, which is $A'(L)$ calculated from the HTB coefficients, may be compared with the dashed curve, which is $A'(L)$ calculated from the CB coefficients. The HTB fit gives higher equatorial values for y' when L is less than ≈ 1.9, as might be expected from the fact, displayed in Figs. 16(a) and (b) and discussed in Section 6.8, that the HTB data select the higher values of Y for $1.4 < L < 1.6$. For L greater than ≈ 1.9, the equatorial values of the HTB fit are somewhat lower than those of the CB fit; however, there is no equatorial data for $L > 1.95$, and the comparison of the fits is not meaningful in this region. The points in Fig. 8 are estimates based on CB, *not* HTB, data and are *not* immediately pertinent to the solid curve.

An estimate of the standard error of the fitted equatorial function $A'(L)$, based on the HTB sample, is plotted as a function of L in Fig. 22(a) (see Section VIII for details). The standard error of $A'(L)$ is typically less than one percent in the range of L ($1.15 < L < 1.95$) over which equatorial data are available. Error bars of this size would hardly be visible in Fig. 21. For the same values of L, the standard errors of $A'(L)$ derived from the HTB fit are substantially smaller than those from the L-slice fits listed in Table II. As might be anticipated, the percent standard error of $A'(L)$ increases as the minimum x values of available data increases with increasing L beyond $L = 2$. This increase to a value of 10 percent at $L = 3$ reflects increasing uncertainty in the extrapolation of the fit. Note that the curves in Fig. 8, which represent the equatorial values of CB and HTB fits, differ, in general, by substantially more than two standard errors and the difference is certainly "statistically significant."

7.5 *Evaluation of Fit at Cutoff*

Figs. 23(b) and (d) show the positions, in x,L and R,λ coordinates, at which zero counts were observed during an 11-second counting interval. Figs. 23(a) and (c) are corresponding plots for one count (one, two, or three counts for $L < 1.5$) per counting interval. Only HTB data are plotted, and the density of points at high L has been reduced to improve the clarity of the display.

Judgments regarding the quality of the fit are made, once again, with reference to the well-defined band of one count, rather than in terms of the more nebulous cutoff. The solid lines in Figs. 23(a) and (c) are the loci of $y'(x, L) = \sqrt{1 \text{ count}/11 \text{ sec}}$, using the HTB coefficients

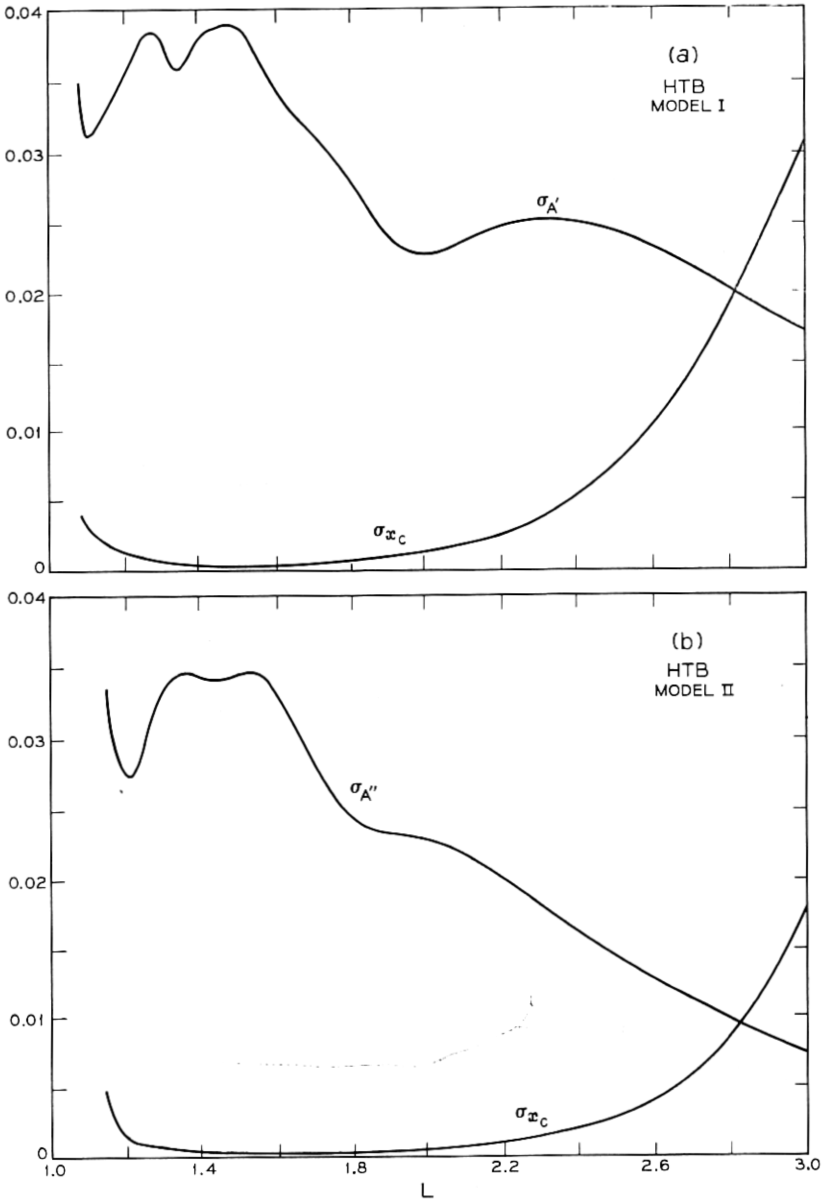

Fig. 22 — The standard deviation of A, σ_A, and the standard deviation of x_c, σ_{x_c}, as functions of L. Units of σ_A and σ_{x_c} are the same as the units of A and x_c, respectively. (a) Model I. (b) Model II.

in the model. These lines represent the data well. Although the fit appears uniformly good in the x,L representation, a slight weakness near the "corner" at $\lambda \approx 40°$ is displayed sensitively in the R,λ plot (see also Fig. 12).

The dashed lines in Figs. 23(a) and (c) show the locus of the fitted cutoff function, $x_c(L)$, calculated from the HTB coefficients. Error bars indicating excursions of one standard error in $x_c(L)$ are shown at two places on Figs. 23(a) and (c). The standard deviation of $x_c(L)$ as a function of L has been estimated (see Section VIII), and is plotted in Fig. 22(a). This standard error is smaller than those produced by the L-slice fits at corresponding values of L (see Table II).

The values of $x_c(L)$ for the HTB and CB coefficients are plotted in Fig. 9. Although there is no discernible difference between the two curves in the figure for $L < 2$, the difference between the tabulated values exceeds twice the standard error (which is very small) over much of the range of L. The two sets of coefficients thus lead to results which differ in a "statistically significant" manner. For L less than ≈ 2, the significance of the standard error is more readily understood when it is interpreted in terms of the altitude of the cutoff. This is done in Section XI.

Beyond $L \approx 2$, the values of x_c for the CB and HTB coefficients diverge noticeably, compare Figs. 12(a) and (c) with Figs. 23(a) and (c), respectively. The magnitude of this divergence is quite sensitive to the method used in selecting the samples to be fitted. As has been discussed, the concept of a cutoff is not well defined in the context of these measurements for $L > 2$. The uncertainty is reflected in the rapid rise in the value of the standard error of $x_c(L)$ [see Fig. 22(a)] as L approaches 3. The significance of this rise may be more readily appreciated by referring once more to the error bars associated with $x_c(L)$ in Figs. 23(a) and (c).

The partitioning of the data on the basis of electrical bias and temperature, and the procedure chosen for selecting the sample to the fitted, introduce statistically significant differences between the values of $x_c(L)$ obtained from the HTB and CB fits, as well as the more readily anticipated significant differences in the values of $A'(L)$.

7.6 *Standard Error of Fitted Value*

The standard error for $y'(x, L)$ is relatively constant, ranging between 0.01 and 0.04, except close to $x_c(L)$. It should be understood that this standard error is based on the fit to the HTB sample, and

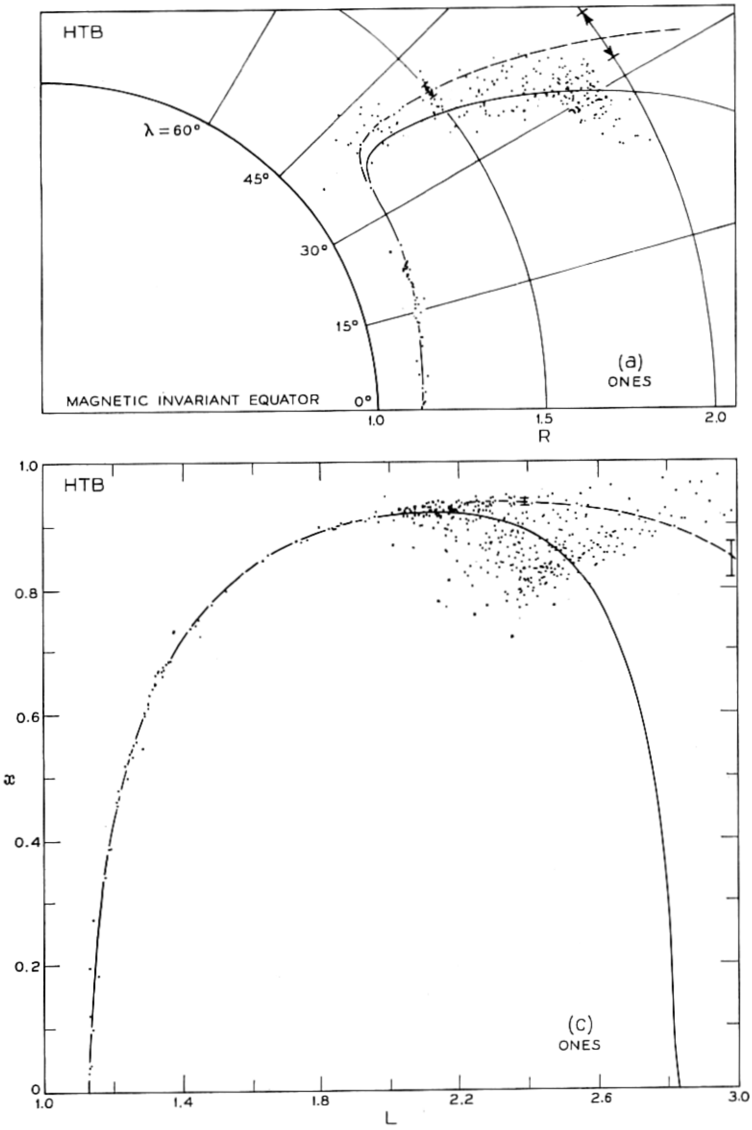

Fig. 23 — All positions for the HTB data in R, λ space (a) and x, L space (c) at which one count (one, two, and three counts for $L < 1.5$) was observed in an 11-second counting interval, and all positions in R, λ space (b) and x, L space (d) at which zero counts were observed in an 11-second counting interval. The solid lines are the loci of positions at which the HTB coefficients estimate one count in 11 seconds. The trace $R = 2.0\ R_e$, which explains the absence of data in the lower right-hand corner of the x, L plots, appears in part (d). The dashed

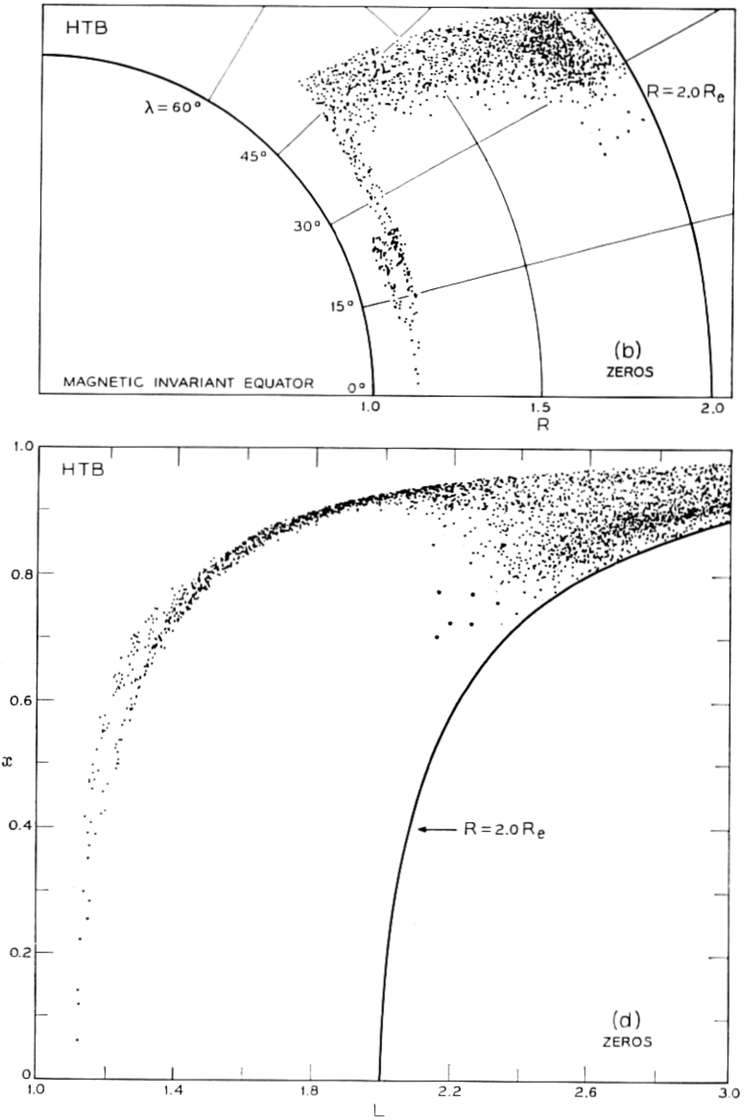

Fig. 23 — (continued)
lines are the loci of the cutoff function $x_c(L)$ or $R_c(L)$ calculated from the HTB coefficients. The cluster of points near $R = 1.1\ R_e$ and $\lambda = 20°$ in part (b) of the figure is data acquired by the telemetry station at Woomera, Australia. They represent observations made near perigee when the satellite was below the bottom edge of the proton belt, which is high over the western Pacific Ocean.

thus applies to the estimate of the *average* value of y and does *not* give the standard deviation of a single predicted observation. The latter would be in the neighborhood of $\sqrt{0.04} = 0.2$ (where 0.04 is approximately the MSE, see Table IV).

Contours of constant percent standard error in the *counting rate*, y^2, are shown by the curves in Fig. 24(a). For $L < 2$ the standard error is less than 2 percent except close to the cutoff, where the value of y^2 is falling fast. (Near the cutoff, the standard error in x_c is more informative.) In the absence of a fitted function, it would be necessary to average between about 30 and 300 observations to achieve a

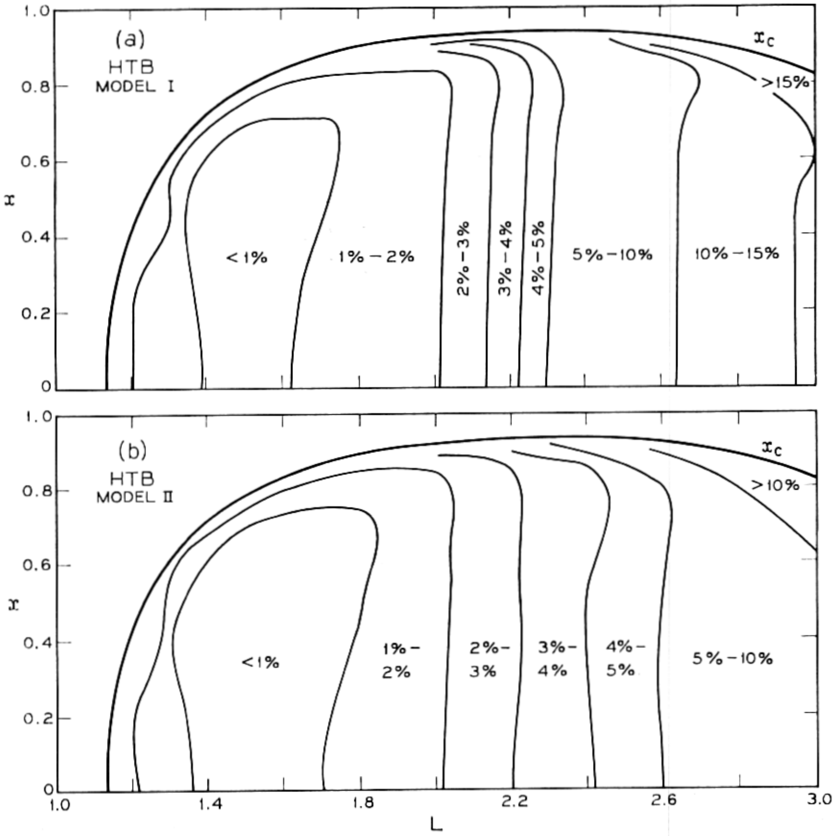

Fig. 24 — Contours of constant percent standard deviation in the *counting rate*, y^2, calculated from the fits to the HTB sample and plotted in x, L space. (a) Model I. (b) Model II.

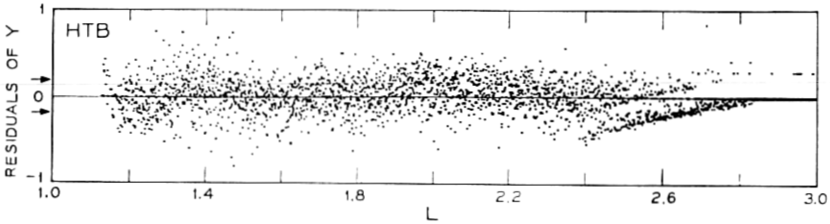

Fig. 25—HTB residuals of Y (i.e., $Y - y$ calculated from the HTB coefficients) plotted against L. The arrows indicate ± the approximate standard deviation if Y^2 were Poisson distributed.

standard deviation as small as 2 percent. As discussed in Appendix B.4, the estimates of the standard deviation based on the HTB sample are conservative and (if there were no biases in the model) the values that apply to the 40,000 HTB points might be smaller than those in Fig. 24(a) by a factor as large as 6.

The values in Fig. 24(a) are for relative counting rates (or fluxes) and do not include the uncertainty in the absolute calibration of the instrument noted at the end of Appendix A. Other discussion is given in Sections 9.4 and 12.2 and Appendix B.4.

7.7 *Behavior of the Fit on Several L-Slices*

Using the HTB coefficients, values of $y_L(x)$ were calculated for $L_m = 1.35$, 1.805, 2.0215, and 1.79. The results are plotted as the heavy solid lines in Figs. 4 to 7. Recall that the points in these figures are *not* all HTB points. In general, the HTB points are those with the higher values of Y, although this may not be the case at $L \approx 2.2$ because of the temporal effects discussed in Section X. The four figures also allow further appreciation of the difference in results between CB fit and the HTB fit produced by the partitioning of the data and the refinement of the procedure by which the sample was selected.

7.8 *Residuals in x,L Space*

The residuals, $Y - y$, were computed for all the HTB data using the HTB coefficients. Fig. 25 is a plot of residuals against L, and Figs. 26 and 27 are plots of residuals against x, in the indicated L-ranges. These plots are analogous to Figs. 13 to 15, and as they display properties similar to the earlier figures, the discussion of

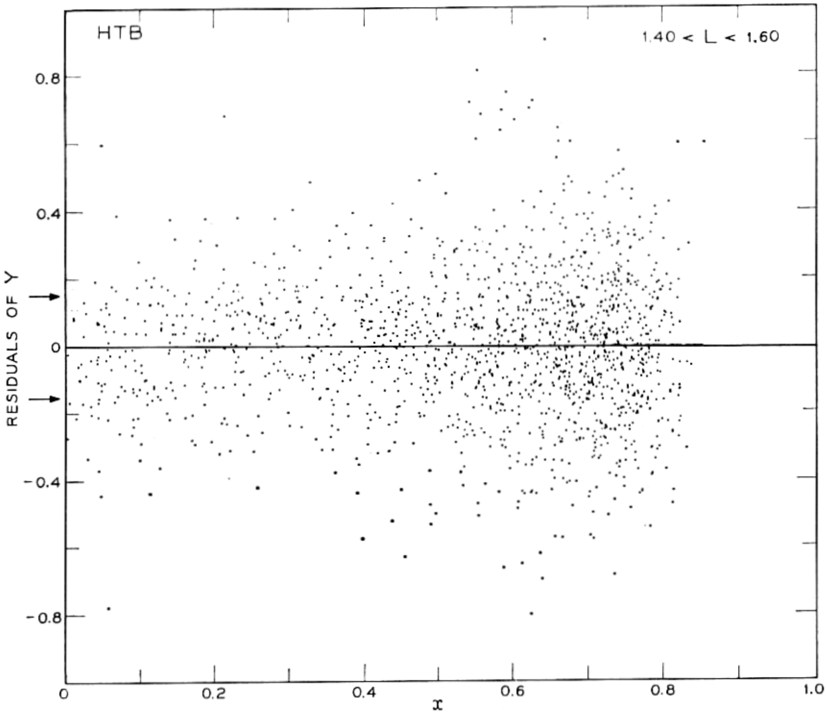

Fig. 26 — HTB residuals of Y (i.e., $Y - y$ calculated from the HTB coefficients) plotted against x for $1.40 < L < 1.60$. The arrows indicate ± the approximate standard deviation if Y^2 were Poisson distributed.

Section 6.6 applies. In particular, there is little indication of a dependence of the residuals on the magnetic coordinates. Moreover, the residuals in Figs. 25 to 27 are more closely clustered about zero than those in Figs. 13 to 15, confirming the fact that there is less scatter in the HTB data. This reduction in the scatter is especially marked in the neighborhood of the peak of the radiation belt (near $x = 0$ between $L = 1.4$ and $L = 1.6$, Fig. 26).

7.9 *Mean Square Residuals in x,L Space*

A breakdown of the mean square residuals (MSR) by L-ranges for the fit to the HTB data is given in Table III. This analysis is analogous to that presented in Section 6.7 for the CB fit. For the Group I data the MSR for the overall fit ($1.1 < L < 3.0$) is about $(1.5)(0.023) = 0.036$ and the largest entry under HTB Group I is

0.059. The anomalous trend of the MSR near $L = 1.4$ evidenced in the fit to the unrestricted data (see Section 6.7) has been largely eliminated. The overall MSR for the Group I data has been reduced by 15 percent.

The breakdown of the MSR by L-ranges is not a particularly refined test of the quality of the fit. This index is based on essentially all the HTB data and, because the averaging procedure is blind to the distribution of data within L-ranges, favors results that fit best where the density of data is high. As the HTB sample was selected using criteria dependent on the preliminary fit to the data and does not necessarily favor x,L regions in which large quantities of data were acquired, the results of fitting this sample does *not* produce the lowest obtainable value of MSR for all of the HTB data. Examina-

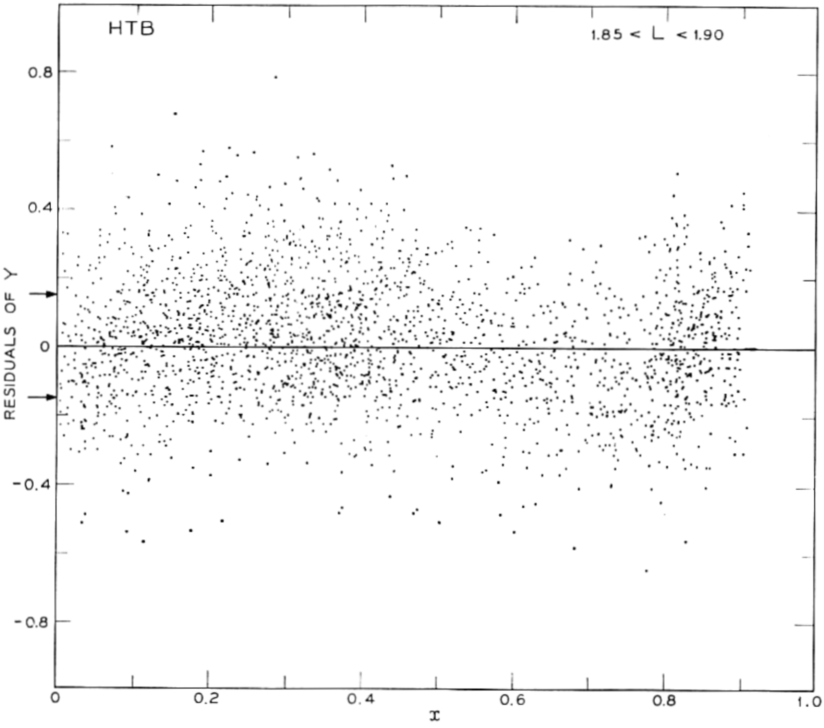

Fig. 27—HTB residuals of Y (i.e., $Y - y$ calculated from the HTB coefficients) plotted against x for $1.85 < L < 1.90$. The arrows indicate ± the approximate standard deviation if Y^2 were Poisson distributed.

tion of the MSR in x,L cells shows the effect of the sample selection procedure on the MSR in L-ranges. Appendix C contains further information and analysis of MSR in x,L cells.

Model I with the HTB coefficients, provides a summary of the HTB data that, in the light of the many sources of variability and measurement errors, reasonably approaches the limit set by expected statistical fluctuations.

7.10 *Sources of Variability in the Data*

The residuals for the HTB data are now examined to see whether further identifiable sources of variability may be associated with them. Possible sources are: instrumental effects, errors in the ephemeris of the satellite, errors in the description of the magnetic field, telemetry errors, fluctuations in the length of the counting interval, deficiencies in the model, and temporal variations. While all these must make some contribution to the MSR, the interrelationships among the coordinates discussed in Section 6.8 and the small size of the individual contributions, make positive identifications very difficult. We have not attempted to examine in detail the large number of small, apparently systematic, deviations discernible on the residual plots, although some of these may be "statistically significant." Instead we have restricted our study to effects which are readily apparent on the residual plots. Where the observations are dense, an effect would be glaringly apparent if it introduced a shift of ≈ 0.05 in the local mean of the residuals. (This corresponds to a change of about 1.2 percent in flux at the peak of the proton intensity, and about 12 percent when the flux is a hundredth of its peak value.)

Instrumental effects are associated with temperature, bias voltage, radiation damage, and imperfections in the omnidirectional characteristics of the detector. Restricting the range of temperature and bias voltage removed the major fraction of the instrumental effects associated with these variables. Directional effects in the detector might show up when the residuals are plotted against γ, the angle between the spin axis and the local magnetic field vector. However, no dependence was observed, indicating that the detector is effectively omnidirectional. Radiation damage, though technically an instrumental effect, is more logically treated with temporal variations.

Examination of plots of residuals versus various geographic coordinates did not reveal any systematic dependencies. In view of the small excess of the MSR over expectation for a random Poisson process, and the existence of other sources of error, it seems reasonable to conclude that the ephemerides were computed with sufficient accuracy for this analysis.

The plots of residuals against the geographic coordinates as well as against x and L values were used to judge the quality of the coefficients used to calculate the magnetic coordinates L and x. No systematic effects that can be attributed to flaws in the coefficients of the magnetic field were discerned. Nor is there any indication, in the form of excessive scatter of the residuals, that L is an imperfect coordinate in any part of the region of space covered by these data.

Gross telemetry errors and those that occur in conjunction with noise bursts are easily identified and have been discarded. There remain telemetry errors that are indistinguishable from good data on a point-by-point basis, and these erroneous data must make some contribution to the scatter. As noted in Section 8.1, the distribution of the residuals has been looked into and they are found to be very well-behaved. However, it is not possible to make any quantitative estimates of the contribution of the remaining telemetry errors to the MSR.

Temporal variations are an important source of variability, and Section X is devoted to their analysis.

VIII. STATISTICAL CRITIQUE OF MODEL I.

This section presents further information on statistical evaluation of the Model I fit. (Some background concerning relevant statistical techniques is given in Appendix B.) While confirming the very satisfactory performance of Model I in fitting the data, as presented in Section VII, some unsatisfactory aspects are uncovered and several defects of the model are pinpointed. The rectification of these defects is effected by use of Model II, discussed in Section IX.

8.1 *Fit of Model I to the 960-point HTB Sample*

The analysis of variance for the fit of Model I to the 960-point HTB sample is shown in Table IV. This gives various partitionings of the total sum of squares (about 0) of the 960 observations (on the square root of counting rate scale). Table IV indicates the relevance of the model to the data in terms of its statistical effectiveness. Fitting the nine coefficients of the model accounts for more than 99.3 percent of the total sum of squares of the observations, leaving less than 0.7 percent associated with "error" or lack of fit. On a per degree-of-freedom-basis, the ratio of mean square for "fitted model" with 9 degrees of freedom to mean square for "error" is over 16,000.

Of course, simply fitting the mean of all the data accounts for a sum of squares of 2121.2 of the total of 5374.7. Of the remaining "corrected" total sum of squares about the mean of 3253.6, the part of the model "orthogonal" to the mean accounts for 3218.9, i.e., approximately 98.9 percent (so that the squared multiple correlation coefficient, R^2, is 0.989). The corresponding ratio, mean square for the model with $(9 - 1) = 8$ degrees of freedom to mean square for error, is over 11,000.

It is worth emphasizing that the sample selection process which was used (see Section 7.1) is such that fitting the sample is, on a per observation basis, a more challenging problem than it would be for the entire body of data (see Appendix B.3).

A summary graphical indication of the appropriateness of the fit is given in Fig. 20 which shows the fitted value plotted against the observed value. A perfect fit (essentially impossible here with any model based on x,L coordinates because different integral values of Y are observed near the same x,L point) would be the diagonal straight line shown. Deviations from fit should be gauged as horizontal spread about the line, since the observed quantities are plotted as abscissa, and are seen to be reasonably uniform throughout.

Incisive indication of the quality of fit was provided by various plots of residuals (against L, x, y, time, etc.). Some representative plots over all the HTB data are shown in Figs. 25 to 27 and Figs. 41 to 43.

As a further examination of the adequacy of the fit to the selected HTB data, normal and half-normal probability plots (see Appendix B.8) were prepared for the 745 residuals comprising the subset of the 960-point HTB sample for which $x < x_c(L)$. These plots are shown in Figs. 28 and 29.

Fig. 28 does display a generally good linear configuration indicating that the residuals may reasonably be regarded as a sample from a normal distribution. There is no suggestion of general asymmetry or other distributional peculiarities. There are perhaps three values which are statistically "too large," but not wildly so. Indeed, the plot is remarkably well-behaved and reassuring.

From some points of view, it is useful to consider the statistical behavior of the residuals without regard to their sign. Fig. 29 is a plot of the ordered absolute residuals against standard half-normal (folded standard normal) quantiles. This presentation is more focussed and sensitive to a statistical overabundance of large absolute residuals. The plot is also very well-behaved, with indication of the same three overly large values.

The reason for omitting from these plots all residuals from points for which $x > x_c(L)$ is that, for those, the predicted value y is 0 and, in the great majority, the observed Y was 0; hence, the residual is 0. Since it was exactly this information which determined the estimate $x_c(L)$ and since one could hardly expect a collection which includes about ⅕ zeros to behave like a normal sample, these points were omitted

From either Figs. 28 or 29 one can estimate a slope of about 0.21, which is an estimate of the standard deviation of the (counting rate)$^{\frac{1}{2}}$ observations, clear of the confounding influence of the nonvariance-stabilized very low counting rate observations, since observations for $x > x_c(L)$ have been omitted. The corresponding variance estimate, 0.044, clearly exceeds that from the Poisson approximation, 0.023, and also is greater than the pooled value for the MSD(Y), 0.039,

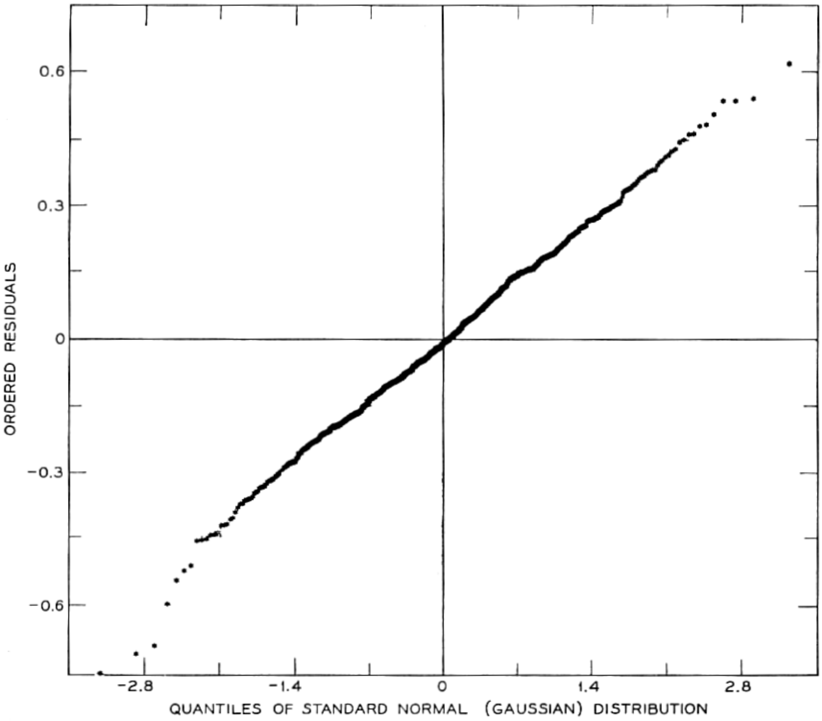

Fig. 28 — Normal probability plot of residuals from fit of the model to the HTB sample.

(Appendix C) the overall HTB data MSR(Y), 0.038, (Appendix C) as well as the MSE(Y) from the fit to the 960 points, 0.036, (Table IV). This is as one would expect, since the variance estimate from the slope of Figs. 28 and 29 is *not* downward biased by the zero (and $\sqrt{1/11}$) residuals from the very low counting rate observations for $x > x_c(L)$, while the other quantities *are* so biased.

The excess of the variance estimate of 0.044 over the Poisson value of 0.023 may be due to any or all of several factors, including: (*i*) the noncorrectness of the Poisson assumption, (*ii*) temporal variations in the radiation belts or the detection equipment, (*iii*) measurement errors or computational biases in time record, ephemeris or magnetic coordinates, etc. (*iv*) noise bursts—the outlandish values were detected and discarded, but the general effect must be an upward bias on variation, and (*v*) inadequacies in the model, including analytic form and coordinates employed.

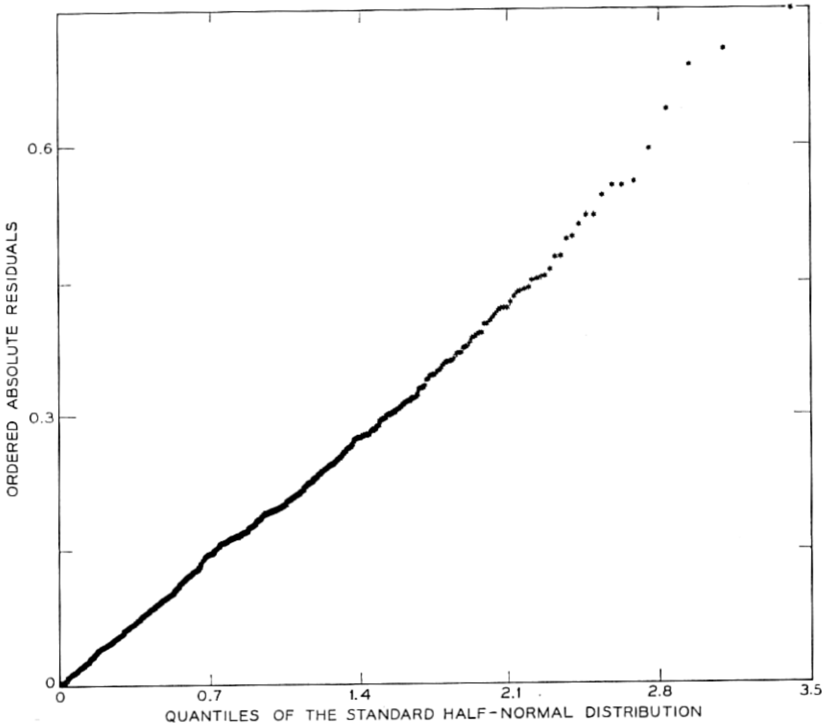

Fig. 29 — Half-normal probability plot of absolute residuals from fit of the model to the HTB sample.

8.2 *Statistical Measures Over All the HTB Data.*

An extensive presentation and comparison of various functions of the residuals over all the HTB data is given in Appendix C. Those results provide (*i*) an empirical justification for the use of the square root transformation; (*ii*) a strong indication that the fit attained by Model I cannot be improved very much in the least squares sense over all the HTB data; (*iii*) information on the extent of "unevenness" of the cell-construction process by which the 960-point HTB sample was selected; and (*iv*) some indication of differential effectiveness of fit of Model I to the data for different x,L regions.

8.3 *Statistical Properties of Estimates of the Coefficients and Coefficient Functions.*

The least squares estimates of the nine coefficients of Model I fitted to the 960-point HTB sample are given in Table IV, with their approximate standard errors and pairwise correlations.* These provide the information needed to obtain estimates and standard errors for functions of the coefficients; e.g., $y'(x,L)$, or $A'(L)$, or the value of the maximum counting rate, or the position in space at which the intensity of high energy protons is maximum, etc. (See Appendix B for the necessary formulae.)

Some of the pairwise correlations in Table IV are exceedingly high. This may be due, in general, either to an unfortunate "design" (i.e., the array of positions of observations in x,L space in this application) or to some inherent "coefficient redundancy" in the model, or to both such blemishes. Occurrence of such near-singularities can lead to practical difficulty with the iterative fitting computation and/or make the individual coefficient estimates poorly determined.

In the present model, only the coefficient L_0 has a direct physical interpretation. Its estimate has a very small standard error and an entirely bearable correlation with the remaining coefficient estimates (all values of $|\alpha| < 0.5$). Otherwise, physical interest centers mainly on the coefficient functions $A'(L)$, $x_c(L)$, and $y'(x,L)$ whose estimation is considered in Sections 7.2, 7.4, 7.5, 7.6, and 8.4.

For a given model and specified coefficient values, the matrix of approximate correlations depends only on the array of data positions in x,L space. Thus, to check on whether the correlational problems might

---

* A rescaling of the values of ρ, namely as the quantity α defined and motivated in Appendix B.5, is also given in Table IV. The coefficient of dependence α has more nearly the behavior of a "linear utility function."

be due to inadequacy of the practically available (selected) array, a correlation matrix was computed using an 'ideal' x,L array, namely the 1034 values of (x,L) corresponding to the division of x,L space described in Section 7.1 and Appendix B.3. While some minor improvements in some of the correlations were noted, the changes were small. Thus, it would appear that the main reason for the high correlations is in fact some "coefficient redundancy" in the model.

Inspection of Table IV indicates that the very large correlations are associated with some of the parameters of the $A'(L)$ function, namely a_1, a_2, a_3, and η for all pairs of which $|\rho| > 0.99$ (i.e., $|\alpha| > 0.90$). Moreover, it will be seen in Section 8.5 below, that the present parameterization of the model leads to a markedly large indication of nonlinearity and there is reason for believing that this is largely due to the same subset of coefficients. The combination of both defects stimulated development of Model II which overcame them (see Section IX).

8.4 *Estimates of Functions of the Coefficients*

The estimates of the coefficient functions $A'(L)$ and $x_c(L)$ have been discussed in Sections 7.4 and 7.5 and summarized in Figs. 10 and 11. Their estimated standard deviations, on a "pointwise" basis, are graphed in Fig. 22(a), while the approximate correlations of the estimates of $A'(L)$, $x_c(L)$, and S, as functions of L, are shown in Fig. 30(a).

Despite the near-singularities (i.e., $|\rho|$ near 1) in the estimates of some of the individual coefficients of $A'(L)$, it is seen that the estimate of the square root of the equatorial counting rate provided by $A'(L)$ is well-determined over the entire L range. The standard error varies between approximate limits of 0.018 and 0.040, nonmonotonically, and these values are typically less, sometimes by a factor of 5 or more, than the standard errors from the corresponding L-slice estimates (see Table II) reflecting in part the statistical gain from the simultaneous two-dimensional fit.

For $x_c(L)$, the standard error is less than 1 percent over much of the range of L, rising to 3 percent for large L values where the data are statistically inadequate.

The three correlation functions $\rho_{A,x_c}(L)$, $\rho_{A,S}(L)$, and $\rho_{S,x_c}(L)$, for the estimated coefficient functions $A'(L)$, $x_c(L)$, and S, are plotted in Fig. 30(a) (see Appendix B.4 for formulae). In general, these correlations are small ($|\rho| < 0.5$, $|\alpha| < 0.12$). The statement applies to the correlations involving $A'(L)$ despite the very high correlations among individual coefficients. The generally low correlation between $A'(L)$ and $x_c(L)$ is as intuitively expected since $A'(L)$ is influenced mainly

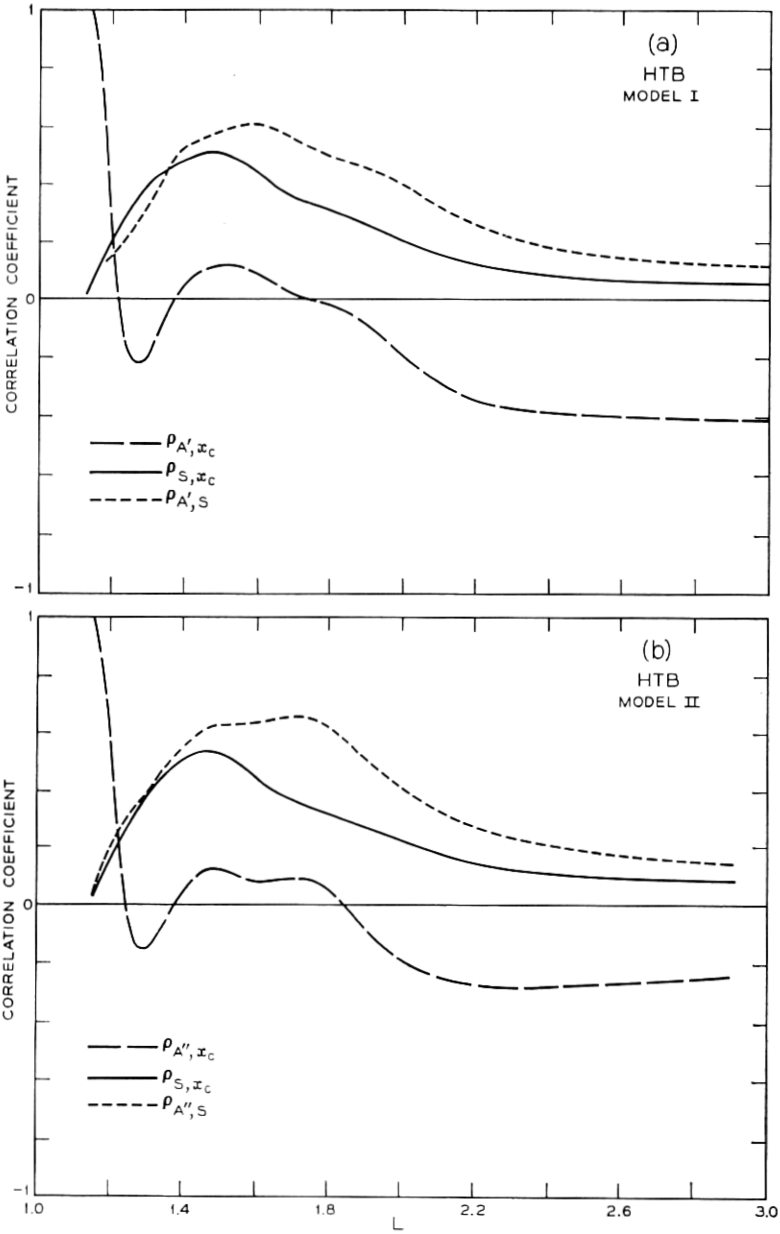

Fig. 30 — Correlation coefficients of A with S, S with x_c, and A with x_c, calculated from the fits to the HTB sample and plotted as functions of L. (a) Model I. (b) Model II.

by observations at small x while $x_c(L)$ is determined mainly by those at large x. The exception is near $L = L_0$, where $\rho_{A,x_c}(L_0)$ approaches 1 as a result of the fact that the coefficient L_0 is common to both functions and that the forms of $A'(L)$ and $x_c(L)$ [see (4), (5), and (6)] require that both functions be zero when $L = L_0$.

The statistical correlation between the fitted A and x_c for the L-slice fits was always positive (see Table II), which is not the case for $\rho_{A,x_c}(L)$. This change in sign gives some indication of basic differences in behavior between the results of the two-dimensional fit and the outcome of the *collection* of one-dimensional L-slice fits.

The (A, S) and (S, x_c) correlations have the same signs in all cases. The magnitude of the correlations among A, x_c, and S is larger for the L-slice fits (see Table II) than for the HTB fit at corresponding values of L [see Fig. 30(a)]. This is very noticeable for L greater than ≈ 1.7. particularly for the large correlation between S and x_c. It is these large correlations which make it difficult to obtain reliable L-slice estimates of x_c or S when $L_m > 2$ (see Fig. 6) or when the distribution of the data within an L-slice is poor (see Fig. 7).

8.5 *Nonlinearity Indices and Dependence of Estimates*

Appendix B.5 discusses the use of the sum of squares function (i.e., sum of squares of differences between observed value and "fitted" value, as a function of proposed coefficients) as an indicator of the joint dependence and behaviour of the coefficient estimates and the fact that the extent to which the contours of the sum of squares function are approximated by a certain family of ellipsoids provides a measure of linearity of the model.

Fig. 31 shows 4 of the 36 pairwise projections of the 9-dimensional ellipsoid, whose size would correspond to a "0.99 joint confidence coefficient" as discussed in Appendix B.5. The axes are scaled in each case according to the standard error of the coefficient. The orientation and shape of the ellipse corresponds directly to the sign and magnitude of the correlation, ρ, or its transform, α, for the pair of coefficients. Thus, for example, Fig. 31(a) shows the projection onto the a_1-a_3 plane. The resulting very narrow positively inclined ellipse corresponds to a very high positive correlation of a_1, a_3 ($\rho = 0.9995$, $\alpha = 0.97$). (The 45° inclination of the graphed ellipses is a result of scaling the axes by their standard errors.) Part (b) of the figure shows a narrow negatively inclined ellipse for the case of rather large negative correlation between a_3 and η estimates. Parts (c) and (d) illustrate results for small and negligible correlations between L_0, r_2 and r_3, S, respectively.

At various positions on these ellipses there appear numbers which are ratios of the actual sum of squares at that "point" to the minimum sum of squares. The computation of the actual sum of squares is done for the coefficient values corresponding to the point on the 9-dimensional ellipsoid which projects into the point on the plotted ellipse.

If, in fact, the coefficients occurred linearly, all of these numbers on all of the pairwise ellipses would be constant and in the present case would have the value 1.023 corresponding to a sum of squares of residuals of about 35.47. As a basis for judging the actual values and their variability, the following table gives values which this ratio would have, if the coefficients did occur linearly, for various joint (9-dimensional) "confidence coefficients:"

Conf. Coeff.	*Contour Ratio*
0.90	1.015
0.95	1.018
0.99	1.023
0.999	1.029

In view of the variability of the actual ratios in Fig. 31, and of the extent to which some depart from the values in the above table, it is clear that in the present form of the model the coefficients behave jointly in a markedly nonlinear fashion even in a relatively small neighborhood around the least squares estimate.

Inspection of the entire set of $(9)(8)/2 = 36$ pairwise plots strongly suggests that a major part of this nonlinear behavior derives from the coefficients a_1, a_2, a_3, and η of the $A'(L)$ part of the model. These also are the coefficients whose estimates exhibit the undesirably high correlations which have been shown above to be due mainly to a "coefficient redundancy" in the model.

Direct interpretation of the ellipses in Fig. 31, as indicating interdependence of the coefficient estimates, depends heavily on the appropriateness of the linear approximation in the neighborhood of the least squares estimate. Since the nonlinearity index is in fact distressingly large one must be cautious in interpreting the ellipses or their associated correlation or dependence coefficients.

8.6 *Summary Statistical Criticisms of Model I.*

Model I, with coefficients determined by fitting to the 960-point HTB sample, has been shown to provide a very good fit both to the

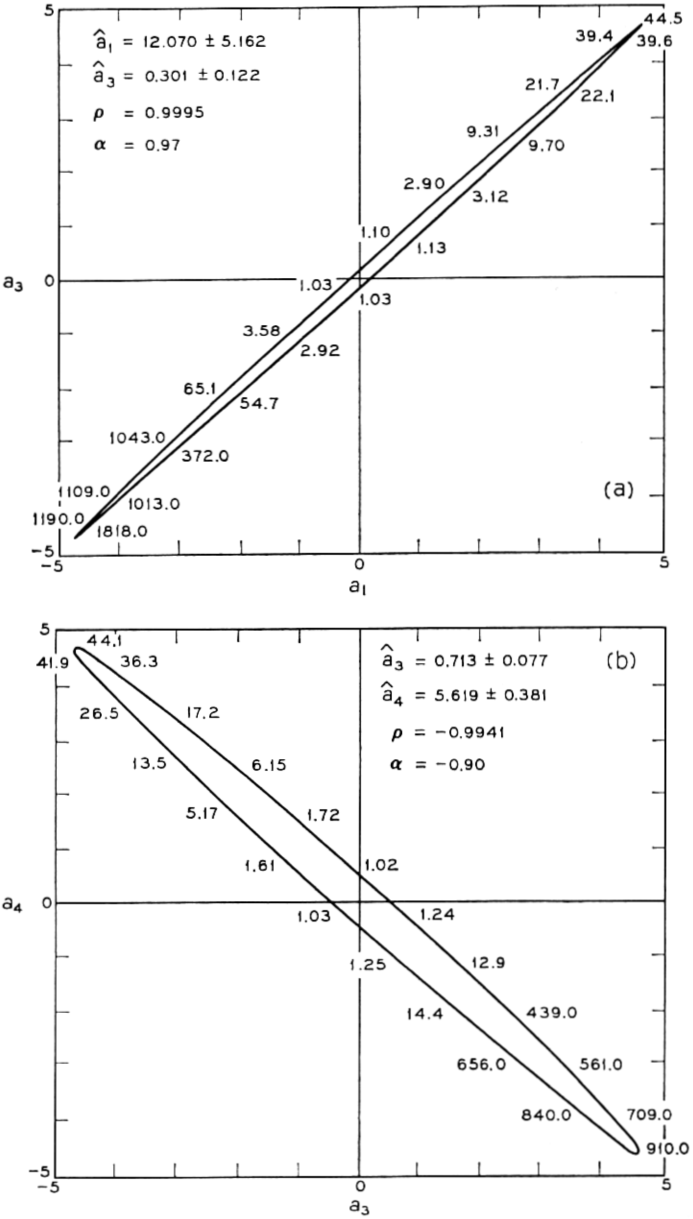

Fig. 31 — Examples of projections of the approximate "0.99 joint confidence region" for the estimates of Model I. (Axes are scaled by standard errors.)

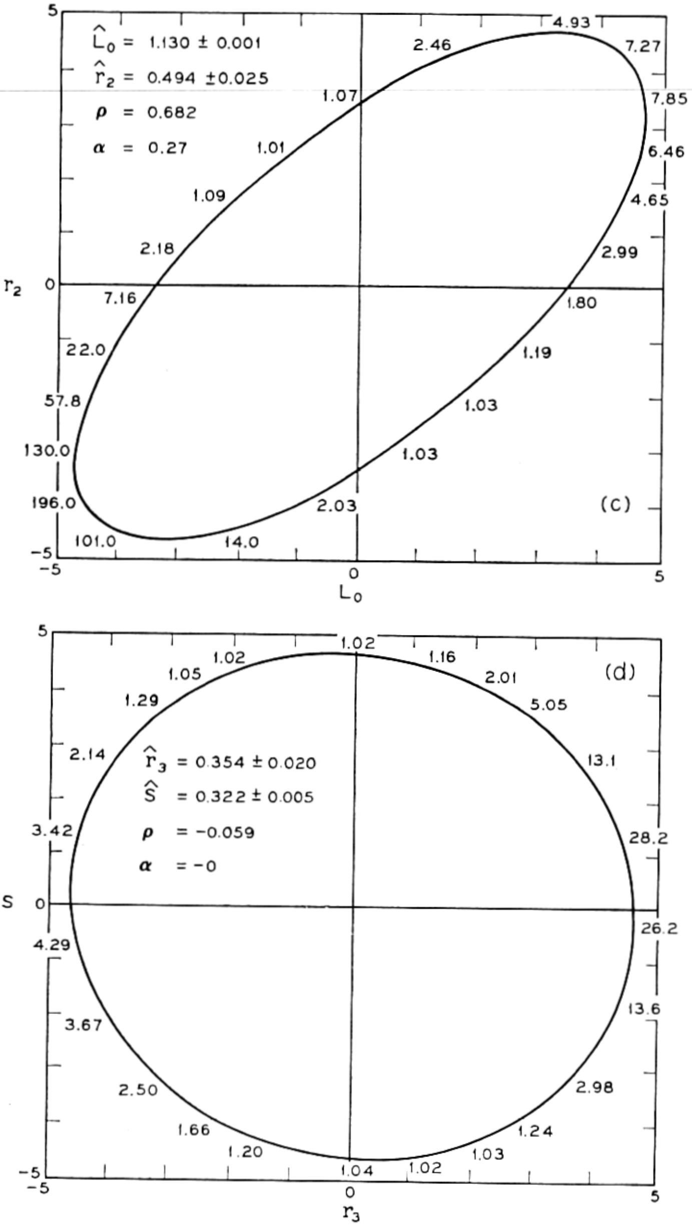

Fig. 31 — (continued)

sample and to the entire body of some 41,000 HTB observations. Moreover, the interesting coefficient functions $y'(x,L)$, $A'(L)$, and $x_c(L)$ have stable statistical properties as has the physically interpretable coefficient L_0.

However, the model has two statistical defects: Firstly, although the model gives an extremely good fit to the data, the parameters a_1, a_2, a_3, and η of the $A'(L)$ part of the model have exceedingly high mutual correlations (see Table IV), and these were shown *not* to be due to an obviously defective design. Secondly, the model coefficients exhibited distressingly high nonlinearity of behavior even within rather close neighborhoods of their least squares estimates, with grounds to suspect that this was caused by the a_1, a_2, a_3, η group of coefficients. In addition, most of the coefficients of Model I do not have any directly meaningful physical interpretation.

The modifications which led to Model II, as discussed in the following Section IX, overcome these defects of Model I while retaining all its virtues.

IX. THE MODEL II FIT TO THE HTB DATA

This section presents the statistical analysis of the HTB data using Model II, a modified version of Model I. The emphasis in the presentation is on comparisons of Models I and II. Since it is shown how very closely the fit of Model II approximates that of Model I, such aspects as the direct presentation of Model II residuals overall the data are unnecessary, and hence omittted.

9.1 *Model II*

The definition of Model II has been given in Section 4.6, together with a discussion of the physical interpretation of its coefficients and its mathematical relation to Model I. Specifically, the 8-coefficient Model II constitutes a specialization and reparameterization of the 9-coefficient Model I. Thus, it follows that the minimum sum of squares in fitting Model II to any body of data can not be less than that from fitting Model I, though this may not be true of the mean square error.

The evolution of Model II from Model I did not arise from any simply described systematic process, as is indeed true in other aspects of this study. Once the basic achievements of Model I were established it was then opportune to focus on major remaining defects. The character of these defects strongly urged elimination of one or more coefficients in conjunction with a nonlinear reparameterization of the coefficients. The solution achieved was arrived at by empiricism, persistence and good luck.

The remainder of this section documents the assertion that Model II retains all the virtues of Model I while overcoming its defects.

9.2 *The Fit of Model II to the 960-point HTB Sample.*

The analysis of variance from fitting the 960-point HTB sample by means of the 8-coefficient Model II is given in Table V. As expected, the residual sum of squares, 34.7126, of Table V exceeds that of Table IV, namely 34.6675. This difference is associated with the one-degree-of-freedom nonlinear constraint defined in (13). Thus, we see that the sum of squares associated with the one-degree-of-freedom non-linear constraint is (34.7126-34.6675) $= 0.0451$ and this gives a ratio of less than 1.24 in relation to the mean square error of 0.03645. The value 1.24 corresponds to the upper tail 27 percent point of the chi-squared-with-one-degree-of-freedom distribution. The proportionate increases in the sum of squares for error is about 0.13 percent and the increase in the mean square error is less than one part in 3000. Multiple $R^2 = 0.989$ is effectively unchanged.

For the models of both Tables IV and V, the coefficient S is treated as constant with L. If Model II is modified so that $S(L) = s_0 + s_1 L$, then, fitting this 9-parameter version of Model II yields a sum of squares for error of 34.520. Thus, we would have a sum of squares of (34.713-34.520) $= 0.193$ associated with the "hypothesis" $s_1 = 0$. The main point of quoting this result is to indicate that these minor differences in the sums of squares for error are judged as unimportant in this context, even if under some highly formalized assumptions the distinctions are "statistically significant."

Of greater interest and sensitivity are the following considerations: (*i*) the behavior of the residuals from Model II as functions of x,L and y; (*ii*) the behavior of the differences between Models I and II; (*iii*) comparisons of the estimates of $A'(L)$ of Model I and $A''(L)$ of Model II [see (6) and (11)]; (*iv*) comparisons of the estimates of $x_c(L)$ from the two models; (*v*) the pattern of correlations of the estimates of the eight Model II coefficients; and (*vi*) the indices of nonlinearity for the coefficients of Model II.

9.3 *Residuals of Model II Fit and Differences Between Models I and II.*

Figs. 32, 33, and 34 are plots of the residuals of the 960-point HTB sample from the fitted values of Model II against L, x and Y, re-

TABLE V—FIT OF MODEL II TO 960-POINT HTB SAMPLE.

Analysis of variance

Due to	d.f.*	Sum of squares	Mean square
Total	960	5374.7321	
Model	8	5340.0195	667.5024
Error	952	34.7126	0.0365

Coefficient estimates

	A_p	L_0	L_p	η	r_1	r_2	r_3	S
Estimate	8.0762	1.1293	1.4644	5.2187	0.2658	−0.5082	0.3638	0.3225
standard error	0.0342	0.0009	0.0016	0.0474	0.0083	0.0241	0.0196	0.0047

α values

		A_p	L_0	L_p	η	r_1	r_2	r_3	S
ρ values	A_p		0.01	0.00	0.02	−0.02	0.01	−0.02	0.21
	L_0	0.140		−0.05	−0.11	−0.41	0.19	−0.09	0.00
	L_p	0.046	−0.304		0.39	0.00	0.00	−0.01	0.01
	η	0.203	−0.451	0.794		0.02	−0.00	−0.01	−0.00
	r_1	−0.181	−0.806	0.045	0.214		−0.62	0.39	−0.01
	r_2	0.162	0.589	0.090	−0.021	−0.923		−0.71	0.00
	r_3	−0.171	−0.422	−0.151	−0.107	0.793	−0.956		−0.00
	S	0.609	0.015	0.099	−0.010	−0.168	0.098	−0.085	

* degrees of freedom

spectively. These plots show no systematic structure and are quite similar to analogous plots for Model I. Furthermore, Fig. 35, showing the observed Y versus fitted y'' for Model II, is as well-behaved as the corresponding Fig. 20 for Model I.

Figs. 36, 37, and 38 show the deviations between the fitted Models I and II plotted against L, x, and Y, respectively. Of course these figures show a systematic structure since one is plotting the difference of two smooth functions. However, the actual differences are totally insignificant in the light of the data. (Note that the scale for Figs. 36, 37, and 38 differs from that of Figs. 32, 33, and 34 by a factor of 10.)

Thus, on the basis of one less coefficient, Model II fits the data essentially as well as Model I, to which indeed it is a very excellent approximation. It has the merit that the physically arbitrary coef-

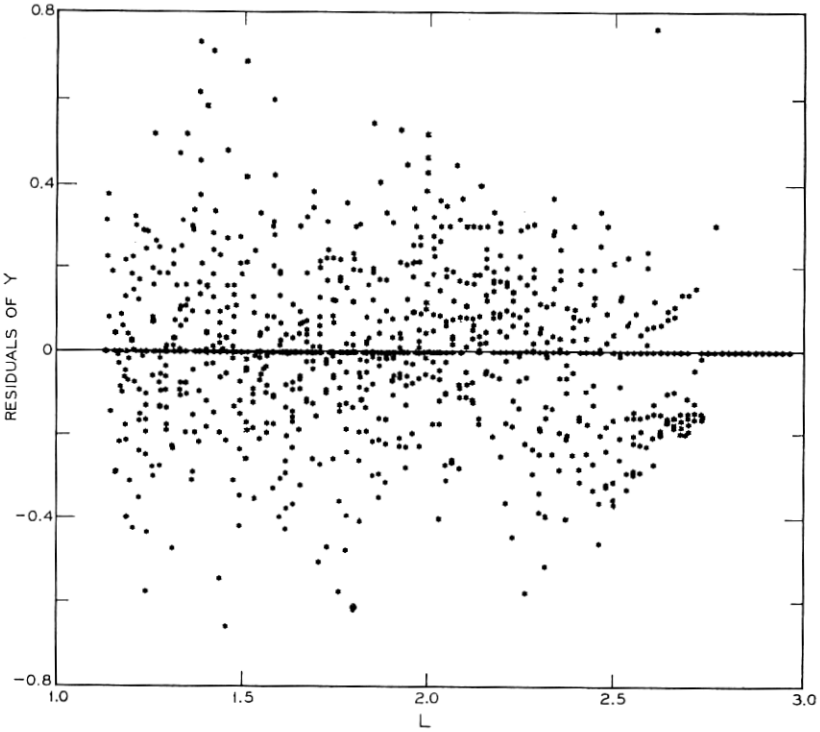

Fig. 32 — Residuals ($Y - y$) from the fit of Model II to the 960-point HTB sample vs L.

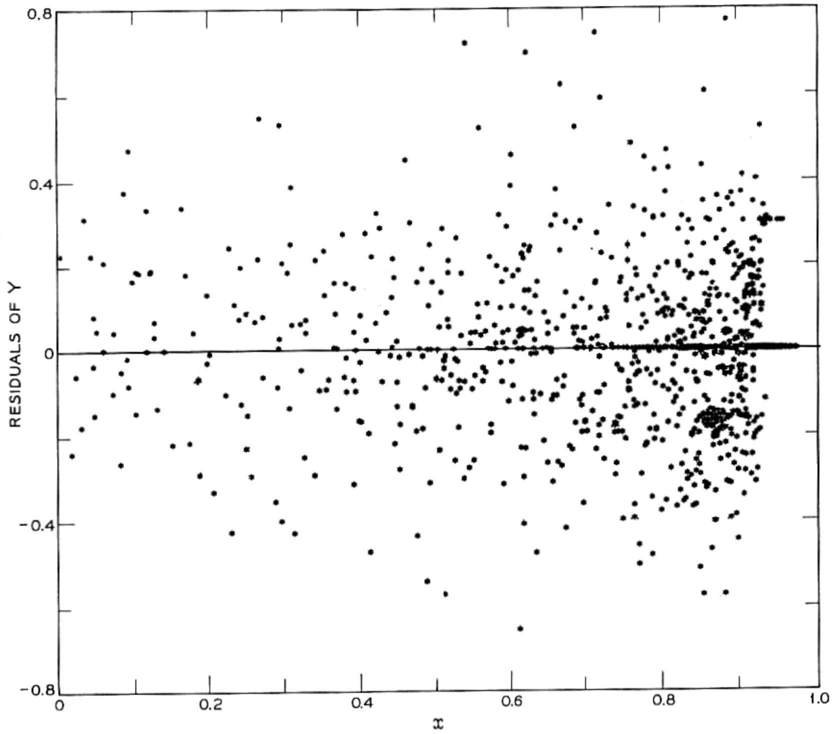

Fig. 33 — Residuals $(Y - y)$ from the fit of Model II to the 960-point HTB sample vs. x.

ficients a_1, a_2, and a_3 of Model I have been replaced by A_p and L_p which do have direct physical interpretations. As will be detailed in the next subsection, Model II also has additional attractive statistical attributes.

9.4 *Coefficient Estimates*

Table V gives the least squares estimates of the eight coefficients of Model II together with their approximate standard errors, correlations and α values. The estimates are seen to be extremely well-determined. In particular, for the physically meaningful quantities A_p, L_0, and L_p the standard errors are about 0.4, 0.1, and 0.15 percent, respectively, while for the shape coefficients η and S they are about 1 and 1.5 percent, respectively.

Comparison with Table IV shows that the standard error has decreased for *every* coefficient which is common to the models. The most dramatic change is for η for which the standard error diminished by a factor of about 8.

The estimates of $A'(L)$ and $A''(L)$ are in very close correspondence as implied by Fig. 36. The comparison of Fig. 22(b) with Fig. 22(a) indicates that the standard error of $A''(L)$ is uniformly lower than (but in general agreement with) that of $A'(L)$.

Entirely similar remarks apply to comparison of estimates of $x_c(L)$ from Models I and II, as also documented by Figs. 22(a) and 22(b).

It has already been shown that the fitted values of $y'(x, L)$ and $y''(x, L)$ are in very close agreement. The pattern of contours of the percent standard errors of $[y''(x, L)]^2$, in Fig. 24(b), shows that the standard error is everywhere smaller than the corresponding results for Model I, in Fig. 24(a).

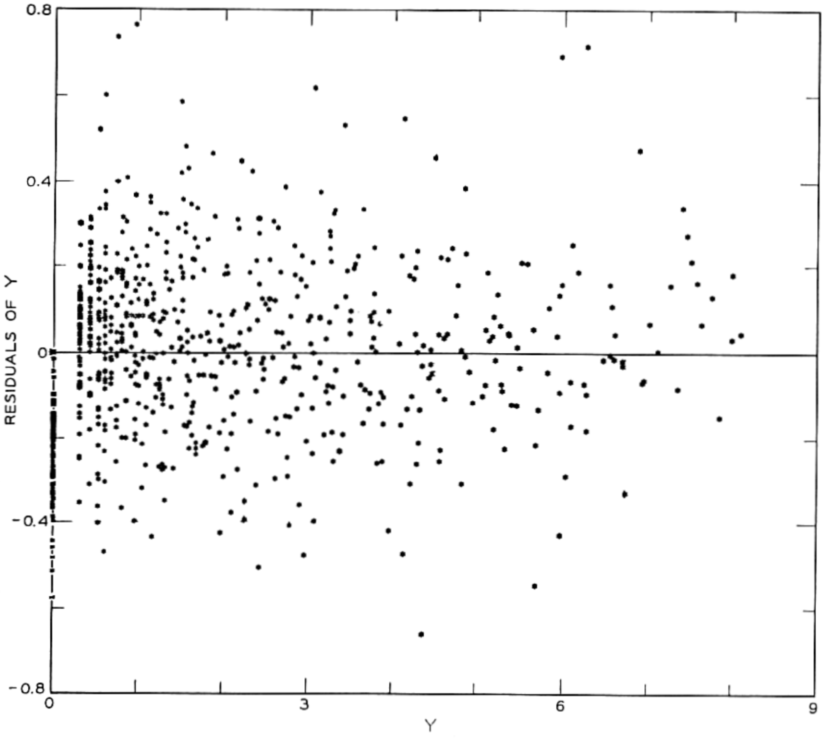

Fig. 34 — Residuals ($Y - y$) from the fit of Model II to the 960-point HTB sample vs Y.

One of the most dramatic changes between Models I and II is indicated by comparison of the correlations in Tables IV and V. The very large correlations ($|\rho| > 0.99$, $|\alpha| > 0.9$) among the $A'(L)$ coefficients of Model I do not occur for Model II. Only the (r_1, r_2) and (r_2, r_3) coefficient pairs of Model II have $|\alpha|$ values above 0.5. This is inconsequential since these are physically arbitrary coefficients of a cubic polynomial.

The correlations of $A''(L)$, $x_c(L)$, and S from Model II remain much like the corresponding results for Model I, as shown in Fig. 30.

9.5 *Nonlinearity Indices*

The further virtuosity of Model II is indicated by the behavior of the nonlinearity index shown for the examples of "confidence regions"

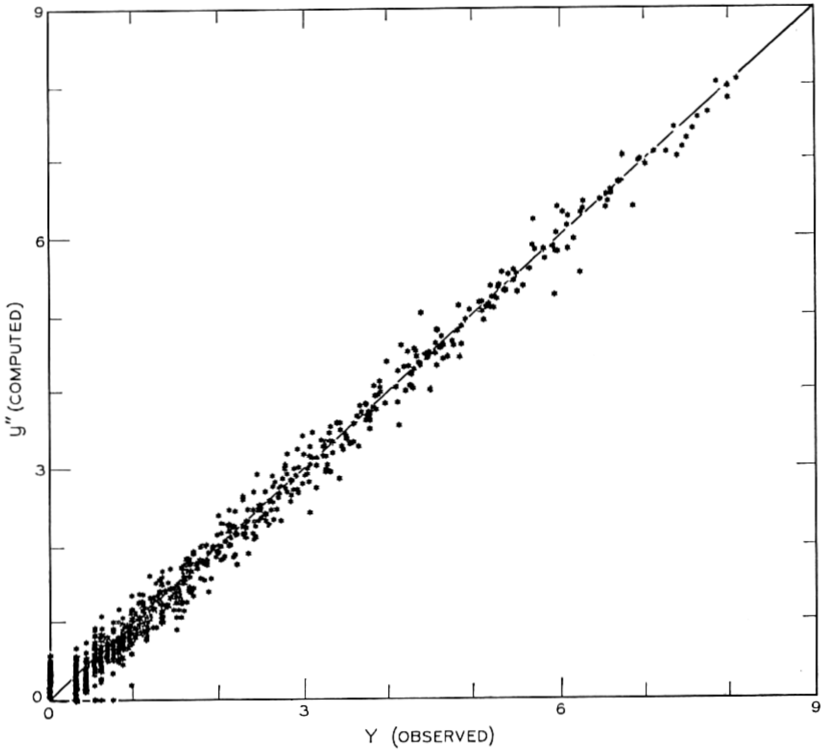

Fig. 35 — The value of y'' computed from the fit of Model II vs the observed value, Y, for the 960-point HTB sample.

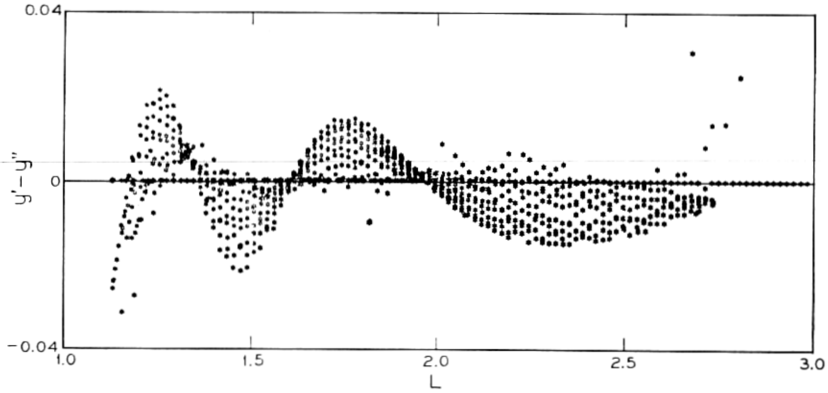

Fig. 36 — Deviations between the Model-I fit, y', and the Model-II fit, y'', vs L, for the 960-point HTB sample.

in Fig. 39. (See Appendix B for general discussion and definition.) Specifically, it is seen that the numbers on the ellipses vary very little and this is true for all 28 of these ellipses. These numbers would be constant and all equal to 1.023 if the model were linear in the fitted coefficients. Comparatively, Model II does indeed behave in a reassuringly linear fashion. For sharp contrast, we may compare Fig. 39 with Fig. 31, for Model I, in which the values range up to 1000 around the 9-dimensional ellipsoid.

The nonlinear behavior of Model I in relation to the linear be-

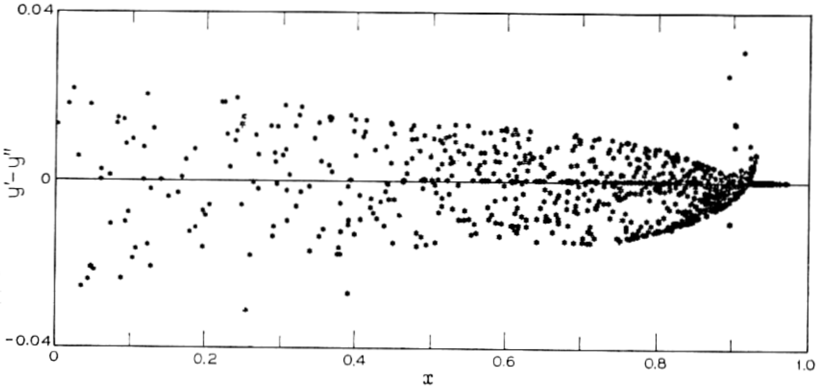

Fig. 37 — Deviations between the Model-I fit, y', and the Model-II fit, y'', vs x, for the 960-point HTB sample.

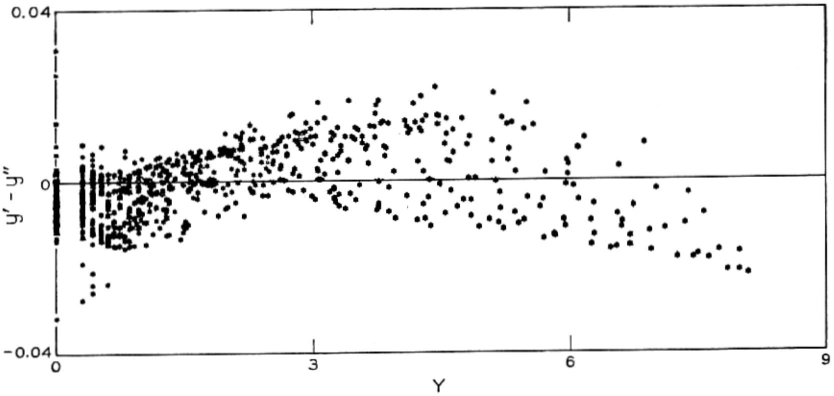

Fig. 38 — Deviations between the Model-I fit, y', and the Model-II fit, y'', vs Y, for the 960-point HTB sample.

havior of its specialized reparameterized version, Model II, is indicative of the reason for the high nonlinearity indices for Model I. Effectively, a p-coefficient model defines a constraining "surface" of p dimensions (p is 9 and 8 for Models I and II, respectively) in the n-dimensional space of the observations (n is 960 in the present case). In a small neighborhood of the least squares estimate, this p-dimensional surface may or may not be planar. If the latter, one will obtain high indices of nonlinearity. If the former, then one will or will not obtain high nonlinearity indices according to whether the individual coefficient *coordinates* within the p-dimensional surface are or are not linearly behaved.

It is likely that the 9-dimensional surface defined by Model I is indeed reasonably planar, but the coordinate system defined by the coefficients is highly nonlinear.

The correlation and nonlinearity effects, it should be noted, are not in principle related. One can have very high correlations with linear models and very low correlations with very nonlinear ones.

9.6 *Summary Comments*

Model II has been presented and validated as an evolution of Model I. Though Model II represents the current recommended fit from this study, several aspects of its justification, and of other comparisons in this paper, are based on the Model I fit. For example, the statistical study of residuals over all the HTB data, discussed in various places including Appendix C, is based on Model I. This hybrid attitude is entirely sound, since the range of deviation between Models I and II is small compared to the range of residuals from the fitted sample.

Thus Model II provides a fit to the HTB in which the 8 estimated coefficients provide a "good description" of about 41,000 observations. The deviations of the fit from the data are within reasonable statistical fluctuations—variation in telemetered counting rates, orbital errors, observational errors, mapping-to-magnetic-coordinate uncertainties, etc. (See Appendix C.3). A number of the coefficients have physical interpretations and these are statistically well-determined and relatively uncorrelated. Model II, though nonlinear in the coefficients, behaves in a very linear fashion in the neighborhood of the least squares estimates.

X. TEMPORAL VARIATIONS

This section and the two to follow are devoted to discussion of some specific physical results of the analysis.

Temporal variations are considered in three classes: diurnal (day-night), secular, and short term. Residual plots were used to study these effects.

10.1 *Diurnal Effects*

The HTB residuals were plotted against local time for various x,L regions. The HTB data are not well-distributed in local time near the magnetic dipole equator, making it difficult to draw firm conclusions. However, no evidence of a diurnal variation was found.

Specifically, to produce a change of about two percent in the average value of Y on the equator ($x = 0$) would require a diurnal shift in the radial position of the magnetic field line of about 0.01 R_e at $L = 1.35$, and a shift of about 0.02 R_e at $L = 1.55$, if there were no other effects. At these two positions, the value of y is large ($y \approx 8$) and $\partial y/\partial L$ is large, and a two-percent change in y would correspond to a shift in the mean of the residuals of $\approx$0.16 between noon and midnight local time. An effect of this magnitude would be readily observable on the residual plots.

Thus, it is unlikely that displacements larger than 70 km and 140 km, at equatorial L's of 1.35 and 1.55, respectively, would escape detection, and these distances are offered as upper limits to the day-night changes of the magnetic field at the two positions. As both of these displacements are equivalent to a change in field strength of

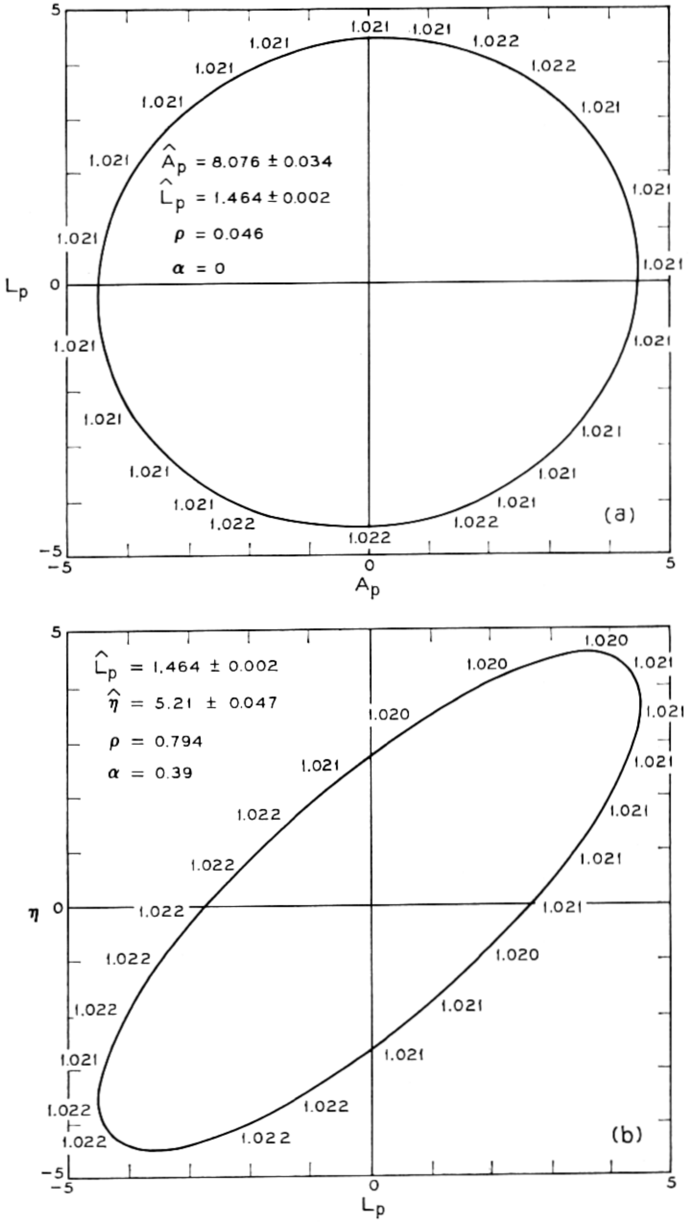

Fig. 39 — Examples of projections of the approximate "0.99 joint confidence region" for the estimates of Model II. (Axes are scaled by standard errors.)

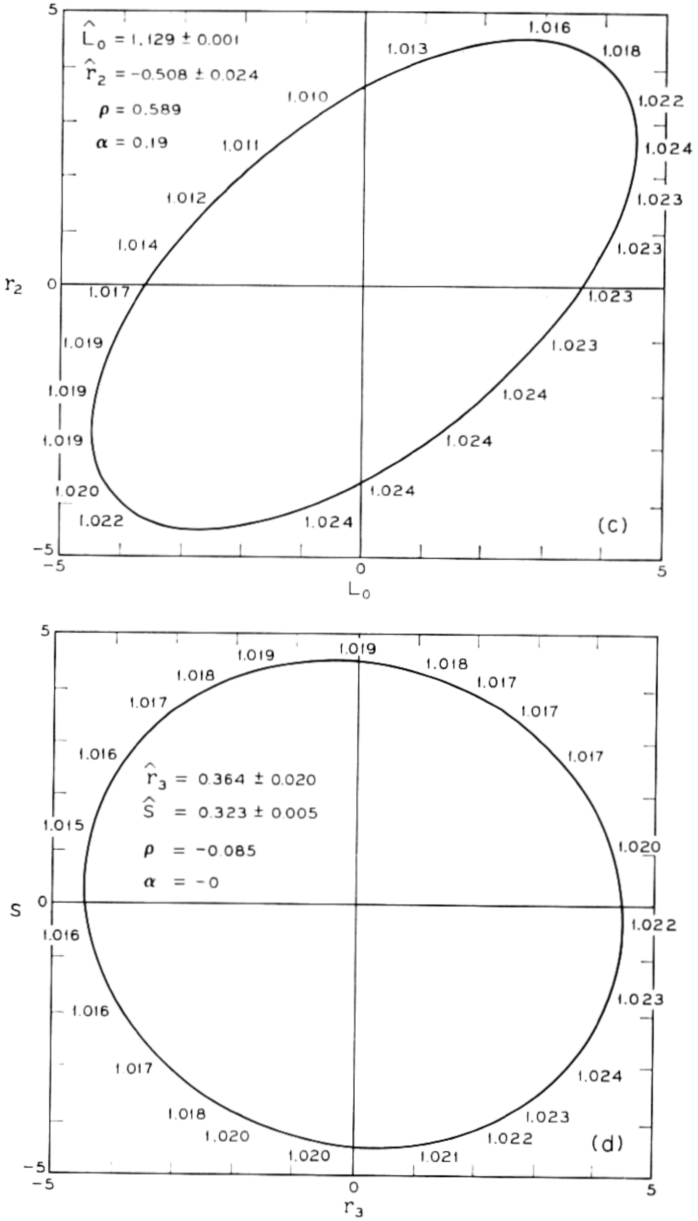

Fig. 39 — (continued)

about 300 gamma (0.003 gauss), this particle experiment does not qualify as a sensitive indicator of adiabatic changes in the earth's magnetic field.

10.2 *Secular Effects*

The HTB residuals are plotted against elapsed time, in days, for $1.85 < L < 1.90$, in Fig. 40. It would appear that the average value of Y decreased between days 191 and 255. This decrease is exhibited in all parts of the belt where we have measurements during this interval. Between days 191 and 225, the orbit of the *Telstar*® 1 satellite did not take it into the central region of the belt $\{1.3 \leqq L \leqq 1.8, \lambda \leqq 10°\}$. In other regions the decrease in the average value of Y over this period is about ten percent. The extremes are two percent and 20 percent, but it

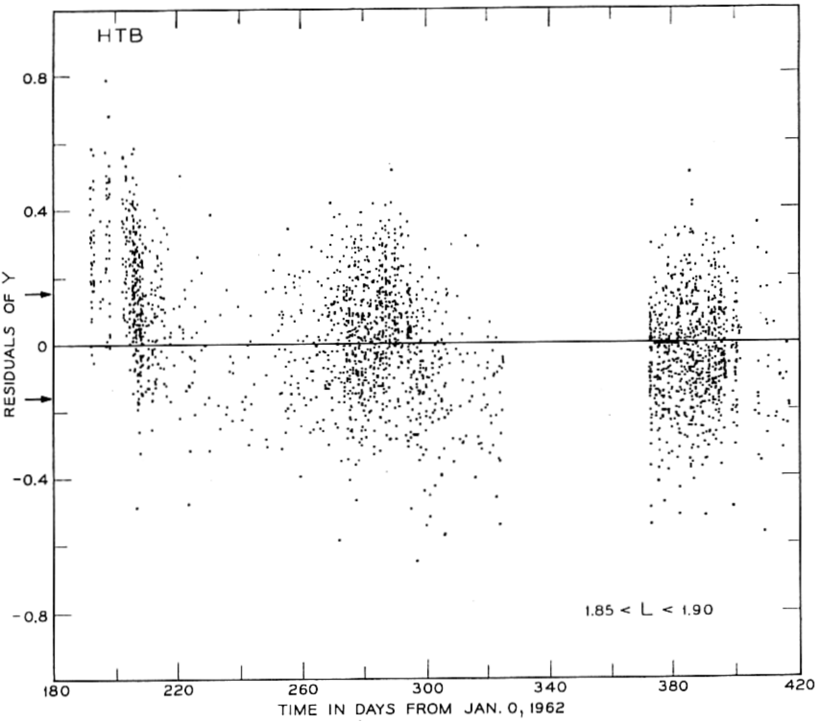

Fig. 40—HTB residuals of Y (i.e., $Y - y$ calculated from the HTB coefficients) plotted against time for $1.85 < L < 1.90$. The arrows indicate ± the approximate standard deviation if Y^2 were Poisson distributed.

is not possible to separate out other variables which may be influencing the results.

From the magnitude of this effect, it is clear that it must be contributing substantially to the MSR. A decrease of ten percent in the average value of Y corresponds to a decrease of about 20 percent in the flux. A fractional change in the flux which is independent of x and L cannot be distinguished from a change in the characteristics of the instrument. Among other possibilities, radiation damage or the decay of protons which might have been associated with the Starfish high-altitude nuclear test of July 9, (day 190) 1962 might have produced the observed effects. Because of this ambiguity, we are unable to offer any well-founded interpretation of the time dependence of the data before day 225. For reasons to be noted shortly, ambiguities are also encountered when interpretation of the temporal behavior of data acquired after day 400 is attempted. In the intermediate period, the time dependence does vary with x and L. By using Fig. 40, which shows comparatively little fluctuation during this intermediate period, as a standard we are able to measure relative changes in the belt. The stretches of sparse data near days 240 and 320 in Fig. 40 are a result of the orbital configuration, there being less opportunity to acquire "high-temperature" data during these periods. The absence of HTB data between day 325 and 373 was caused, as noted in Section 6.9, by the low bias condition that existed during that time. However, an examination of residuals from the CB fit between days 325 and 373 reveals nothing that vitiates the conclusions drawn from the HTB data in what follows.

Residuals versus time-in-days have also been plotted for x,L cells of size 0.1 in L by 0.2 in x. Below $L = 1.9$ we find only one change with time within the sensitivity of our measurements, namely, a secular decrease between days 225 and 400 which occurs only near the ends of the field lines ($x \geqq x_c - 0.2$). We are unable to quantify this effect because, in order to see the droop above the noise, we need to collect residuals from a fairly sizable region of space. The term "sizable" means a region over which y changes so much that an average value of y in the region is not sufficiently representative to be used as a basis for computing a percent change in the flux. Fig. 41 gives an example of an x,L cell near the cutoff where this decrease may be seen. However, in the adjacent lower-x region, Fig. 42, where the ability to discriminate absolute changes in the average value of Y is the same and the ability to discriminate percent change in the average value of Y is much greater

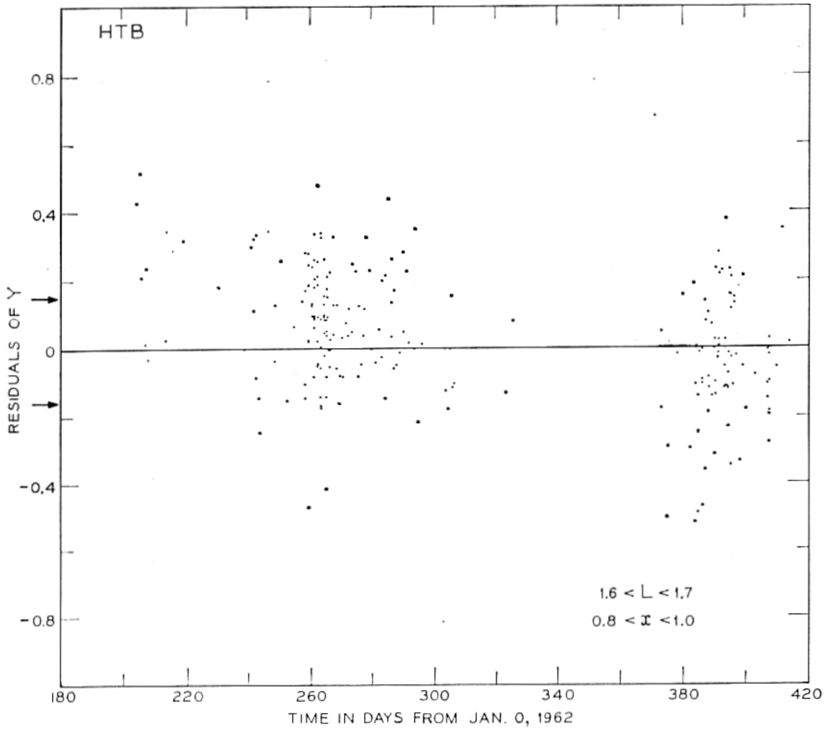

Fig. 41—HTB residuals of Y (i.e., $Y - y$ calculated from the HTB coefficients) plotted against time for $1.6 < L < 1.7$ and $0.8 < x < 1.0$. The arrows indicate ± the approximate standard deviation if Y^2 were Poisson distributed.

than for the region of Fig. 41, no corresponding secular decrease between days 225 and 400 is evident.

The droop in the residuals after day 400, which is noticeable in Fig. 42, is characteristic of many of the plots of residuals versus time-in-days. The widespread occurrence of this effect confuses instrumental and "real" variations and introduces unresolvable ambiguities when attempts are made to identify the source of the droop.

The observation of the general downward slope in Fig. 41 might be explained by a small decrease in x_c, which corresponds to a small increase in the altitude of the cutoff, between August 1962 and January 1963 on L-shells below 1.9.[23] Alternatively, one might be observing the decay of the 55 MeV protons whose perturbation by the Starfish high-altitude nuclear test of July 10, (day 190) 1962 and subsequent behavior have been measured by Filz[24] near the bottom of the trapped proton belt. There are too few data for us to attempt further interpretation of this qualitative observation concerning the secular behavior of x_c. The number of points affected and the magnitude of the shift are too small for this effect to contribute interestingly to the MSR.

10.3 *Short-Term Effect*

The plots of the residuals versus time-in-days, for x,L regions, show a short-term fluctuation which is sufficiently singular to be referred to as an event. This event is an increase in the average value of Y over the 30-day period which starts about day 280. It can be seen clearly in Fig. 43. The increase is discernible only for $L > 1.9$.

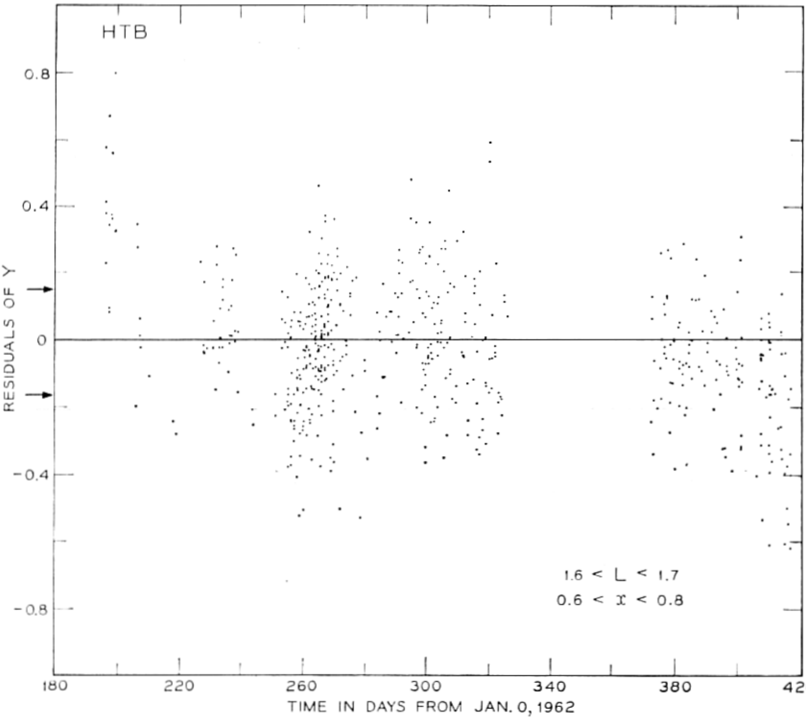

Fig. 42—HTB residuals of Y (i.e., $Y - y$ calculated from the HTB coefficients) plotted against time for $1.6 < L < 1.7$ and $0.6 < x < 0.8$. The arrows indicate ± the approximate standard deviation if Y^2 were Poisson distributed.

TABLE VI—FRACTIONAL INCREASE IN FLUX BETWEEN DAYS 280 AND 310, 1962.

L \ x	0.1	0.3	0.5	0.7	0.9
<1.9	—	—	—	—	—
1.95	0.05	0.07	0.12	0.20	0.70
2.05	—	—	0.37	0.46	0.90
2.15	—	—	0.28	0.33	—

Table VI gives the fractional increase in the average counting rate (Y^2) during this period at various values of x and L. By $L = 2.25$ the change is barely observable and for $L > 2.3$ it has disappeared. The data acquired between days 325 and 373, which are not included among the HTB data because the bias voltage was low, were ex-

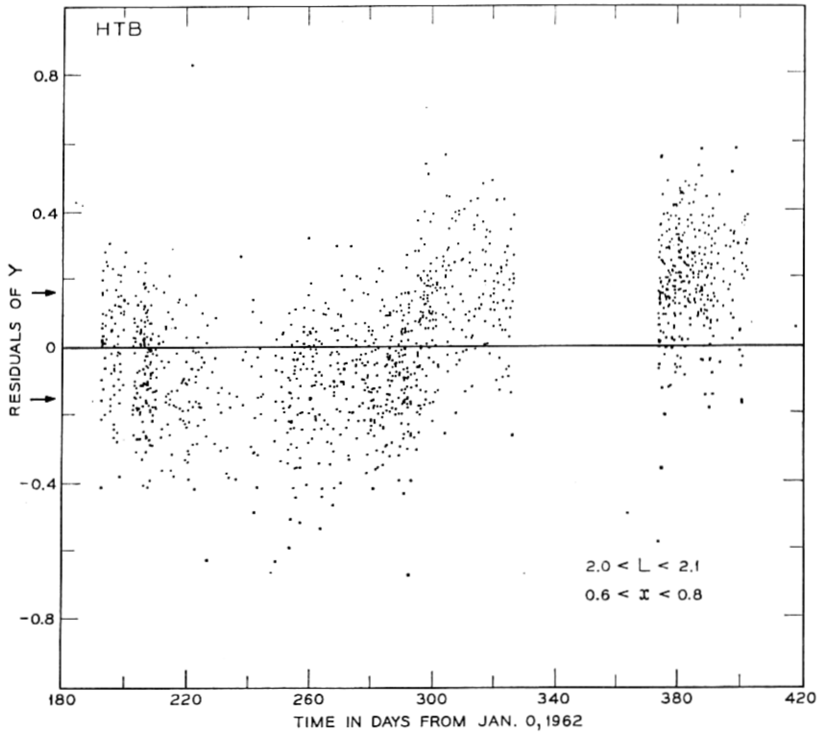

Fig. 43—HTB residuals of Y (i.e., $Y - y$ calculated from the HTB coefficients) plotted against time for $2.0 < L < 2.1$ and $0.6 < x < 0.8$. The arrows indicate ± the approximate standard deviation if Y^2 were Poisson distributed.

amined; and there appears no reason to believe that there were any changes in the intensity of the >50 MeV protons for $L > 1.9$ during these 48 days.

While it is not possible to be quite sure that we are observing a "true" temporal effect, it is difficult to contrive any alternate explanation. This event can be compared with the changes produced in the high energy proton distribution by the magnetic storm of September 22, 1963, and observed with Relay 1[25] and the *Telstar*® 2 satellite.[5] In both cases only L shells with values above 1.9 were affected, and the effect is more pronounced at higher x's. However, the storm produced a decrease in flux whereas an increase was observed in 1962; the effects of the storm were more severe at larger L's, whereas in this event, a maximum fractional change was observed near $L = 2.05$; and the effect of the storm was sudden, i.e., the flux decrease took place within 24 hours, while the increase observed in 1962 was gradual and required a month to complete. Increases in flux having some of the features described here were observed with Explorer 7.[26] However, it is difficult to be certain that those increases were caused by protons with energies above 18 MeV, rather than electrons with energies greater than 1.1 MeV.

The high-energy protons appear very stable over the seven months covered by our data. In particular, no effects associated with the USSR high-altitude nuclear tests of October 22, October 28, and November 1, 1962, or the large magnetic storm of December 18, 1962 have been observed.

In summary, changes through time in the observed values of the flux are generally less than 20 percent, although they may be larger in some regions of space. We have not been able to detect a diurnal effect. Often, secular changes are not separable from other variables, an exception being an apparent change in the position of the cutoff. An event which appears to comprise a measurable redistribution of the proton flux over an appreciable volume of space and period of time has been noted. We do not know whether the redistribution is in energy or space, and find no indication of the mechanism in the data.

XI. THE CUTOFF

As discussed in Sections V, 6.3, and 7.5, the cutoff function, $x_c(L)$, is defined in terms of our instrument, model and fitting procedure. For $L < 2$, the value of $x_c(L)$ corresponds to the position on the given L

shell at which the omnidirectional flux is of the order of 1 proton/cm^2 sec, more than three orders of magnitude below the highest flux in the belt. However, because the flux is falling so fast with x, this position is almost certainly very close to the place at which the flux becomes 0. The last statement is not true for $L > 2$. Here, although the value of $x_c(L)$ (the place at which $y = 0$) still corresponds to the point at which the limit of sensitivity of our instrument is reached, the position of x_c is not so well-defined by the fit. In addition, one has only to examine Fig. 23 to realize that x_c may be significantly removed from the value of x at which the flux falls to zero.

The Model-I HTB coefficients of Table IV define the cutoff function, and we have made use of a modification of R. H. Pennington's mirror trace program* to calculate the minimum altitude corresponding to $x_c(L)$ for $L < 2.2$. This inversion was accomplished using the Jensen and Cain magnitude field coefficients for 1960,[13] the same set used to calculate x and L (see Table I). (Other sets of coefficients are available.[27] However, using the GSFC (7/65) coefficients[28] does not produce significantly different altitudes.)

The minimum altitude is smallest in the Southern Hemisphere over the Atlantic Ocean. Fig. 44 shows the results in graphical form. The minimum altitude is $\approx$270 km near the equator ($L = L_0 \approx 1.13$), decreases to a minimum of $\approx$160 km at $L = 1.6$, and increases very rapidly thereafter. For L less than 1.5, the standard error in altitude, derived from the standard error in x_c (see Fig. 22), is about 10 km, which is roughly the accuracy of the inversion procedure as we used it. The standard error in altitude for $L > 1.5$ is indicated by the dashed lines in Fig. 44. At $L = 2$, where the cutoff mechanism is only partially atmospheric, the standard error is nearly 50 km.

The minimum near $L = 1.6$ in the altitude curve of Fig. 44 appears to reflect the existence of the South American magnetic anomaly. Although $R_c(L)$ [see (5)] increases monotonically with L for $L > 1$, the increase is apparently not fast enough to override the influence of the anomaly. This result is true for all the sets of coefficients produced in many trial fits as well as for the HTB coefficients in Table IV. We have not yet carried out the obvious next step of averaging the atmospheric density over the orbital path of the protons to see whether or not the shape of Fig. 44 can be explained on the basis of present models of the atmosphere.

Although the shape of the minimum altitude curve remains the

---

* Kindly communicated to us by D. J. Williams.

same, the value of the altitude is sensitive to the method of selecting the sample (see Section 7.1). For example, the minimum value of altitude calculated from the CB coefficients is 100 km (again at $L = 1.6$), 60 km lower than the 160 km calculated from the HTB coefficients. The weighting of the HTB sample emphasizes the high x data and gives better representation, and therefore a better expectation of fitting well, near the cutoff. However, the *Telstar*® 1 satellite, with its eccentric orbit and relatively high (950 km) perigee, could not give detailed information about particles near the top of the atmosphere, and this is reflected in the results of the analysis.

In conclusion, the curve of Fig. 44 probably represents the quali-

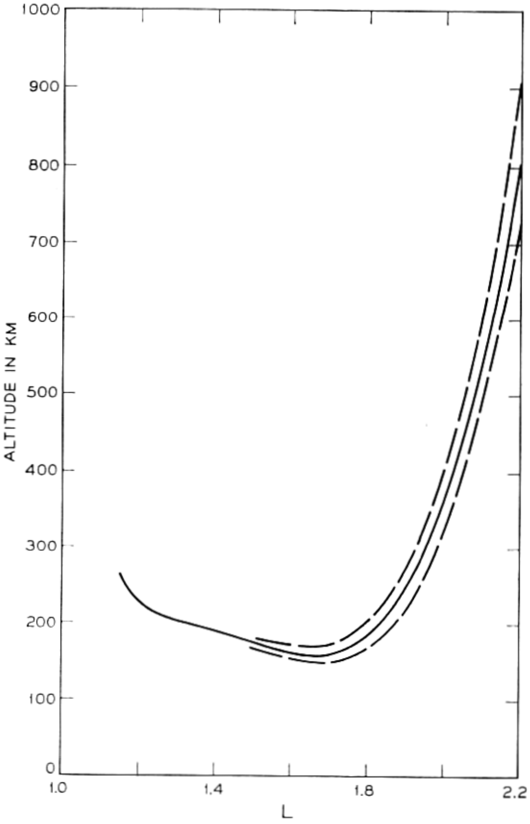

Fig. 44—The minimum altitude reached by > 50 MeV protons as a function of L. This altitude is determined in geographic coordinates from the transform of $x_c(L)$. The dashed curves are ± one standard error.

tative behavior of the minimum altitude of the cutoff reasonably well, but the uncertainty in the value of the altitude is larger than a simple examination of the standard error plotted in the figure would lead one to believe. The implications of these results for the details of the cutoff mechanism have not been examined in detail; however, it is clear from the sudden upturn of the curve in Fig. 44 that the mechanism is principally atmospheric for L less than about 1.9 and principally nonatmospheric on higher L shells.

XII. COMPARISON WITH OTHER WORK

12.1 *Introduction*

When making comparisons among the various high-energy proton measurements it is desirable that the results be extensive in time and space, reported in terms of omnidirectional fluxes at various positions, and that these positions be expressed in magnetic coordinates derivable from the B,L set. A list of some experiments which meet these desiderata is given in Table VII.

Following a presentation of flux maps, comparisons among these experiments are made with respect to the following features: the absolute intensity at one point in the belt, as close to the maximum of intensity as is practical; the intensity vs L in the equatorial plane; the behavior of the intensity on selected L shells; the flux near the top of the atmosphere, and the equatorial pitch angle distribution. Comparisons covering a larger range of proton energies have also been made by Vette[29] and Fillius.[20]

One of the difficulties encountered in making comparisons among the various bodies of data is that most of the results have been published in graphical form, rendering it necessary to scale numerical values from small plots, an inaccurate procedure at best. A welcome exception is the Explorer 15 data, which McIlwain[18] has made available by means of a series of interpolation functions in the form of a FORTRAN computer program.

12.2 *Telstar® 1 Flux Maps*

For this discussion, the *Telstar®* 1 HTB results have been converted to omnidirectional flux, J, where $J = 4\pi y^2/\bar{g}$. (Note that the value of $\bar{g}$ derives from the assumptions of Appendix A regarding the energy spectrum.) This procedure provides an estimate of the flux of protons with energies between 50 and 130 MeV at positions, (x, L), in mag-

TABLE VII—SOME SATELLITE MEASUREMENTS OF THE HIGH-ENERGY TRAPPED PROTONS.

Satellite	Approx. period covered in reference	Orbit perigee, R_e apogee, R_e incl, deg	Instrument	Approx. energy range	References
Explorer 4 1958 $\epsilon 1$	7/26/58 to *	1.041 1.347 50	Anton 302 Geiger tube (shielded)	> 43 MeV	9 30
Injun 1 1961 $o2$	7/61 to 12/61	1.14 1.16 67	Anton 213 Geiger tube (shielded, SpB)	> 40 MeV	31.
1961 $\alpha\delta 1$ (H2)	10/21/61 to **	1.59 1.55 96	scintillator	> 59 MeV	32.
1962 $\kappa 1$ (H3)	4/9/62 to **	1.54 1.44 87	scintillator	> 59 MeV	32.
Telstar® *1* 1962 $\alpha\epsilon 1$	7/10/62 to 2/21/63	1.15 1.90 45	solid-state detector	50–130 MeV	
Explorer 15 1962 $\beta\lambda 1$	10/27/62 to 1/27/63	1.049 3.72 18	scintillator	40–110 MeV	18
Relay 1 1962 $\beta\nu 1$	5/1/64 to 9/22/64	1.21 2.14 48	scintillator	> 35 MeV	33.
Injun 3 1962 $\beta\tau 2$	12/24/62 to 9/28/63	1.037 1.44 70	scintillator	40–110 MeV	19

* Not stated. Re-entered atmosphere 10/23/59.
** Not stated.

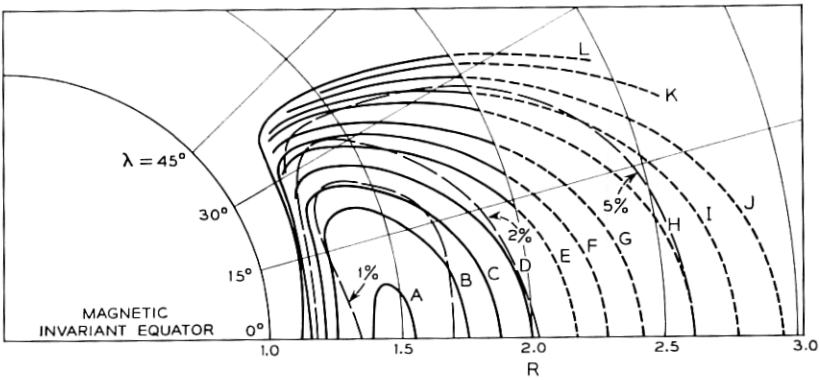

Fig. 45 — Omnidirectional isoflux contours derived from the HTB coefficients and plotted in R,λ space. Dashes indicate extrapolation beyond the region in which data were acquired. Long dashes form contours of constant percent standard deviation.

Label	A	B	C	D	E	....	L
Omnidirectional flux (J)	5×10^3	2×10^3	1×10^3	5×10^2	2×10^2		1×10^0 protons/cm^2 sec

netic space on the basis of the presently provided model and fit to the HTB data.

For ease of reference, *Telstar*® 1 HTB flux maps are presented in three commonly used forms: Fig. 45 shows contours of constant flux in R,λ coordinates; Fig. 46, contours of constant flux in B,L coordinates; and Fig. 47, log flux vs log B curves for various values of L. These three graphs give an overall picture of the particle distribution. In these figures, dashed lines are used to indicate the extrapolation of fitted values to regions not penetrated by the satellite. Note the way the geometry of the coordinate transformations affects the extrapolated regions. In particular, the functional extrapolation in B,L coordinates gives much more curvature to the contours than might be anticipated. The difference between the functional and straight line extrapolation in B,L can be as large as a factor of 2 in the flux (a shift of 0.2 in L) at $L = 3$. Except for the region of the secondary local maximum in the flux near $L = 2.2$, this functional extrapolation compares surprisingly well with the measurements made on higher altitude satellites.[5, 18]

In the altitude range covered by the data, a single maximum is observed. This maximum in the omnidirectional flux of $\approx 6 \times 10^3$ protons/cm^2 sec is located on the magnetic equator at $R = L = 1.46$.

The intensity falls abruptly near the bottom of the belt (the top of the atmosphere) and decreases more gradually toward the sides and top of the belt. On a given L shell, the intensity is a maximum at the magnetic equator, and deceases monotonically as the distance from the equator increases.

Neglecting the uncertainties in the calibration of the instrument (−25 to +50 percent), which are discussed in Appendix A and are mentioned in the next subsection, the estimated standard deviation of the estimate of J is less than 2 percent of J over much of the region of space discussed in this section. Smoothed contours of 1 percent, 2 percent and 5 percent standard error are plotted as the dotted lines in Fig. 45. Near the cutoff, where the counting rate is falling to zero, the standard deviation in x_c (see Figs. 44 and 22) is a useful indication of uncertainty in the flux. Other information concerning

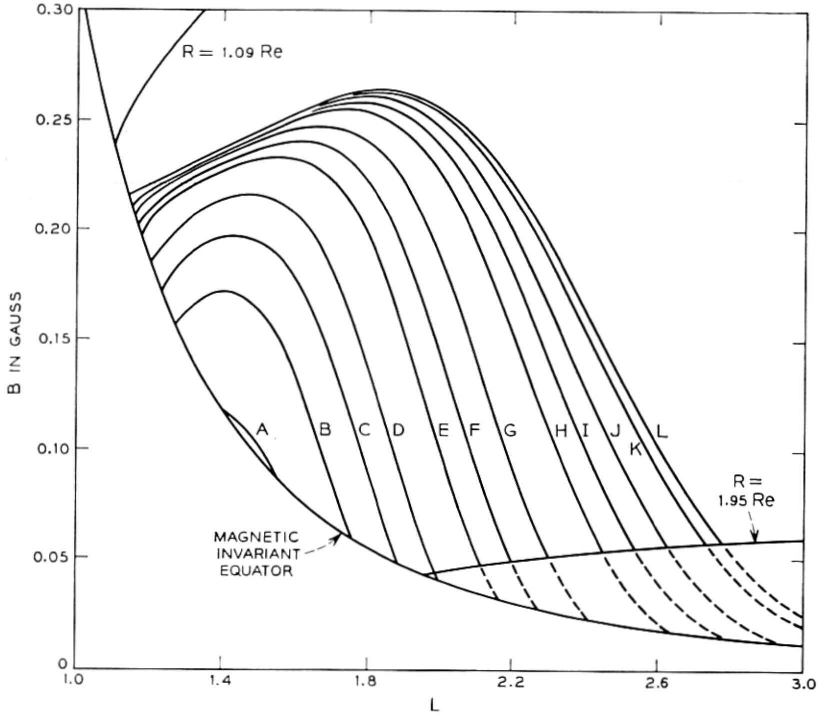

Fig. 46 — Omnidirectional isoflux contours derived from the HTB coefficients and plotted in B,L space. Dashes indicate extrapolation beyond the region in which data were acquired. Labeling is given in Fig. 45.

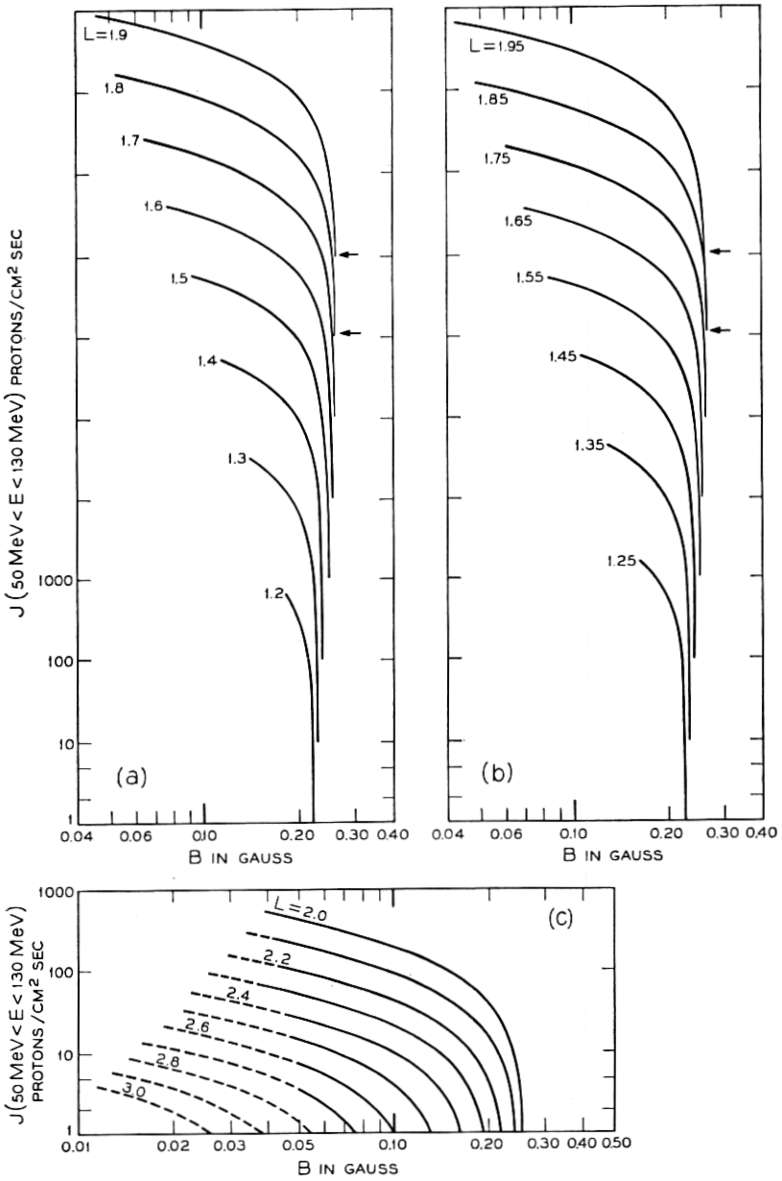

Fig. 47 — Omnidirectional flux on several *L*-shells derived from the HTB coefficients and plotted against log B. Adjacent curves in parts (a) and (b) are slipped one decade in *J*. All curves rise from $J = 1$ proton/cm² sec. Dashes indicate extrapolation beyond the region in which data were acquired.

standard deviations may be found in Sections 7.4 to 7.6 and 8.4, Figs. 22, 23(a), 23(c), and 24.

The equations defining Model II (see Section 4.6) and coefficients of Table V, together with the transformation equations among various magnetic coordinate systems, allow accurate relative flux values to be easily calculated in any coordinate system.

12.3 *Comparison of Absolute Intensities*

The solid curve in Fig. 48 is the fitted omnidirectional equatorial flux of 50–130 MeV protons measured by the *Telstar®* 1 satellite. The points are fluxes observed on other satellites (Table VII) at the mag-

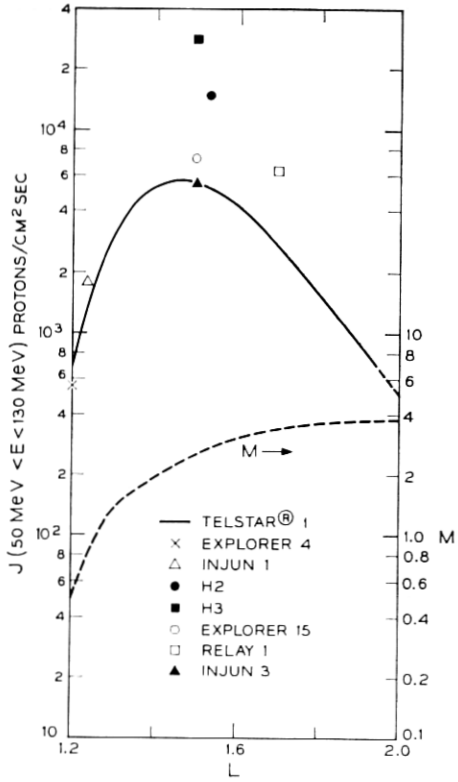

Fig. 48 — Values of equatorial omnidirectional flux, for the satellites indicated in the legend, corrected to the energy range 50–130 MeV and plotted at the appropriate value of L. An integral power-law energy spectrum [see (17)] of exponent $-M$, where M is given is a function of L by the dashed curve, was used in making the corrections. References are given in Table VII.

netic equator and corrected to 50–130 MeV by using a single-component integral energy spectrum of the form

$$N(>E) \propto E^{-M} . \tag{17}$$

The values of M at the magnetic equator are plotted as the dashed line in Fig. 48. These values were taken from Gabbe and Brown,[5] and are consistent with those of Brown, Gabbe, and Rosenzweig,[3] and also those of Fillius and McIlwain,[34] and Freden et al,[35] where the data overlap. Because of uncertainties in the geometric factors of the detectors (see Appendix A) and changes in the belt with time (see Section X), one might expect agreement only within a factor of about 2. On this basis the agreement in absolute intensity is quite reason-

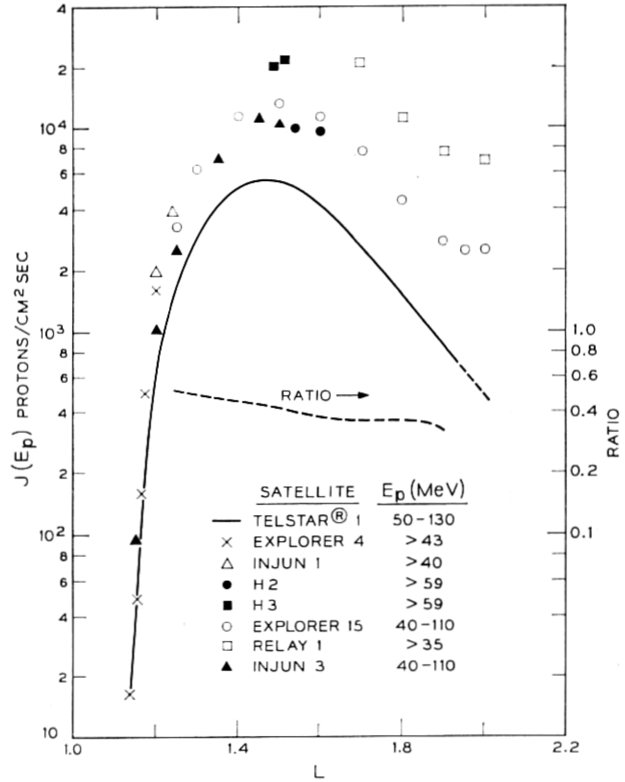

Fig. 49 — Values of equatorial omnidirectional flux, for the satellites and energy ranges indicated in the legend, plotted against L. The dashed curve is the ratio of *Telstar*® 1 to Explorer 15 measurements. References are given in Table VII.

able. However, the *Telstar*® measurements are somewhat on the low side, and those of Imhof and Smith[32] (H_2 and H_3 on Fig. 48) are much higher than the other observations.

The points represent measurements taken before, after, and during the *Telstar*® 1 experiment so it is unlikely that changes in the flux with time explain these differences. It is difficult to account for the discrepancies in absolute flux in terms of the spectral correction, unless more complex spectral forms than those of Appendix A are considered, because the comparisons are among results of detectors whose threshold energies are close to 50 MeV. The most likely sources of the differences are errors in absolute calibration. It follows that a good deal of caution should be exercised in drawing conclusions about temporal effects and energy spectra from measurements made with *different* instruments.

12.4 *Intensity vs L in the Equatorial Plane*

Fig. 49 is a plot of the omnidirectional equatorial flux for each of the satellites listed in the legend of the figure. The data are from detectors having several different energy ranges and no spectral corrections have been made. The general features of the data in these energy ranges have been noted previously in the literature. The flux increases rapidly with L, goes through a maximum near $L = 1.5$ and then decreases. The decrease is not as rapid as the initial rise and in this energy range the flux generally does not decrease monotonically[18, 20] for $L > 2$. Excepting the measurements of Imhof and Smith,[32] the flux decreases with increasing energy, indicating a falling energy spectrum.

The dashed line in Fig. 49 is the ratio of the 50–130 MeV proton flux measured with *Telstar*® 1 to the 40–110 MeV proton flux measured with Explorer 15. This ratio is a good qualitative index of the energy spectrum near 45 MeV, and in these circumstances the change in this index is independent of the absolute calibrations of the instruments. The ratio is seen to decrease monotonically as L goes from 1.25 to 1.9, indicating, in agreement with the references cited in the previous subsection, a softer spectrum* at higher L.

12.5 *Intensity vs B on L Shells*

In Fig. 50 [parts (a), (b), and (c)] measurements from various satellites are compared on the three L shells, 1.3, 1.5, and 1.8. The

---

* A softer spectrum contains a larger fraction of low-energy particles.

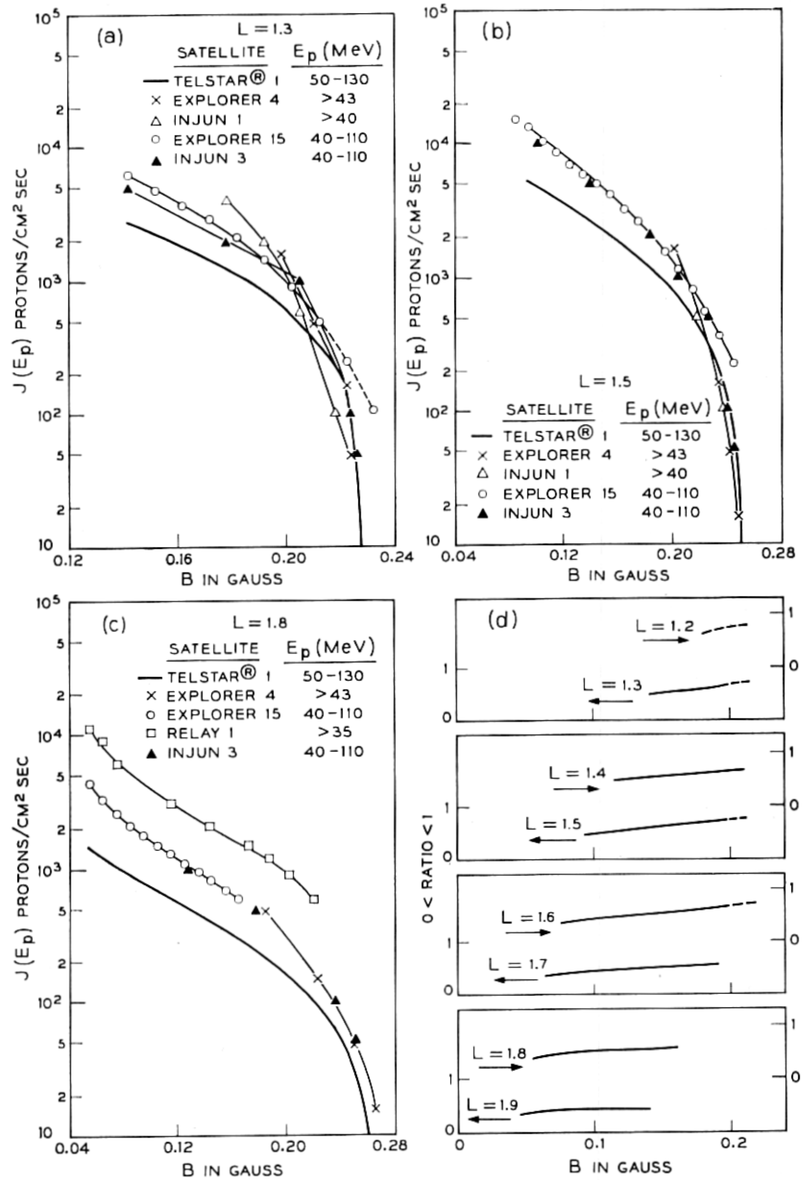

Fig. 50 — Values of omnidirectional flux on various specified L-shells, for the satellites and energy ranges indicated in the legend, are plotted vs B, in parts (a), (b), and (c). Ratios of *Telstar*® 1 to Explorer 15 measurements are shown in part (d). References are given in Table VII.

Explorer 15 and Injun 3 measurements have been compared in more detail by Valerio.[19] Observe that J decreases monotonically with B on all the L shells and the shape of J vs B is very similar for all the measurements on the same shell except for the lowest L shell where the dependence on the energy response of the detector is most important. Information concerning the energy spectrum near 45 MeV is contained in the changes in the ratios of the measurements, and in these circumstances the changes are independent of the absolute calibrations of the instrument.

To cast more light on the qualitative behavior of the energy spectrum, the ratio of the 50–130 MeV proton flux measured with the *Telstar*® 1 satellite to the 40–110 MeV proton flux measured with Explorer 15 has been calculated as a function of B for fixed L. The results are plotted in Fig. 50(d). All the ratios increase with increasing B for L from 1.2 to 1.9 inclusive. The values of B in the plot cover the range from the magnetic equator to a magnetic dipole latitude (λ) of about 30°. The increase in the ratio indicates a spectrum that hardens with increasing B in the neighborhood of 45 MeV. At $L = 1.8$ Freden et al[35] find a spectrum that hardens with increasing B for proton energies between 10 and 35 MeV, but softens with increasing B for proton energies above about 55 MeV. Our results suggest that this change in behavior cannot have occurred below 50 MeV.

12.6 *The Intensity Near the Top of the Atmsophere*

The position of the 8-protons/cm^2 sec flux contour from the *Telstar*® 1 satellite is plotted in B,L coordinates in Fig. 51 (a), together with our own extrapolation of the published Injun 3 data[19] to a flux of about 10 protons/cm^2 sec,* and the 16-proton/cm^2 sec flux contour from Explorer 4. The purpose of this figure is to test whether or not the altitude dependence of contours of constant counting rate at low altitudes is consistent with other data. The qualitative agreement of the results plotted in Fig. 51(a) is quite good, especially for $L < 1.8$, where the atmosphere is controlling. A number of effects may contribute to the divergence of the results for $L > 1.8$. Among them are: temporal effects, this region of the belt is shown to be subject to temporal variations in Section X; instrumental effects, the instruments are near their threshold sensitivities in a region of magnetic space in which the energy spectrum may be anomalous; and biases in the fitting procedure,

---

* Valerio[19] states that his fits (and therefore his Fig. 8) are not intended to represent the data accurately at low altitude.

examination of residuals give some indication of a slight bias in the fitted function in this region.

It is difficult to get direct insight into the altitude dependence from a B,L plot, so the values of B have been transformed into mini-

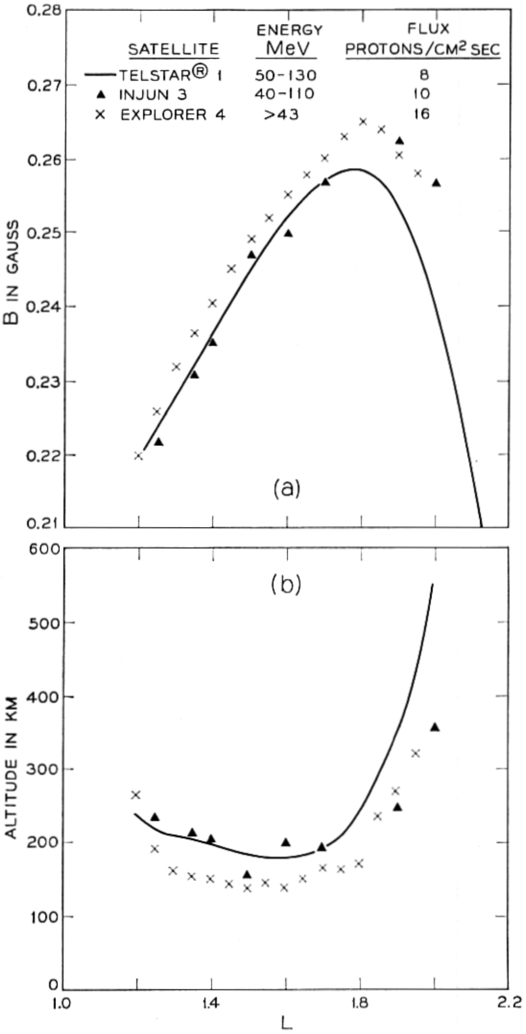

Fig. 51 — Comparison of isoflux contours obtained from three satellites near the top of the atmosphere. Part (a) B, L coordinates, part (b) minimum altitude (near the South American magnetic anomoly). References are given in Table VII.

mum altitude by using the procedure mentioned in Section XI. The minimum altitudes are plotted against L in Fig. 51(b). It is characteristic of all three bodies of data that the minimum in the minimum altitude curve does not occur at minimum L.

It is tempting to consider whether the lower altitude of the Explorer 4 points, coupled with the lower low-energy threshold and high flux associated with the Explorer 4 measurements, might imply that the exosphere was less dense when the Explorer 4 measurements were made. However, the uncertainty in the position of the *Telstar*® contour (see Section XI) is so large that the use of this figure to refute the hypothesis that the atmosphere contracted[23] between 1958 ($\approx$ solar maximum), when the Explorer 4 measurements were made, and 1962, when the *Telstar*® data were taken is precluded, even if one were prepared to overlook the possibility that the energy spectrum at these low altitudes is anomalous[36] and consequently that the calculated geometric factors of the instruments may be in substantial error near the cutoff.

12.7 *Equatorial Pitch Angle Distribution*

The solid curves in Fig. 52(a) represent the equatorial pitch angle distributions, at various values of L, calculated from (8) and the coefficients in Table V. When these are compared with the equatorial pitch angle distributions obtained from the Injun 3 data,[19] which have been replotted as the dashed curves in Fig. 52(a), they are found to be very similar in shape, although the *Telstar*® curves are a trifle flatter. This would be anticipated from the previous discussion of the tendency of the energy spectrum of protons with energies near 45 MeV to harden at high values of B. The shape of the distributions are, however, appreciably different from those derived by Lenchek and Singer[37] from consideration of possible injection and loss mechanisms. This may be seen in Fig. 52(b) which contains the present results as the solid lines, and the results of Lenchek and Singer[37] as the dashed lines.

12.8 *Other Bodies of Data*

A portion of the considerable body of relevent high-energy proton data, some of which does not meet the requirements for inclusion in Table VII, is noted here. The earliest measurements of proton intensities were made on Explorers 1 and 3 by Van Allen.[38] His historic estimate of $\approx 2 \times 10^4$ protons/cm^2 sec with energies >40 MeV at the heart of the inner belt ($x = 0$, $L \approx 1.56$) has been substantiated by all the measurements reported to date. In particular, the high-energy proton

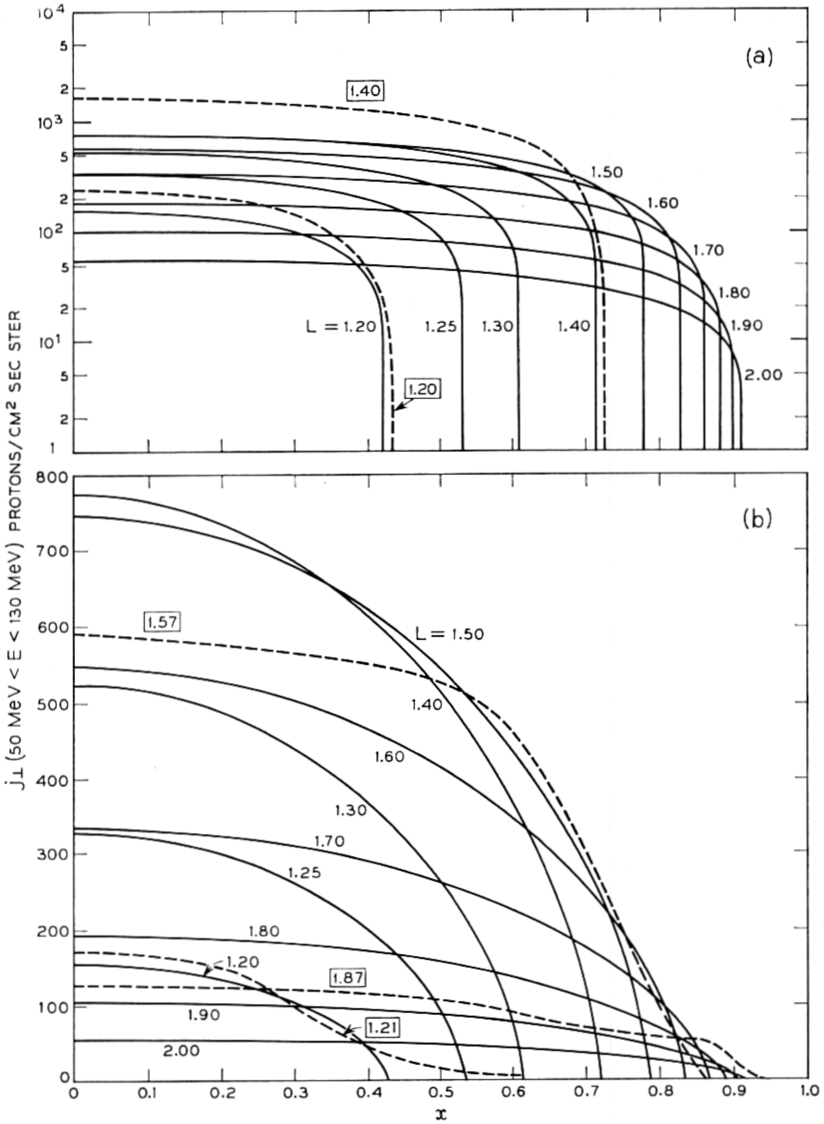

Fig. 52 — Unidirectional flux vs x on various L-shells. The solid curves are derived from the HTB coefficients using (8). The dashed curves in part (a) are Injun 3 results (from Valerio[19] Fig. 8). The dashed curves in part (b) are the results of the theoretical calculations of Lenchek and Singer,[37] taken from their Fig. 10 and arbitrarily normalized to reasonable values of j at $x = 0$.

measurements made in the inner belt by Explorers 6, 12, and 14 and Pioneers 3 and 4, have been noted by Frank et al[39] to agree with each other and with those on Explorers 1 and 3. Reference to some measurements made with ballistic probes may be found in the article by Freden et al.[35]

XIII. QUO VADIS

The mathematical model which has evolved along the lines summarized in Section IV has provided a very satisfactory representation of the high-energy proton data from the *Telstar*® 1 satellite, as discussed in both statistical and physical terms in Sections VI through XII. It is appropriate to consider how this work might be extended.

13.1 *Further Improvements within the Present Scheme*

The final fit of Model II has a mean square error which is less than twice the variance to be expected on the assumption of a Poisson distribution of the count data. Some of this excess is surely due to "experimental error." However, one might seek some additional improvement by the addition of more parameters to the fitting function as indicated in Model III of Section 4.7. Such fits, carried out on an approximately 1000-point selected data set, will almost surely lead to a reduction in the mean square residuals because of the increased freedom the additional parameters provide. However, as noted in Section 4.7, preliminary work with Model III has not led to a really substantial improvement, either statistically or aesthetically as judged by plots of the residuals.

Additionally, one might try to improve further on the representativeness of the sample by simple iteration. Using the HTB fit to Model II to determine new x,L cells, another sample might be selected and fitted. The very small differences between the Model-I CB fit and the Model-I (or II) HTB fit do not suggest that this would be fruitful in the present case. If the preliminary fit used for determining the x boundaries of the cells were a poorer fit, iteration would clearly be worthwhile.

A further extension of the procedure for designating representative cells would involve the development of a two-dimensional version of the basic idea and procedure outlined in Section 7.1. Specifically, one would try to define approximately 1000 x,L cells within each of which the preliminary fit to $y(x, L)$ has the same range. In the present case, the anticipated gain from this refinement did not seem to justify the practical difficulties. However, a practical, well-defined algorithm for such a process in several dimensions simultaneously might prove very useful.

13.2 *Another Approach to the Model*

All the models presented so far are of the form

$$y(x,\, L) = A(L) \cdot b(x;\, e_i(L)), \tag{18}$$

where $A(L)$ represents the variation in intensity along the magnetic equator and $b(x;\, e_i(L))$ represents the variation with x on an L-shell. The $\{e_i(L)\}$ adjust the nature of the dependence on x, as a function of L. This approach arises from the L-shell orientation of the adiabatic theory of trapped particle motion.

Alternatively, one might focus attention on the shape of y as a function of L at constant x, rather than on y as a function of x at constant L. It is shown in Fig. 19(a) and discussed in Section 7.2 that $y(x,\, L)$ as a function of L for fixed x forms a simple nesting set of curves at successive values of x. This is a consequence of the monotonic decrease of y with x at any fixed L. With this orientation, a model might be expressed as:

$$y(x,\, L) = F(L;\, p_i(x)), \tag{19}$$

where $F(L)$ is the shape of a constant-x section, whose parameters, the $\{p_i\}$, are expressed as functions of x. Although this approach would not contain the L-shell orientation of the particle motion explicitly, it seems to offer very significant practical possibilities.

13.3 *Full Data Utilization*

In the two-dimensional fits that were carried out, only a selected set of data were used, either chosen at random within a set of narrow, contiguous L-slices, as in the fit of Section VI, or chosen on the basis of a preliminary fit to the data as in Section VII. All the data were examined by residual plots and mean square residual measures of the fits, but only a small part of the data were actually used in determining the values of the fitting parameters. With this procedure, information is clearly being lost that could be used to "better" determine the function.

Several methods have been applied in the past to allow all of an existing body of satellite data to influence the mathematical description of that data. The most direct method uses interpolation or smoothing functions. It is often the case that consecutive satellite observations from a particular detector are closely enough spaced to determine the local spatial variation. Under these conditions a sequence of data points can be averaged or fitted to a local smoothing function. A number of points in a sequence may thus be replaced and represented by a single point which is determined by them all. The replacement may also be made at some particularly convenient coordinate location, for example, at one of a fixed set of L or x values on which functional fitting may subsequently be carried out. This method has been used on the data of Explorer 15, portions of which have been described by McIlwain,[18] Roberts[40] and Brown.[41]

In the context of the high-energy proton data from the *Telstar*® 1 satellite, a different but analogous procedure could be used. Rather than selecting at random one data point within each of approximately 1000 x,L cells, all points within a given cell could be used to determine a value which would represent the observable at the central point of the cell. This might be done by simply averaging the points within the cell, but the cell size is large enough so that the x and L dependence within the cell generally cannot be neglected. A more representative procedure would be to fit the points within an x,L cell with a local smoothing function. This function can be the same function with which the finally selected data values would be fitted across the complete range of x,L space (see Appendix B.7). Although in the present case the average number of points per cell is about 40, in many cells the number of points is fewer than the number of coefficients of the Model II function, and some coefficient constraint would be required. This is not a substantial objection, however, since the function is only being used for smoothing and does not need to be capable of elaborate variation over an x,L cell.

A procedure of this kind greatly reduces the chance that members of a final 1000-point set will be nonrepresentative and acknowledges the experimental weight of adjacent observations in fixing the values of the set. Accordingly, one would expect a reduction in the mean square residuals overall the data, from a fit to such a smoothed sample.

The procedure of smoothing within a cell could be used with larger x, L cells (with more points per cell) to define a point set smaller than 1000. It can of course also be used with much larger bodies of data up to a maximum of 1000 points per cell with the existing computer program.

13.4 *Extension to Other Cases*

There are very evident values in being able to communicate the essence of a large body of data in terms of a mathematical model with a small number of coefficients. This is very effectively accomplished by the present empirical representation of the *Telstar*® 1 high-energy protons, but the model is very specialized. As previously noted, including a wider range of space such as that explored by the *Telstar*® 2 satellite requires modification of the function. Characterizing the proton distribution for substantially lower energy protons may well require functions outside the generality of even Model III. Treating electrons in almost any region of space requires treating time as well as position variables because a complete set of measurements of the spatial distribution of the particles cannot readily be obtained in a time short compared with significant time variations.

No single formulation yet exists which is capable of coping in a useful way with the range of measurements of particles trapped in the magnetic field of the earth. However, the success of the present formulation as it has been evolved and the general methods that have been developed gives us confidence that other and more complicated cases can be treated.

XIV. SUMMARY AND CONCLUSIONS

This section provides a summary, with references, for the entire document including the appendices.

14.1 *General Accomplishment*

The main accomplishment is the development of a relatively simple (empirical) mathematical model which gives a statistically accurate representation of the spatial distribution of high-energy protons measured with the *Telstar*® 1 satellite.

14.2 *The Data*

14.2.1 *Space and Time Coverage* (Sections I and II)

The data were acquired between July 1962 and February 1963 within the region of space bounded by $1.09\, R_e \leqq R \leqq 1.95\, R_e$ and $0 \leqq \lambda \leqq 58°$. Inside these boundaries good temporal and spatial coverage were achieved.

14.2.2 *Energy Range and Instrumental Sensitivity* (Appendix A)

The nominal energy interval of the detector is $50 < E < 130$ MeV and its nominal geometric factor is $0.143^{+0.071}_{-0.036}$ cm^2 ster. The instrument is effectively omnidirectional and the lower threshold of sensitivity is ≈ 1 proton/cm^2 sec.

14.2.3 *Telemetry* (Section II)

Each observation consisted of the number of counts registered in 11 seconds. With this was associated the time at which the telemetry was received, and auxilliary information.

14.3 *The Models*

14.3.1 *Coordinate System* (Section III)

Each model relates the omnidirectional intensity of high-energy protons to a two-dimensional magnetic space whose coordinates, x,L, derive from a mapping of the earth's main magnetic field onto an axially symmetric dipole field through the adiabatic invariants of the particle motion.

14.3.2 *General Form and Properties* (Section IV)

The models have the form of a product, $A(L) \cdot G(x,L)$, in which the first term expresses the equatorial intensity as a function of L, and the second term describes the diminishment of intensity, as a function of increasing x, for fixed L. The functional expressions for G (excluding G''') transform in closed form to equivalent pitch angle distributions.

14.3.3 *Specializations* (Sections IV and IX)

Retrospectively, all the models may be considered to be specializations of Model III, but historically the two-dimensional models evolved from a series of one-dimensional fits on L-slices. These fits led to the L-slice model which was then generalized empirically to the two-dimensional Model I. Model I was in turn specialized to Model II to overcome some statistical (nonlinearities and high correlations) and interpretive difficulties encountered with Model I.

14.4 *Fitting*

14.4.1 *Criterion* (Section III and Appendix B)

The least squares criterion was used in deriving estimates of the 8 (or 9 or 10) coefficients required by the models to fit the data.

14.4.2 *Scale* (Section III and Appendix B)

To stabilize the variance of the observations, the models have been fitted to the square root of the observed counting rate.

14.4.3 *Sampling* (Sections 6.1, 6.9, 7.1 and Appendix B.3)

Coefficients of Models I and II were estimated by fitting samples containing about 1000 of the nearly 80,000 available observations. Sampling is necessary to avoid exaggerating the importance of regions of x,L space where data are abundant, and also for compatability with existing computer programs. A method of sample selection based on a preliminary fit has been developed to provide a good overall representation of the data. Before selecting the sample, the data were partitioned to remove instrumental effects and outliers identified by studying residuals from preliminary fits.

14.5 *Quality of Fit*

14.5.1 *Criteria of Judgment* (Sections VI to IX and Appendices B and C)

Judgments regarding the quality of fit were largely based on graphical studies of residuals, the behavior of the fit at the boundaries of the radiation belt and various statistical measures. Residuals (equal to observed minus fitted), on the square root scale, were particularly useful as sensitive indicators of the quality and nature of the fit.

14.5.2 *Comparisons Among Models* (Sections V and IX)

The L-slice fits give good one-dimensional representations of very limited regions of data. Both the standard errors of the coefficients and the correlations among coefficients are high compared to the corresponding measures derived from the two-dimensional fits. The fits of Models I and II to the 960-point HTB sample are practically equivalent. However, Model II is superior in the following respects: one less coefficient is required, standard errors are uniformly smaller, correlations among the coefficients are uniformly smaller, the index of nonlinearity is very much smaller, and more of its coefficients have a physical meaning.

14.5.3 *Coordinates* (Sections VI and VII)

Plots of residuals vs x, L, time, etc. indicate the general adequacy of x,L coordinates for the organization of the data.

14.5.4 *Quantitative Measures* (Sections VII, VIII, IX, and Appendices B and C)

Typically, the fits account for nearly 99 percent of the variability about the data mean. The mean square error of fit is about $1\frac{1}{2}$ times as large as would be anticipated on the basis of assumed Poisson statistics. Even in the worst of quite small spatial regions, the mean square residual does not exceed $2\frac{1}{2}$ times the Poisson-based prediction. Probability plotting procedures indicate that the residuals are closely normally distributed and lead to an estimate of the variance which is about twice the Poisson-based prediction.

14.5.5 *General Limitations* (Appendix C)

Statistical examination of all the data, categorized in x,L cells defined from a preliminary fit, indicates that it is unlikely that the fit given by the present model could be significantly improved by any simple modification based on x,L coordinates alone.

14.6 *Numerical Values of Fitted Coefficients, Standard Errors, etc.*

14.6.1 *L-Slices* (Section V)

Coefficient values and other statistics for four L-slices appear in Table II, and values of coefficients for a large number of L-slices are shown in Figs. 8 to 10.

14.6.2 *Models I and II* (Sections VI to IX, also Sections V, XI, and XII)

Model II is the preferred model. Coefficients, standard errors, correlations, and other summary analysis-of-variance statistics appear in Table IV for Model I and Table V for Model II. The coefficient functions: (*i*) square root of average counting rate, $y(x,L)$; (*ii*) square root of average equatorial counting rate, $A(L)$; and (*iii*) position of cutoff, $x_c(L)$; are well-determined and applicable values, standard errors, and correlations appear in Figs. 19 and 24 for $y(x, L)$ (and Figs. 45 to 47 for the flux); Figs. 8, 11, 21, 22, and 30 for $A(L)$; and Figs. 9, 12, 22, 23, and 30 for $x_c(L)$ (and Fig. 44 for altitude).

14.7 *Some Physical Results*

14.7.1 *Flux Maps* (Section XII)

Flux maps are given in B,L and R,λ coordinates and as J,B contours for constant L, based on the fitted model and using a calibration of the detector assuming certain single-component energy spectra. Neglecting uncertainties of calibration, the *relative* fluxes have a standard error of about 2 percent. The value of the maximum flux is $(5.7^{+1.4}_{-2.8}) \times 10^3$ protons/cm^2 sec at $L = 1.46$ on the magnetic equator.

14.7.2 *The Cutoff* (Section XI)

The minimum geographical altitude corresponding to the fitted cutoff function was computed. This altitude varies as a function of L and has a value of about 270 km at the magnetic equator at $L = L_0 = 1.13$ and a minimum of about 160 km at $L = 1.6$. The shape of this L dependence suggests that the interaction between the protons and the residual atmosphere is of major importance in determining the cutoff for values of L less than 1.9. For larger L values, the loss mechanism determining the cutoff is of different origin.

14.7.3 *Temporal Effects* (Section X)

The general spatial distribution of high-energy protons is very stable in time over the period covered by the present data; however, using residuals as a sensitive indicator, we find two temporal effects that are distinguishable from instrumental effects. Firstly, there appears to be an increase in the flux in the $1.9 < L < 2.2$ region during the 30-day period starting about day 280, 1962. This increase varied from about 5 to 90 percent depending on both x and L. Secondly, there is an indication of a qualitative increase in the altitude of the cutoff over the period of the observations. The present results indicate that any diurnal variability of the earth's magnetic field would have an upper limit of 0.003 Gauss at $\mathrm{L} \approx 1.5$.

14.7.4 *Comparison with Other Experiments and Theory* (Section XII)

The absolute fluxes measured in this experiment agree well (within a factor of two) with other extensive experimental measurements, but the present values are in general slightly lower. Spatial distribution of the flux agrees very well with other measurements but differs appreciably from published theoretical calculations.

14.8 *Extensions* (Sections XIII, IV, and Appendix B)

The methods developed in this work have lead to a very satisfactory representation of the high-energy proton data from the *Telstar*® 1 satellite.

With the better methods of utilizing data and selecting samples noted in this paper, and with more general functional forms (some approaches to which have been indicated), it should be possible to represent the radiation intensity for other more extensive and less "well-behaved" bodies of data than the one treated here. Most aspects of the statistical methods developed are generally applicable to problems of modeling data mathematically.

XV. ACKNOWLEDGMENT

The authors are indebted to the many people who have made substantial contributions to various phases of this work. In particular, we thank C. S. Roberts for enlightening discussions regarding various aspects of the model; Mrs. M. Becker, Miss E. A. Blake, Mrs. N. L. Graham, Mrs. A. S. Michaels, and Mrs. M. F. Robbins, for their contributions to the data analysis; D. R. Cox for the suggestion for distinguishing 'coefficient redundancy' from poor 'design'; and J. W. Tukey for the suggestion to examine the mean square deviation of residuals in the x,L cells and for editorial advice.

APPENDIX A.

The Instrument

Energetic electrons and protons were measured on the *Telstar*® 1 satellite by a group of detectors in all of which the sensitive element was a phosphorous-diffused silicon diode specially developed for such particle measurements.[7] The active volume of the device is the disk-shaped space-charge region of the diode under reverse bias. For the detector measuring protons with energies above 50 MeV, the reverse bias was approximately 100 volts, the space-charge region was approximately 2.8 mm in diameter and 0.39 mm thick, and the diode was shielded by about 12 mm of aluminum over a solid angle of 2π and somewhat more than 12 mm of aluminum equivalent over the remaining hemisphere (see Fig. 53).

The thickness of the space-charge region of the detector was measured with protons from a cyclotron. A calculation of the path-length distribution for unscattered particles in the space-charge region and in the surrounding shielding materials has been made. These calculated results have been combined with range-energy information, and the properties of the associated electronic circuits, to give the geometric factor of the instrument, $g(E)$, as a function of the energy, E, of protons incident on the spacecraft. The geometric factor varies with the reverse bias voltage and the temperature of the detector, both of which affect the effective thickness of the active volume of the diode. Fig. 54 is a graph of $g(E)$ vs E for a bias voltage of -97.5 volts and a temperature of 20°C, the nominal operating conditions of the instrument. Note that protons with energies below 50 MeV were not detected.

The geometry of the detector and shield is only approximately omni-

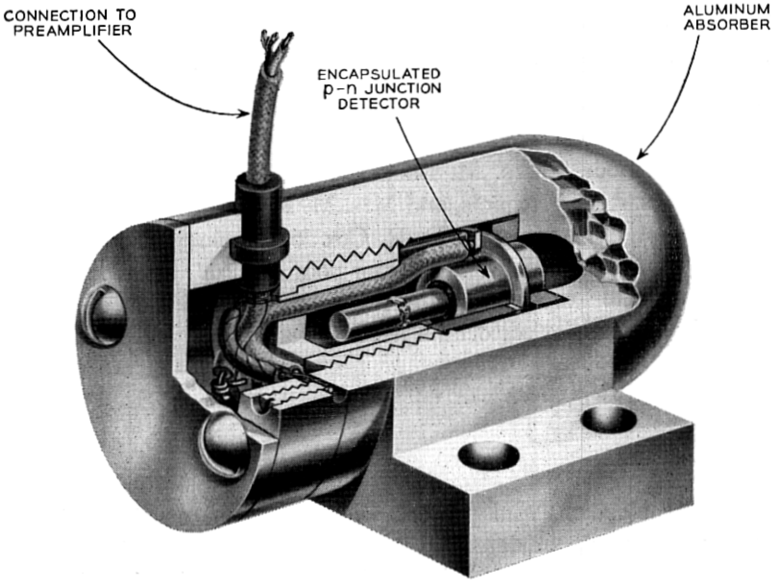

Fig. 53 — The instrument.

directional. However, the satellite was spin stabilized, the symmetry axis of the detector was nearly perpendicular to the spin axis of the satellite, and the telemetered counting rate was an average over at least 15 revolutions of the satellite. This averaging process tends to remove any directionality inherent in the detector geometry. A sensitive analysis noted in Section 7.10 failed to show any directional dependence in the data.

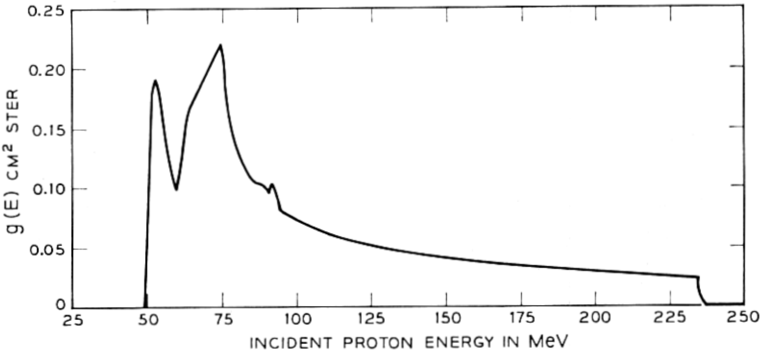

Fig. 54 — Dependence of geometric factor on energy of protons incident on the shielding.

For a differential energy spectrum $N(E)$, where $N(E)dE$ is the number of protons with energies between E and $E + dE$, the average geometric factor, $\bar{g}(E_1, E_2)$, of the detector for particles with energies between E_1 and E_2 is defined by

$$\bar{g}(E_1, E_2) = \frac{\int_0^\infty g(E)N(E)\, dE}{\int_{E_1}^{E_2} N(E)\, dE}. \tag{20}$$

The function $\bar{g}(50 \text{ MeV}, E_2)$ has been evaluated numerically for various values of E_2 and forms of $N(E)$. The values of $\bar{g}(50 \text{ MeV}, 130 \text{ MeV})$ are plotted in Fig. 55 as a function of n for the single-component power-law spectrum $N(E) \propto E^{-n}$, and also as a function of E_0 for the single-component exponential spectrum $N(E) \propto \exp(-E/E_0)$. It may be seen from the figure that $\bar{g}(50 \text{ MeV}, 130 \text{ MeV})$ varies by less than 6 percent from 0.143 cm^2 ster for $0 < n < 7.5$ and $10 \text{ MeV} < E_0 < 90 \text{ MeV}$. These ranges of n and E_0 include most experimentally determined values by a comfortable margin.[3,5,29,34,35] The omnidirectional flux, $J(E_1, E_2)$, of protons with energies between E_1 and E_2 is given by

$$J(E_1, E_2) = \frac{4\pi Y^2}{\bar{g}(E_1, E_2)}, \tag{21}$$

where Y^2 is the counting rate of the detector. In the body of this paper, the values $E_1 = 50$ MeV, $E_2 = 130$ MeV and

$$\bar{g} \equiv \bar{g}(50 \text{ MeV}, 130 \text{ MeV}) = 0.143 \text{ cm}^2 \text{ ster} \tag{22}$$

are used. The flux $J(50 \text{ MeV}, 130 \text{ MeV})$ is designated simply by J,

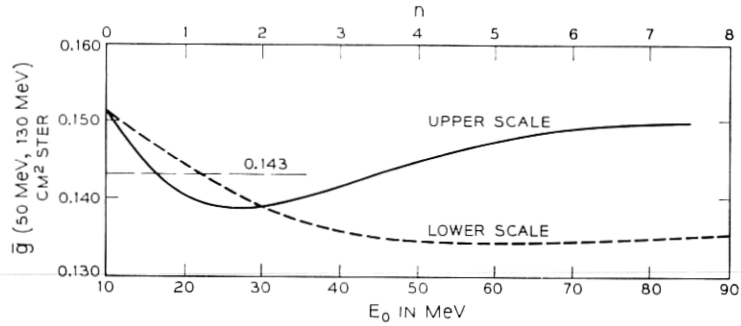

Fig. 55 — Dependence of average geometric factor on the exponent of a differential power-law energy spectrum and the e-folding energy of an exponential energy spectrum.

and the counting rate to flux conversion is considered to be independent of the proton energy spectrum.

While the relative value of $\bar{g}$ shows a variation of less than 6 percent for the wide range of single-component energy spectra noted above, the absolute value of $\bar{g}$ is less well specified. Variations in the ambient temperature and reverse bias voltage may change the effective geometric factor by as much as 25 percent. The difficulty of dealing with the complexities in shielding geometry, caused by embedding the instrument in the spacecraft, introduces additional uncertainties in the absolute value of $\bar{g}$. These uncertainties are in the range of -25 to $+50$ percent.

No provision was made for recalibrating the detector once the satellite was in orbit. However, the evidence, which is discussed in Section X, concerning the temporal variations of the proton distribution is that neither the detector nor the associated circuit elements were substantially affected by the space environment. Instrumental (e.g., temperature and bias voltage) effects are often quite different in character from temporal changes in the proton belts and may be separated from them in many circumstances. It is, of course, possible to postulate instrumental effects that will be inextricably confounded with certain secular changes that might take place in the proton distribution.

APPENDIX B.

Some Statistical Details

B.1 *Introduction*

This appendix presents, heuristically, some facts and formulae concerning the statistical analysis of the data. While a variety of statistical principles, precepts and procedures were employed as guides, the main judgments came from empiricism, scientific intuition and common sense. Various kinds of plots of residuals, used informally, have been of key importance, both for evaluation and for suggestion.

Simply stated, the objective was to produce a statistically accurate analytical description of the intensity distribution of high-energy protons in space surrounding the earth. The process of analysis involved the empirical evolution of a mathematical model, in interaction with the application of fitting and evaluative techniques. The data source and processing have been described in Sections II and III. The iterative and interactive processes of the final stages of model development, fitting, data partitioning and data sampling are described in Sections IV to IX.

Appendix B.2 deals with the basis for use of the square root transformation, Y, of the counting rate data, Y^2. Appendix B.3 discusses the selection of a sub-sample used in fitting. The use of the method of least squares in nonlinear model fitting, to estimate unknown coefficients, or functions of the coefficients, and their standard errors and correlations is reviewed briefly in Appendix B.4. Some remarks on construction of sums of squares contours, often referred to as confidence regions, and of indices of local nonlinearity of the model are given in Appendix B.5. Appendix B.6 discusses several issues relevant to the interpretation of the analysis of variance results. Appendix B.7 describes a mode of "smoothing" data within cells, which could have been used in conjunction with the sub-sampling procedure. Appendix B.8 concerns the technique of probability plotting.

B.2 *The Square Root Transformation*

It appears a reasonable assumption (supported by some empirical evidence) that, in the absence of geophysical disturbances, at a fixed point in space relative to the earth, the number of counts Z, recorded in the detector in 11 seconds, will vary in time according to a Poisson distribution, i.e.,

$$\text{Probability }\{Z = z\} = \frac{e^{-\nu}\nu^{z}}{z!}, \qquad z = 0, 1, 2, 3, \cdots, \tag{23}$$

where the parameter of the distribution, ν, is the mean value of Z.

With this statistical model, the average intensity of radiation in the region of space measured by the detector is proportional to ν, where the proportionality factor depends on the counter geometry and efficiency. The objective is to develop a function which describes how ν varies in space, based on observations of the quantity Z at different positions in the satellite orbit.

For the Poisson distribution, the variance of Z is also ν, i.e., the average of the squared deviations, $(Z - \nu)^2$, is ν. Thus, as the value of ν changes, the variance of the associated random variable Z also changes. Hence, the scatter of Z about its average value will be different in different regions of space as the average intensity fluctuates.

Working with the experimental data on the scale of Z has two drawbacks. Firstly, if one fitted a mathematical model to the data using a least squares criterion, the different observations would have variable weight, which would require appropriate, troublesome, allowance in the fitting procedure. Secondly, graphical judgment of the adequacy of any particular fit would be difficult because of the variable scatter of the data about a fitted function in different regions.

Thus, the square root transformation, Y, of the counting rate ($Y^2 = Z/11$ counts per sec) was used to "stabilize" the variance and the model-fitting procedure employed unweighted nonlinear least squares on Y (but with some data weighting as discussed in Section 7.1 and Appendix B.3).

Heuristically, consider the linear Taylor's expansion of Z about ν

$$\sqrt{Z} \doteq \sqrt{\nu} + \frac{(Z - \nu)}{2\sqrt{\nu}} \cdots . \tag{24}$$

Then, the variance of $\sqrt{Z}$ is approximately

$$\mathrm{Var}\,(\sqrt{Z}) \doteq \left(\frac{1}{2\sqrt{\nu}}\right)^2 \mathrm{Var}\,(Z - \nu) + \cdots . \tag{25}$$

If

$$\mathrm{Var}\,(Z - \nu) \propto \nu, \tag{26}$$

then

$$\mathrm{Var}\,(\sqrt{Z}) \mathrel{\dot{\propto}} \frac{1}{4}\frac{\nu}{\nu} = \frac{1}{4}, \tag{27}$$

that is, Var ($\sqrt{Z}$) would be approximately a constant.

Discussions of this transformation are given by Bartlett[42] and Anscombe.[43] If the distribution is in fact Poisson, then Anscombe shows that the average value of $\sqrt{Z}$ is approximately

$$\sqrt{\nu} - \frac{1}{8\sqrt{\nu}} - \frac{7}{128\nu^{\frac{3}{2}}},$$

while the variance of $\sqrt{Z}$ is, asymptotically,

$$\frac{1}{4}\left\{1 + \frac{3}{8\nu} + \frac{17}{32\nu^2} + \cdots\right\}.$$

Again for the Poisson distribution, Bartlett gives exact values of the dependence of the variance of $\sqrt{Z}$ on ν, summarized in the following:

ν:	0	0.5	1	2	3	4	6	9	15
Var $\sqrt{Z}$:	0	0.310	0.402	0.390	0.340	0.306	0.276	0.263	0.256

For a Poisson distribution, a transformation of the form $\sqrt{Z + 1/2}$ or $\sqrt{Z + 3/8}$ or $(\sqrt{Z} + \sqrt{Z + 1} - 1)$ will improve the variance stabilization at smaller ν values. In the present application, such a modification would have appeared physically artificial and inconvenient. Moreover, the actual variance of the observations exceeds the Poisson variance (see Appendix C) and the "correction" was thus felt to be unwarranted. Some response to the (empirically defined) variance instability remaining after the square root transformation was made in the form of some weighting in the data selection (described in Section 7.1 and Appendix B.3).

Of course, if one wished to adopt the assumption of a Poisson distribution as an absolute basis for procedure, instead of as a guide, then one might choose to use maximum likelihood to estimate the coefficients of the model. This would mean developing a procedure for determining values of the coefficients [of the function $\nu(x,L)$] which would maximize

$$\prod_{\text{observations}} e^{-\nu(x,L)}[\nu(x,\, L)]^{z}/z!.$$

In the present case, a general program for nonlinear least squares was available while a procedure for Poisson likelihood maximization would need to be evolved. Apart from this practical consideration, however, it seemed more robust to use the Poisson assumption as a guide to developing an appropriate transformation preliminary to fitting by least squares. The point is that the square root transformation will effect an approximate variance stabilization not only when the variance is *equal* to the mean (as in the case of the Poisson distribution) but also when, more generally, the variance is *proportional* to the mean. Empirical vindication of this caution is given in Appendix C. Moreover, the least squares approach enables the approximate statistical interpretation of results using familiar procedures from linear multiple regression methods.

The present analysis is based on the quantity Y, where Y^2 = counting rate = $Z/11$ counts per sec. Thus, if in fact Z were a Poisson variable,

$$\operatorname{Var}(Y) \doteq \left(\frac{1}{11}\right)\left(\frac{1}{4}\right) = 0.023, \tag{28}$$

as a reasonable approximation. When the average counting rate exceeds 1/11, this value of 0.023 is a lower bound on the variance of Y, even with the Poisson assumption. Moreover, there are many other possible sources of intrinsic variability and experimental error in this situation.

A further benefit which one might expect from the square root transformation in this circumstance is that the distribution of residuals would tend to be more symmetric and more nearly normal (Gaussian).

Some empirical properties of this square root transformation in the present body of data are given in Appendix C.

B.3 *Sample Selection*

As a practical requirement, the available multivariable, multicoefficient, nonlinear least squares fitting program could operate with a maximum of 1000 data points. Hence, the 41,135 HTB observations needed to be sampled or condensed at a 1 in 40 ratio.

As in all real sampling or experimental design situations, many competing criteria and practical difficulties were relevant. Perhaps the overriding point, explicitly understood here (and probably true in most actual model fitting problems), is that the model which was being developed was not the "truth" but was really just a smoothing function which one wanted to fit well over a wide region of space. Thus, it was not appropriate to think of estimating the model coefficients, say, so as to optimize their apparent (indicated) statistical reliability, nor would it be appropriate to try to use all the available data in an equally weighted manner, since accidents of orbital position and instrumental behavior would have too great an effect on the distribution of data points.

The procedure developed for the present use is outlined in Section 7.1, with pertinent remarks also in Section 13.3 and Appendix B.7.

The method of Section 7.1 yielded 960 observations to which the model was then fitted using unweighted least squares. The 960 sampled observations were selected so as to be roughly speaking, "widely spaced," the metric being change in average counting rate. Thus, the challenge of fitting the 960-point sample, as measured by sum of squares of residuals, is *greater,* on a per-observation basis, then would be that of fitting the entire body of 41,135 HTB observations, very many of which are quite close together. The "model bias" difficulties of the entire body of data are concentrated in the sample. The statistical fluctuation would be approximately the same, on a per observation basis, in the sample as in the whole body of data.

B.4 *Estimation Procedure*

The unspecified coefficients of the models defined in Section IV were estimated so as to minimize the sum of squares of deviations between the observed Y and fitted y, for the sample array of data. The iterative, multivariable, multicoefficient, nonlinear least squares fitting was executed using a computer program due to Huyett and Wilk,[44] based on a procedure outlined by Wilk[45] (see also Lundberg, Wilk and Huyett).[46, 47]

The classical statistical properties of least squares estimation, namely unbiased estimates with minimum variance, apply in the case of statistically uncorrelated observations having equal variances and with the coefficients to be estimated occurring linearly in the model (see, for example, Wilks[16]). In the present case, even with the square root transformation, the observations do not have equal variances but, for practical purposes, the weighting implied by the selection procedure (see Section 7.1) compensates adequately. The model is, however, quite nonlinear in the coefficients. Still, one hopes that the attractive statistical properties of linear least squares carry over approximately to the nonlinear case because, in small enough neighborhoods, nonlinear functions can be linearly approximated. (An index for measuring model nonlinearity is described in Appendix B.5.) In any case, the least squares criterion is geometrically appealing and primitively meaningful.

Among the by-products of the fitting procedure, applied to the particular array of data in x,L space, are approximate values for the standard errors of the estimated coefficients, a matrix of approximate pairwise correlation coefficients for the estimated coefficients, an analysis-of-variance table giving the sum of squares accounted for and not accounted for by the fitted model, a list of residuals (equal to observed minus fitted), and various plots.

The least squares estimates of single-valued functions of the coefficients, such as $A(L)$, $x_c(L)$, or $y(x, L)$ are simply the same functions of the estimates of the coefficients (since least squares is an invariant process). Approximate variances and correlations of functions of the coefficients may be derived as follows: If $\theta' = (\theta_1, \cdots, \theta_p)$ denotes the coefficients of the model, and $\hat{\theta}$ their estimates, then the approximate covariance of the estimates $g(\hat{\theta})$ and $h(\hat{\theta})$ of the functions $g(\theta)$ and $h(\theta)$ is

$$\text{Covariance } (g(\hat{\theta}), h(\hat{\theta}))$$

$$= \text{Cov } (g(\hat{\theta}), h(\hat{\theta}))$$

$$= \text{Statistical average of } \{(g(\hat{\theta}) - g(\theta))(h(\hat{\theta}) - h(\theta))\}$$

$$
\begin{aligned}
&\cong \sum_i \sum_j \left[\frac{\partial g(\theta)}{\partial \theta_i}\right]_{\hat{\theta}} \left[\frac{\partial h(\theta)}{\partial \theta_j}\right]_{\hat{\theta}} \operatorname{Cov}(\hat{\theta}_i, \hat{\theta}_j) \\
&= \sum_i \left[\frac{\partial g(\theta)}{\partial \theta_i}\right]_{\hat{\theta}} \left[\frac{\partial h(\theta)}{\partial \theta_i}\right]_{\hat{\theta}} \operatorname{Var}(\hat{\theta}_i) \\
&\qquad + 2 \sum_{i<j} \left[\frac{\partial g(\theta)}{\partial \theta_i}\right]_{\hat{\theta}} \left[\frac{\partial h(\theta)}{\partial \theta_j}\right]_{\hat{\theta}} [\operatorname{Var}(\hat{\theta}_i) \operatorname{Var}(\hat{\theta}_j)]^{\frac{1}{2}} \rho_{ij} , \qquad (29)
\end{aligned}
$$

where ρ_{ij} is the correlation of $\hat{\theta}_i$ and $\hat{\theta}_j$. The formula for the approximate variance of $g(\hat{\theta})$ is then just a specialization of the above, putting $g = h$.

Some associated facts and issues are worth mentioning here. First, the approximate statistical correlations ρ_{ij} of the estimated coefficients of the model, or of functions of these, depend on (*i*) the distribution of the sample in x,L space, (*ii*) the values of the coefficients and (*iii*) the nature of the mathematical model; but do *not* depend on the actual adequacy or appropriateness of the fit. Similarly, the approximate standard errors of estimates are each made up as a product of which one term depends upon the square root of the mean square of the residuals of fit and the other depends only on the same factors as do the ρ_{ij}. Second, the various statistical measures, such as standard errors of estimated coefficients which are obtained from the fit to the 960-point HTB sample are, in a narrow statistical sense, conservative because they refer to the *sample* only and do not make allowance for the fact that the fitted model does indeed fit very well to the *entire body* of 41,135 HTB data. Thus, if statistical fluctuations were the only factor in the uncertainty of the estimates, one might further reduce this uncertainty by some factor, roughly approximated by $6 \approx \sqrt{41{,}135/960}$. This view of statistical uncertainty does not, however, give appropriate weight to the "model bias", which will not be eliminated by *any* number of observations. Third, all the summary statistical measures, which are referred to as standard errors, correlations, confidence regions, etc., should be used and interpreted in a data analytic way, i.e., as indicating facets of the body of data and the adequacy of its description by the model and analysis—rather than in terms of some supposedly "true" model or hypothesis which one is trying to evaluate in probabilistic terms.

B.5 *Sums of Squares Contours, "Confidence Regions" and Nonlinearity Indices*

The models of Section IV are defined up to the values of the unspecified coefficients. Any set of values for these coefficients may be said to provide a "fit" to the 960-point sample of data. Thence one can define a sum of squares function of the set of coefficients as

$$SS\ (\text{coefficients}) = \sum (\text{observed} - \text{“fitted”})^2, \tag{30}$$

which will take on various (positive) values as one varies the values of the coefficients. In the space of the coefficients there exist then, in principle, contours of this "sum of squares" function.

While standard errors provide information on reasonable allowances for the estimate of a single parameter in the light of the fit of the model to the actual body of data, they do not carry any information on the *joint* statistical properties of the estimates. A reasonable (robust and primitive) indication of joint statistical behavior is provided by these "sum of squares" contours in coefficient space.

In the case of models in which the unknown coefficients occur *linearly,* these contours are a family of ellipsoids defined by certain simple quadratic functions of the coefficients. The orientation and shape of this family of ellipsoids indicate the interdependence of the estimates of the coefficients in the light of the data, and show which coefficients are well-determined and which poorly. However, the interpretive value depends heavily on geometrical appreciation and, for more than a few coefficients, high-dimensional representation cannot be achieved directly.

The ellipsoid (even in the linear case) is *not* defined, in general, by its one-dimensional projections. (The standard error of a coefficient estimate is half the length of the projection of the unit ellipsoid of the family onto the coefficient axis.) But, as a matter of simple geometrical fact, *all pairs* of two-dimensional projections *do* uniquely define the ellipsoid. Thus, one practical means of a complete graphical representation of the high-dimensional ellipsoid is in terms of all possible pairwise planar projections.

For the case of linear models, on the basis of a series of assumptions —namely that the differences between the model and the observations are due to statistical fluctuations which are normally and independently distributed all with zero mean and the same variance—some may choose the abstract probabilistic interpretation of these ellipsoids as "confidence regions" (see, for example, Wilks[16]). If this interpretation is used, it is necessary that the distinctions and relationships between the joint, pairwise and marginal confidence coefficients and regions or intervals be understood. Details will not be provided here. Briefly, if a nine-dimensional ellipsoid were specified to have a confidence coefficient of β_9, then any two-dimensional projection would have a confidence coefficient of β_2, interpreted marginally. The relation between β_9 and β_2 is indicated by the following:

β_9	β_2
0.13	0.90
0.25	0.95
0.50	0.984
0.75	0.997
0.90	0.9994
0.95	0.99995

In the present case, the model is nonlinear and the fluctuations are not normal. Contours of the sums of squares function as a function of the coefficients can, in principle, be obtained for a given body of data and will *not* be ellipsoids. In practice, however, obtaining these contours is so laborious as to be virtually impossible.

However, one may consider a linear (planar) approximation to the nonlinear model in the neighborhood of the least squares estimates of the coefficients and thence obtain expressions for a family of ellipsoids which *may* be reasonably good approximations to contours of the sums of squares function. An index of the effective nonlinearity of the model is the nonconstancy of the sums of squares of residuals on these ellipsoids and this can be normalized by division by the value of the minimum sum of squares. Such measures are presented and discussed in Sections VIII and IX.

Given that the linear approximation is adequate, the nonnormality of the observations should not deter those who seek (and who believe in) the general probabilistic confidence interpretation since the statistical process is likely very robust.

Sections VIII and IX contain specific examples of some of the pairwise projections of these "approximations to sum of squares contours." Specifically, the size of the 9-dimensional ellipsoid was such that, if all the statistical assumptions applied, a joint 0.99 confidence coefficient could be attached. Since a complete set of pairwise projections for nine coefficients involves 36 ellipses only a few are shown. As a summary indicator of the nature and behavior of these ellipses the quantity

$$\alpha = (\text{sign of } \rho)\cdot(1 - \sqrt{1 - \rho^2}) \tag{31}$$

is tabulated (in Tables IV and V), where ρ is the correlation of the pair of coefficients involved. The value of $1 - |\alpha|$ is the ratio of the area of the actual ellipse to that of the largest ellipse which could be inscribed in the rectangle formed by the horizontal and vertical tangents to the actual ellipse (see Wilk[48]). The range of α is $-1 \leqq \alpha \leqq 1$ and large values of $|\alpha|$ (say above 0.75) corresponds to narrow ellipses with major axis oblique to the coordinate axes, and represent situations of high interdependence of the coefficient estimates.

B.6 *The Analysis of Variance*

The analysis of variance provides a summary description of the apportionment of the "variability" of a body of data in the light of the model employed for analysis, where variability is defined in terms of sum of squares.

Given n observations, one may visualize an n-dimensional observation space, whose coordinates represent the possible values of each of the n observations. The data are then represented by a fixed point in this space.

The model, having p unspecified coefficients, implies certain functional relationships amongst the coordinates of the observation space. Thus the model effectively defines a constraining "surface" of p dimensions, and each point on this surface corresponds to some set of values of the unspecified coefficients of the model. The least squares estimate of the coefficients corresponds to that point on the constraining surface which is closest to the actual data point. If the coefficients in the model occur linearly then the constraining surface is a hyperplane which ordinarily, by definition of the observations, contains the origin, and, if the model includes a constant term, also contains the equiangular line (corresponding to the mean).

The squared distance of the data point to the origin is then the total sum of squares, $\sum Y_i^2$, while its shortest squared distance to the constraining surface is the error or residual sum of squares, associated with lack of fit. The difference between these may be termed the model sum of squares and, for linear models, this is actually the squared distance from the least squares estimates point to the origin.* If a constant term is included in a linear model, then the model sum of squares may be further decomposed additively in terms of the squared

---

* In the linear case, the model sum of squares is easily computed directly as the squared length of the projection onto the hyperplane of the line joining the data point and the origin. This fact is used in the present iterative computer program in checking convergence.

perpendicular distance (call it D_1^2) of the least squares estimate point to the equiangular line and the squared distance (call it D_2^2) along the equiangular line, from the foot of that perpendicular, to the origin. This latter quantity D_2^2 is usually termed the sum of squares due to the mean. The squared distance of the above-defined point on the equiangular line to the data point is called the corrected total sum of squares, $\sum (Y_i - \bar{Y})^2$ and is just $\sum Y_i^2 - D_2^2$. The ratio of the squared length D_1^2 to the corrected total sum of squares is defined as the squared multiple correlation, R^2, and often used as a measure of accomplishment of a model. It is easy to show that R^2 defined above is equal to

$$1 - \frac{\text{sum of squares for error}}{\text{total corrected sum of squares}}.$$

This latter quantity is computable even when the model is nonlinear and/or does not contain a constant term.

One may define contours of sums of squares of residuals in the constraining surface as the loci of the intersections with the surface of given radii from the observation point. In the event that the constraining surface was a hyperplane, which would be true if the unspecified coefficients in the model occur linearly, then these loci (or contours) would be a family of p-dimensional spheres. For nonlinear models, this will be approximately true for a sufficiently small neighborhood of the least squares point.

The particular form of the model, in regard to the unspecified coefficients, defines a coordinate system within the constraining surface. Three cases are worth distinguishing. First, the constraining surface is a hyperplane and the coefficients are linear. Second, the surface is a hyperplane but its coordinates are nonlinear. The second case may be reduced to the first by appropriately transforming the coefficient coordinate system. Third, the surface is nonlinear. In this case one can approximate the surface by a hyperplane in a small neighborhood. Thus, in a sufficiently small neighborhood, the situation can be regarded as linear.

The approximately or exactly linear coordinates implied by the model will in general be nonorthogonal. Thus, the representation of the spherical (exact or approximate) contours in an orthogonal coordinate system for the coefficients yields a family of ellipsoids. In the sense of measuring lack of fit by sums of squares between fitted and observed values, these contours in coefficient space constitute sets whose members are "equidistant" from the data point.

B.7 *A Procedure for Smoothing in Cells*

In Sections 7.1, 13.3 and Appendix B.3, discussion of why and how to sample and possibly "smooth" the data has been given. One specific practical possibility is now described.

Suppose one has a preliminary fit of the model, represented by $g(w_i\, ;\, \hat{\theta})$, where $\hat{\theta}' = (\hat{\theta}_1\, , \hat{\theta}_2\, , \cdots , \hat{\theta}_p)$ are the fitted coefficient values and w_i denotes the independent variables. Suppose this preliminary fit is used to partition the space of the independent variables (here x and L) into some approximation of equirange cells, as described earlier. As argued in Section XIII, it may be profitable to "smooth" the data in each cell so as to yield a value generally representative of all the observations in that cell, instead of using a random selection from the cell.

A sensible smoothing function for each cell is, clearly, the model $g(w;\, \theta)$. A simple procedure is, for each cell separately, to carry out one stage of linear adjustment, doing the linear least squares regression of $\{Y_i - g(w_i\, ;\, \hat{\theta})\}$ on $\partial g/\partial \theta_1 \,|_{\hat{\theta}}\, , \cdots , \partial g/\partial \theta_p \,|_{\hat{\theta}}$, to obtain the regression coefficients $\tilde{\delta}' = (\tilde{\delta}_1\, , \cdots , \tilde{\delta}_p)$, for that particular cell. Then the smoothing function for that cell would be $g(w;\, \tilde{\theta})$ where $\tilde{\theta} = \hat{\theta} + \tilde{\delta}$. A representative "smoothed observation" for that cell might then be the quantity $g(\bar{w};\, \tilde{\theta})$, where $\bar{w}$ is, say, the mid-point of the cell.

This process permits each cell, overall, to determine a single value to represent it in the entire fitting process and diminishes the chance that a random selection from a cell may be unnecessarily nonrepresentative of that cell behavior.

If one had wished to fit to *all* the available data, then the smoothed cell values would be weighted in proportion to the number of data in the cell. In the present case, this was deliberately *not* done.

The goodness of fit of a model to smoothed cell values, not differentially weighted, cannot be statistically judged directly from the analysis of variance since the residuals are no longer individually statistically comparable and the mean square residual is not an estimate of the error variance of the observations. However, the fitted model can be assessed by functions of its residuals from the original data (or a sample thereof).

B.8 *Probability Plotting*

The techniques of probability plotting are useful for data analysis in a wide variety of circumstances. (See Wilk and Gnanadesikan[17] for a general discussion of probability plotting techniques.) For instance, in the present work, plots of residuals against various variables have provided invaluable guidance, but one is also interested in the distributional behavior *per se* of the collection of residuals. As presented in Section 8.1, normal and half-normal probability plots have been used for this purpose.

The rationale for such probability plots is roughly as follows: If one draws a random sample of size n from a population which is normally distributed with mean μ and variance σ^2 then the ordered observations would be expected to approximate, roughly, to a linear function, $\mu + \sigma z_i(n)$, of appropriate "representative" values $z_i(n)$ from a standard normal ($\mu = 0$, $\sigma^2 = 1$) distribution. Thence a plot of the ordered observations against the $z_i(n)$ would tend to be linear, with intercept approximately μ and slope approximately σ. For the representative value, $z_i(n)$, corresponding to the ith ordered observation, one can use the standard normal quantile for the proportion $(i-\frac{1}{2})/n$.

This plotting technique displays the individual observations in a sample graphically and does so against a backdrop such that the existence of outliers and asymmetry, as well as other distributional properties, are sensitively indicated. Of course such plots are usually profitably supplemented by others that order or partition the data according to information extraneous to the responses themselves.

We expect the mean of the residuals, $Y - y$, in the present study (see Section 8.1) to lie near 0. Also we expect that their variances will be approximately the same, since that is the purpose of the square root transformation. As a further benefit of the square root transformation we expect that the distribution of the residuals will tend to be symmetric and to approach normality; thence the present application of *normal* probability plotting of the residuals. The fact that these residuals are not entirely statistically independent—since they derive from a commonly estimated fitted function—is a minor issue since the number of observations is so much larger than the number of fitted coefficients.

Half-normal probability plotting employs the ordered *absolute* residuals plotted against standard half-normal (standard normal folded at 0) distribution quantiles. Such a plot eliminates any symmetry-type information but provides an incisive focus in bringing together on the plot the largest departures from fit.

Probability plots can provide very sensitive indications of distributional peculiarities especially in regard to "overly" large values. Sometimes the indications are of little practical interest, such as minor lumps which one can see in Fig. 29, but in other regards, such as in estimating an "intrinsic" error standard deviation, the plots may permit a good judgment on how to discount or correct for apparently aberrant values which might otherwise have an undue influence, say, on mean square error.

Error standard deviations may be estimated from normal or half-normal probability plots as the "slope of the linear configuration." Typically, it will not be relevant to make a great show of objectivity in this process since the declared purpose is to permit an informal discounting of unexpected distributional peculiarities. Thus, in Fig. 29, one takes the slope as defined essentially by the bulk of residuals, ignoring the few largest.

APPENDIX C

Statistical Measures Over All the HTB Data

This appendix presents various statistical measures over all the 41,135 HTB data. These measures concern the fit of Models I and II and the partition of the x,L space (as described in Section 7.1 and Appendix B.3) into 1034 cells of which 813 were nonempty of observations. The partition is such that the range of y within cells is relatively small. For each cell, two functions are used: (*i*) The mean square deviation (MSD) defined as

$$\mathrm{MSD}\,(u) = \frac{1}{n-1} \sum_{j=1}^{n} (u_j - \bar{u})^2, \tag{32}$$

where the cell has n observations and u_j denotes some function of a cell observation, e.g., Y_j or Y_j^2, and $\bar{u}$ is the mean of the u_j in the cell; (*ii*) The mean square residual (MSR) defined as

$$\mathrm{MSR}\,(Y) = \frac{1}{n} \sum_{j=1}^{n} (Y_j - y_j)^2, \tag{33}$$

where y_j is the fitted value (from Model I or II) corresponding to the observed Y_j.

C.1 *Empirical Justification of Square Root Transformation*

Figs. 56 and 57 show plots of MSD(Y^2) versus the cell mean of Y^2 and MSD(Y) versus the cell mean of Y, respectively. It is seen that MSD(Y^2) shows a distinct and major dependence on the average value of the counting rate, Y^2, while MSD(Y) does not show systematic increase relative to the average value of Y, except, as expected, in the close neighborhood of zero counting rate.

A more detailed analsis of the results of Fig. 56 indicates that the dependence of MSD(Y^2) on cell mean of Y^2 is somewhat curvilinear having larger slope for larger Y^2 values. This curvilinearity is very likely mainly due to the mode of definition of the x,L cells. The procedure used tends to produce cells which are "too large" in regions where the counting rate is also large, thus leading to an apparent *extra* increase in MSD(Y^2) with Y^2. At all values, however, the dependence of MSD(Y^2) on Y^2 is greater than the slope 0.09 (=1/11) which would be associated with the Poisson distribution. The empirically observed slope varies from about 0.15, based on small values, to 0.3, based on large values of the MSD(Y^2).

These results suggest that one cannot hope to achieve, by means of

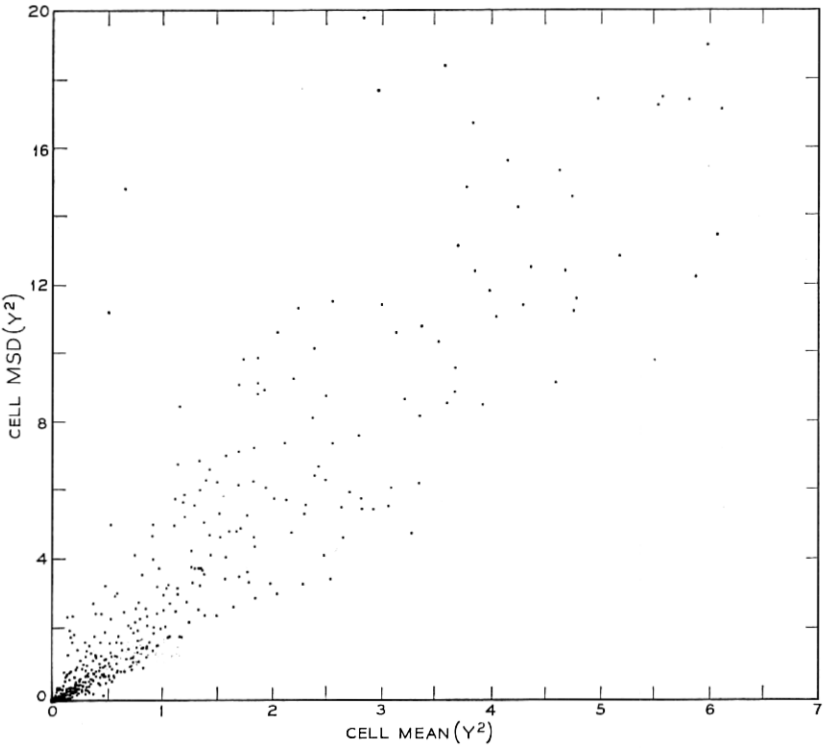

Fig. 56 — Cell MSD (Y^2) vs cell mean of Y^2 for the x, L cells defined in Section 7.1 and Appendix B.

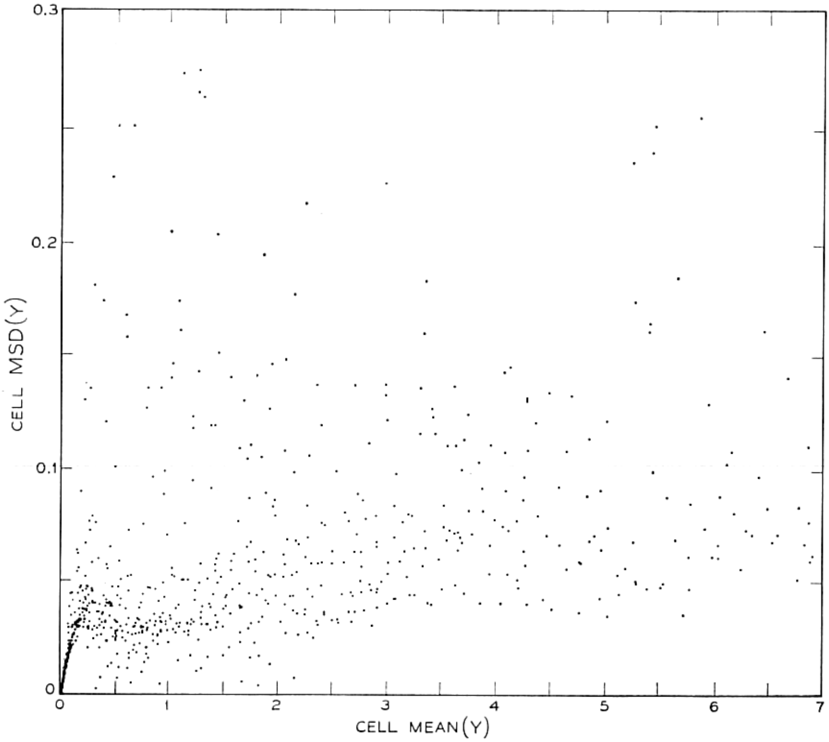

Fig. 57 — Cell MSD (Y) vs cell mean of Y for the x, L cells defined in Section 7.1 and Appendix B.

any fitted model based on x,L coordinates, on the scale of Y, a mean square residual (error) as low as 0.023 which is associated with the Poisson assumption.

Although the Poisson assumption provided a useful stimulus toward a profitable transformation of the data, these results confirm that it would have been unwise to have tied oneself too closely to the assumption as a complete basis for analysis, as for instance in basing the fit on maximization of the Poisson likelihood function (see Appendix B.2). Possible sources of variability and error in the data, beyond Poisson fluctuations in counts, have been discussed elsewhere in this paper.

C.2 *Determination of Weights*

The sample selection procedure involved "weighting" the 813 nonempty cells by selecting 2, 3/2, or 1 observation per cell. The observed

MSD (Y) were classified into three groups defined by: $0 \leqq \text{MSD} \leqq 0.013$; $0.013 < \text{MSD} \leqq 0.02$; $0.02 < \text{MSD}$. The x,L coordinates of the midpoints of cells so identified are shown in Fig. 58. The actual assignment of weights was based on applying contiguity considerations to this plot.

C.3 *Analysis of Variance Over All the HTB Data*

Table VIII summarizes the analysis of variance over all the 41,135 HTB data. The table covers the fit of Models I and II to all the data, using the estimated coefficients (see Tables IV and V) from the fit to the 960-point sample. Also, one can regard the collection of averages of the Y values in each of the 813 nonempty cells as providing a fit depending on 813 fitted quantities. The corresponding "error" (cell deviations) is the pooled cell MSD(Y). Finally, the residuals of the fit of Model I (or II) can be "fitted" by 813 cell

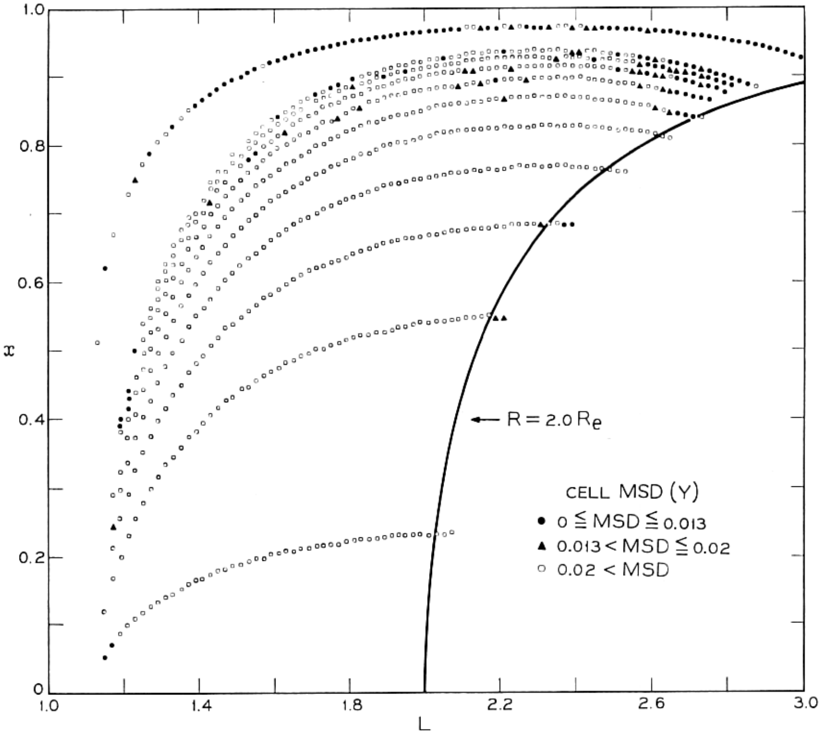

Fig. 58 — Positions of centers of regions in x, L space having certain ranges of cell MSD (Y). The ranges are indicated in the legend.

TABLE VIII—ANALYSIS OF VARIANCE OVER ALL THE HTB DATA (41,135 POINTS MINUS 226 OUTLIERS).

Due to	d.f.	Sum of squares	Mean square
Total (41,135–226)	40,909	230,267.45	
Mean	1	115,755.39	
Corrected total	40,908	114,512.07	
Model I residuals	40,900	1,411.3	0.0345
Model II residuals	40,901	1,419.6	0.0347
Cell deviations	40,096	1,541.4	0.0384
Cell dev. of Model I res.	40,085	1,167.0	0.0291
Cell dev. of Model II res.	40,086	1,166.9	0.0291

	Multiple R^2 value
Model I	0.988
Model II	0.988

averages of the residuals, leading to an "error" which is the pooled cell MSD($Y - y$), i.e., due to the cell deviations of the Model I (or II) residuals.

The fits to all the data provided by Models I and II are equally good, as was true for the 960-point sample. The mean square residuals over all the data (about 0.035) is *lower* than the value (about 0.036) obtained for the sample even though the fit of the model was determined by the sample. This bears out the expectation (see Appendix B.3) that the mode of selection of the sample is such that the sample was *harder* to fit on a per-observation basis than the entire body of data.

The cell means provide overall a poorer actual fit than Model I or II, and allowing for the number of fitted coefficients, the mean square for cell deviations exceeds that for the models by about 12 percent.

Fitting cell means to the model residuals yields an additional substantial reduction in the sum of squares of the model residuals and a mean square of about 0.029, which is some 17 percent lower than the value for the models. If in fact the models gave an "unbiased" fit everywhere, then one would expect that the values of pooled MSR(Y) and pooled MSD($Y - y$) would be nearly the same. The excess of the former is due mainly to systematic inadequacies of the fit (see Appendix C.4).

The value 0.029 represents virtually a lower bound on the achievable 'mean square error' for this body of data. Despite its downward bias from the substantial number of 'zero counting rate' observations, it exceeds the 'Poisson' variance of 0.023 by about 25 percent. This excess is probably due to a combination of factors, including incomplete elimination of temperature and bias voltage instrumental effects, as discussed further below.

The 'improvement' of the MSD$(Y - y)$ over MSR *cannot* be taken to mean that some smooth "simple" adjustment of the model based on x,L coordinates might be found so as to yield similar improvement. Some of the bias apparently associated with x,L coordinates in different regions may be due to artifactual association with temporal, instrumental, or other small effects and such corrections could not be made overall in terms of a "simple" x,L dependence.

C.4 *Analysis of the Excess Variation*

A study of plots of cell MSD(Y) against each of y, x, and L indicates that large MSD values occur mainly in the $1.2 < L < 1.7$ region, at high average counting rates. This excess is due largely to

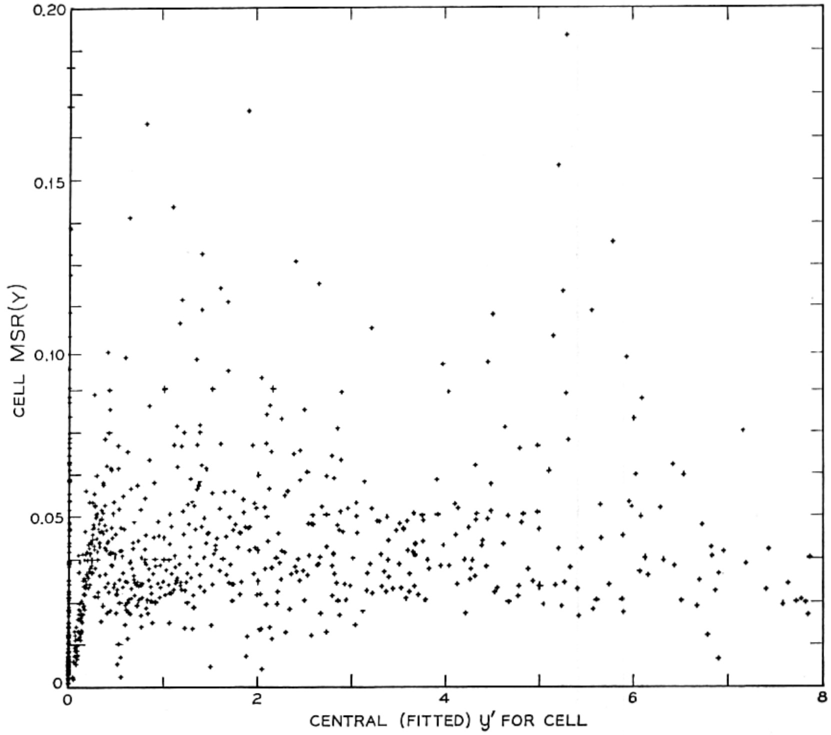

Fig. 59 — Cell MSR (Y) vs central value of y' for cell.

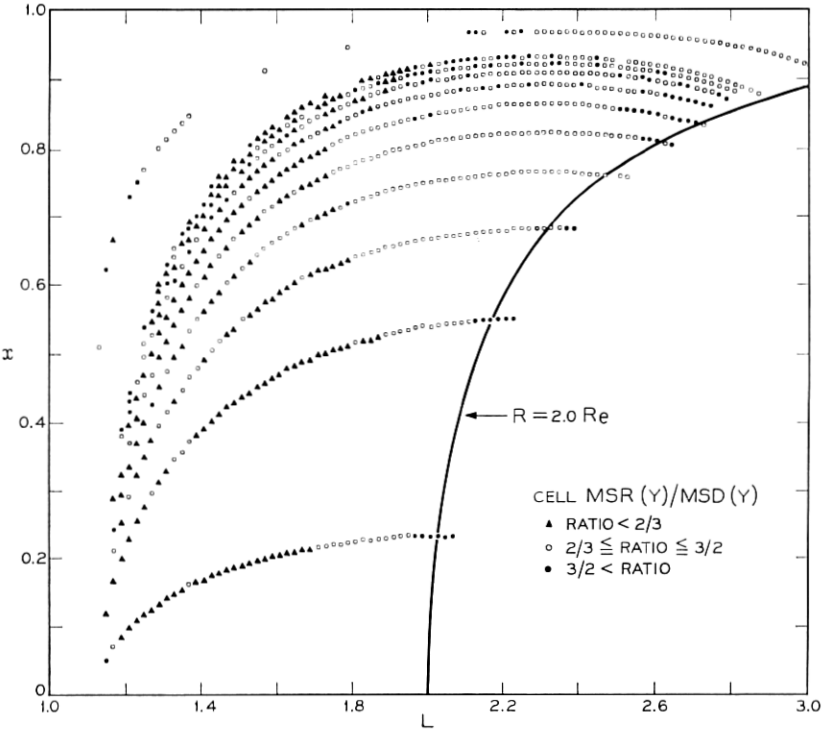

Fig. 60 — Positions of centers of regions in x, L space having certain ranges of cell MSR(Y)/MSD(Y). The ranges are indicated in the legend. (Plotted points are mid-points for the cells. Points appearing to the right of the boundary $R = 2.0\ R_e$ represent cells which have data only in one corner.)

the hybrid mode of x,L cell formation, in which the L-slices were equal length intervals, while within each L-slice, the x segments were chosen to have equal increments of y. Thus, at L values where y is large, the x,L cells will tend to have a larger y range.

The tendency of MSD to rise with cell average counting rate is not mirrored by cell MSR behaviour. As shown by Fig. 59, the level of MSR is not dependent on y except, as expected, for those cells where the counting rate is near zero. Roughly speaking, the average level of cell MSR for y values away from zero is about 0.04, in agreement with the probability plot estimate of Section 8.1. Of course, Fig. 59 shows both smaller ordinate values and less dependence on the abscissa values than the comparable plot of Fig. 57.

The relation of cell MSR to cell MSD is partially indicated in Fig.

60, showing positions in x,L space of various ranges of the value of the ratio MSR/MSD. One sees that MSR tends to exceed MSD along the "outside" of the data region. The excess along the $R = 2\ R_e$ boundary is due mainly to model bias or inadequacy. The excess at high L-high x is probably associated with temporal effects. The large ratios along the left edge of the data, which is the cutoff region, is likely a reflection of deficiency of the function. The excess of MSR over MSD is associated in the main with small y values.

Fig. 61 shows cell mean square deviations of residuals, MSD$(Y - y)$, plotted against y. This plot shows less scatter (most noticably for MSD$(Y - y) > 0.075$) than that of Fig. 59, and a lower average level of MSD$(Y - y)$ for $y > 0$, as expected. The high values of MSD$(Y - y)$ are not related to y as such but rather, as other plots show, with "extra fluctuations" in the $1.2 < L < 1.7$ region. This is probably associated with the coarse HTB data partition which does not com-

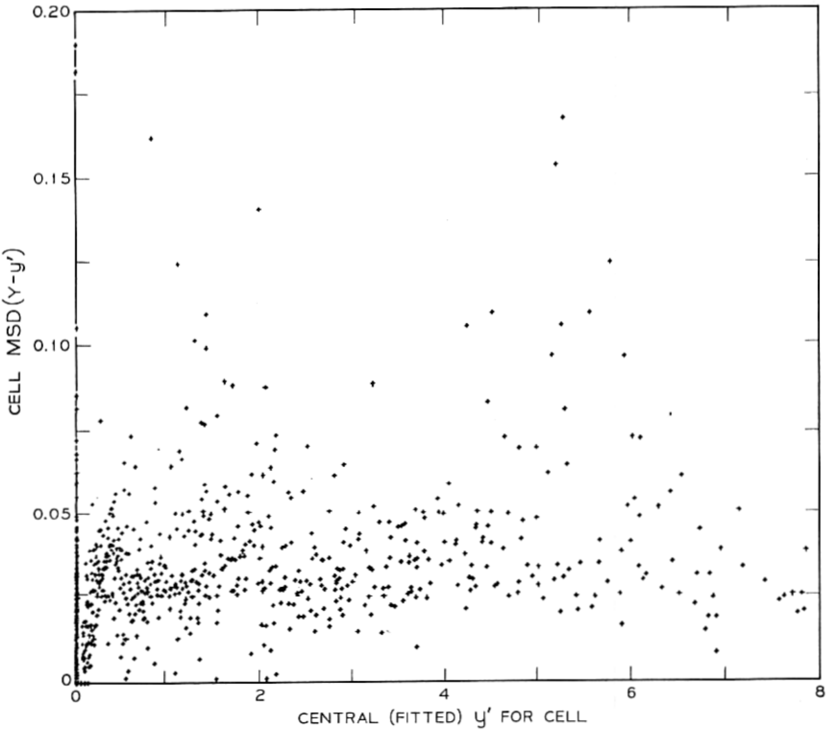

Fig. 61 — Cell MSD $(Y - y')$ vs central value of y' for cell.

pletely take care of the temperature and bias voltage instrumental effects.

REFERENCES

1. The *Telstar* Experiment, B.S.T.J., *42,* July, 1963, pp. 739–1940.
2. Brown, W. L., Buck, T. M., Medford, L. V., Thomas, E. W., Gummel, H. K., Miller, G. L., and Smits, F. M., The Spacecraft Radiation Experiments, B.S.T.J., *42,* July 1963, pp. 899–942.
3. Brown, W. L., Gabbe, J. D., and Rosenzweig, W., Results of the Telstar Radiation Experiments, B.S.T.J., *42,* July, 1963, pp. 1505–1560.
4. Brown, W. L. and Gabbe, J. D., The Electron Distribution in the Earth's Radiation Belts During July, 1962, as Measured by Telstar, J. Geophys. Res., *68,* 1963, pp. 607–618.
5. Gabbe, J. D. and Brown, W. L., Some Observations of the Distribution of Energetic Protons in the Earth's Radiation Belts between 1962 and 1964, *Radiation Trapped in the Earth's Magnetic Field,* B. M. McCormac, ed., D. Ridel Publishing Co., Dordrecht, Netherlands, 1966, pp. 165–184.
6. Chapman, S. and Bartels, J., *Geomagnetism,* Oxford University Press, London, 1940.
7. Buck, T. M., Wheatley, G. H., and Rodgers, J. W., Silicon *p-n* Junction Radiation Detectors for the Telstar Satellite, IEEE Trans. Nuc. Sci., *11,* 1964, pp. 294–301.
8. Courtney-Pratt, J. S., Hett, J. H., and McLaughlin, J. W., Optical Measurements on Telstar to Determine the Orientation of the Spin Axis, and the Spin Rate, J. Soc. Motion Pict. Telev. Eng., *72,* 1963, pp. 462–484.
9. McIlwain, C. E., Coordinates for Mapping the Distribution of Magnetically Trapped Particles, J. Geophys. Res., *66,* 1961, pp. 3681–3692.
10. Roberts, C. S., On the Relationship between the Unidirectional and Omnidirectional Flux of Trapped Particles on a Magnetic Line of Force, J. Geophys. Res., *70,* 1965, pp. 2517–2528.
11. Chamberlain, J. W., *Motion of Charged Particles in the Earth's Magnetic Field,* Gordon and Breach Publishing Co., New York, New York, 1964.
12. McIlwain, C. E., Program INVAR, private communication, 1962.
13. Jensen, D. C. and Cain, J. C., An Interim Geomagnetic Field (abstract), J. Geophys. Res., *67,* 1962, pp. 3568–3569.
14. Heiskanan, W. A., Geodetic Data, *American Institute of Physics Handbook,* D. E. Gray, ed., McGraw-Hill Book Company, New York, 1957.
15. *The American Ephemeris and Nautical Almanac* for the Year 1962 (and for the Year 1963), United States Government Printing Office, Washington, D. C., 1960 (and 1961).
16. Wilks, S. S., *Mathematical Statistics,* John Wiley, New York, 1962.
17. Wilk, M. B., and Gnanadesikan, R., Probability Plotting Methods for the Analysis of Data. Submitted to Biometrika, 1966.
18. McIlwain, C. E., The Radiation Belts, Natural and Artificial, Sci., *142,* 1963, pp. 355–361.
19. Valerio, J., Protons from 40–100 MeV Observed on Injun 3, J. Geophys. Res., *69,* 1964, pp. 4949–4958.
20. Fillius, R. W., Trapped Protons of the Inner Radiation Belt, J. Geophys. Res., *71,* 1966, pp. 97–123.
21. Gabbe, J. D., Michaels, A. S., and Wilk, M. B., unpublished work, 1967.
22. McIlwain, C. E., Long-Term Changes in the Distribution of the 40- to 110-MeV Trapped Protons, Trans., AGU, *46,* 1965 (abstract), p. 141.
23. Blanchard, R. C., and Hess, W. N., Solar Cycle Changes in Inner-Zone Protons, J. Geophys. Res., *69,* 1964, pp. 3927–3938.
24. Filz, R. C., The Low-Altitude Inner-Zone Trapped Proton Flux during 1965 Measured at 55 MeV, Trans., AGU, *47,* 1966 (abstract), p. 129.
25. McIlwain, C. E., Redistribution of Trapped Protons during a Magnetic Storm, Department of Physics, Univ. of Calif. at San Diego, April, 1964.

26. Pizzella, G., McIlwain, C. E., and Van Allen, J. A., Time Variation of Intensity of the Earth's Inner Radiation Zone, October, 1959, through December, 1960, J. Geophys. Res., *67,* 1962, pp. 1235–1253.
27. Cain, J. C., Daniels, W. E., Hendricks, S. J., and Jensen, D. C., An Evaluation of the Main Geomagnetic Field, 1940–1962, J. Geophys. Res., *70,* 1965, pp. 3647–3674.
28. Cain, J. C., private communication, September, 1965.
29. Vette, J. I., Models of the Trapped Radiation Environment, *Volume I: Inner Zone Protons and Electrons,* National Aeronautics and Space Administration, Washington, D. C., 1966 (NASA SP-3024).
30. McIlwain, C. E. and Pizzella, G., On the Energy Spectrum of Protons Trapped in the Earth's Inner Van Allen Zone, J. Geophys. Res., *68,* 1963, pp. 1811–1823.
31. Bostrom, C. O., Zmuda, A. J., and Pieper, G. F., Trapped Protons in the South Atlantic Magnetic Anomaly, July through December, 1961; (2) Comparisons with Nerv and Relay 1 and Discussion of the Energy Spectrum, J. Geophys. Res., *70,* 1965, pp. 2035–2043.
32. Imhof, W. L. and Smith, R. V., Proton Intensities and Energy Spectrums in the Inner Van Allen Belt, J. Geophys. Res., *69,* 1964, pp. 91–100.
33. McIlwain, C. E., Fillius, R. W., Valerio, J., and Dave, A., Relay 1 Trapped Radiation Measurements, Department of Physics, University of California at San Diego, March, 1964.
34. Fillius, R. W., and McIlwain, C. E., Anomalous Energy Spectrum of Protons in the Earth's Radiation Belt, Phys. Rev. Letters, *12,* 1964, pp. 609–612.
35. Freden, S. C., Blake, J. B., and Paulikas, G. A., Spatial Variation of the Inner Zone Trapped Proton Spectrum, J. Geophys. Res., *70,* 1965, pp. 3113–3116.
36. Knecht, D. J., The Energetic-Proton Spectrum at the Lower Edge of the Inner Belt, Trans., AGU, *47,* 1966, (abstract), p. 128.
37. Lenchek, A. M. and Singer, S. F., Geomagnetically Trapped Protons from Cosmic-Ray Albedo Neutrons, J. Geophys. Res., *67,* 1962, pp. 1263–1287.
38. Van Allen, J. A., The Geomagnetically Trapped Corpuscular Radiation, J. Geophys. Res., *64,* 1959, pp. 1683–1689.
39. Frank, L. A., Van Allen, J. A., Whelpley, W. A., and Craven, J. D., Absolute Intensities of Geomagnetically Trapped Particles with Explorer 14, J. Geophys. Res., *68,* 1963, pp. 1573–1579.
40. Roberts, C. S., Electron Loss from the Van Allen Zones due to Pitch Angle Scattering by Electromagnetic Disturbances, *Radiation Trapped in the Earth's Magnetic Field,* B. M. McCormac, ed., D. Ridel Publishing Co., Dordrecht, Netherlands, 1966, pp. 403–421.
41. Brown, W. L., Observations of Transient Behavior of Electrons in the Artificial Radiation Belts, *Radiation Trapped in the Earth's Magnetic Field,* B. M. McCormac, ed., D. Ridel Publishing Co., Dordrecht, Netherlands, 1966, pp. 610–633.
42. Bartlett, M. S., The Square Transformation in Analysis of Variance, J. Roy. Stat. Soc. Suppl. *3,* 1936, pp. 68–78.
43. Anscombe, F. J., The Transformation of Poisson, Binomial and Negative Binomial Data. Biometrika, *35,* 1948, pp. 246–254.
44. Huyett, Marilyn J. and Wilk, M. B., A General Fortran II Program for Nonlinear Least Squares Regression, unpublished manuscript, 1960.
45. Wilk, M. B., An Identity of Use in Nonlinear Least Squares (abstract), Ann. Math. Statist., *29,* 1958, p. 618.
46. Lundberg, J. L., Wilk, M. B., and Huyett, Miss M. J., Estimation of Diffusivities and Solubilities from Sorption Studies, J. Polymer Sci., *57,* 1962, pp. 275–299.
47. Lundberg, J. L., Wilk, M. B., and Huyett, Miss M. J., Sorption Studies using Automation and Computation. Ind. Eng. Chem. Fundamentals, *2,* 1963, pp. 37–43.
48. Wilk, M. B., Gauging the Magnitude of Correlation. Submitted to J. Amer. Stat. Assoc., 1966.